Charles University in Prague
Faculty of Mathematics and Physics

DOCTORAL THESIS

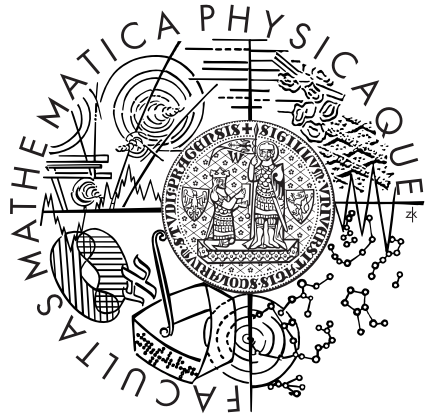

Kamil Olejník

Preparation and characterization of ferromagnetic GaMnAs epilayers

Institute of Physics ASCR, v. v. i.
Supervisor: RNDr. Josef Zemek, CSc.

Acknowledgements

This thesis was done in years 2004-2009 in the laboratory of molecular beam epitaxy of the Institute of Physics, ASCR where I participated on a work on preparation of ferromagnetic GaMnAs layers.

I would like to thank to my supervisor RNDr. Josef Zemek, CSc. for guidance during the work on this thesis and during my whole work in the Institute of Physics since 2000.

Then I want to thank to all my colleagues from the Department of spintronics and nanoelectronics, especially to Vít Novák and Miroslav Cukr from the laboratory of molecular beam epitaxy, and to all our collaborators. For a representative sample of those see Fig. 1.

Then I would like to thank to Miroslav Maryško for introducing me to the use of the SQUID magnetometer, to Petr Jiříček for technical support during the XPS measurements, and to Jiří Zyka and Pavel Zich for various technical help.

I would also like to thank to my fiancée Hanka for understanding and support.

To summarize I would like to express my thanks to all people who supported me during my doctoral studies and who I had opportunity to collaborate with, who allowed me to become involved in the exciting physical research.

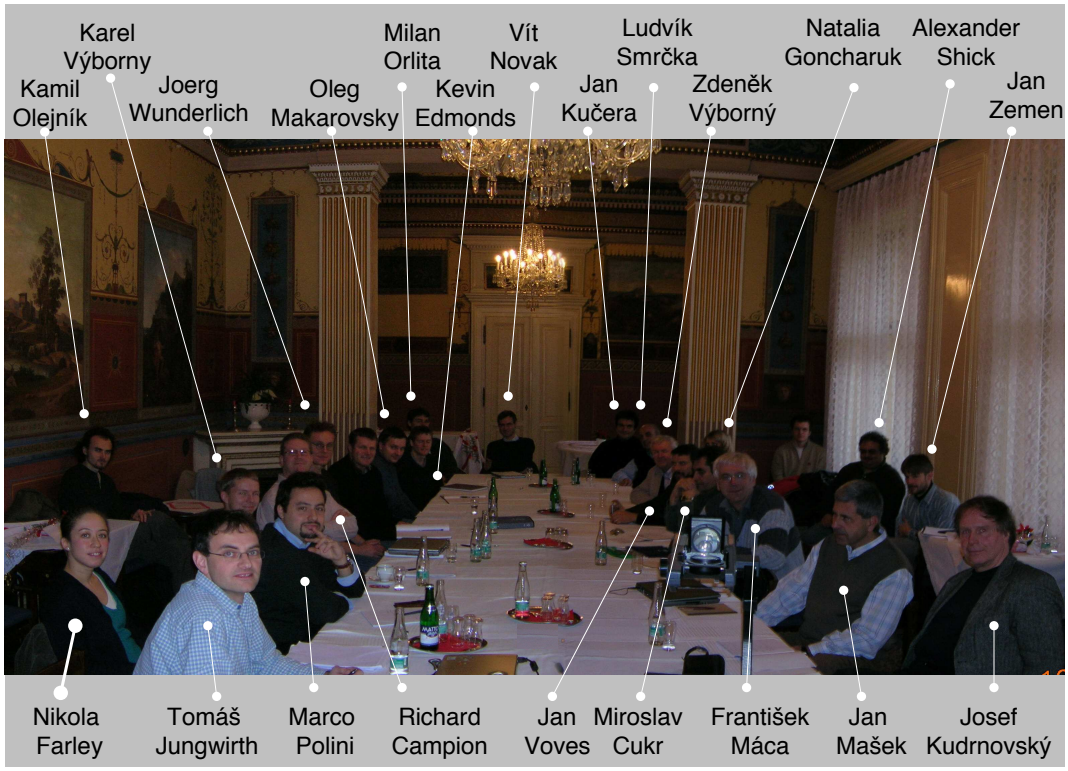

Figure 1: Lanna meeting, Prague, 2005.

Contents

Contents

Chapter 1

Introduction

GaMnAs belongs to a family of (III,Mn)V dilute magnetic semiconductors. These materials attracted a great deal of the scientific interest after the recent discovery of their relatively high Curie temperature [1]. The interest is stimulated by the possible applications of these materials in semiconductor spintronics.

The role of magnetic Mn atoms in the (III,Mn)V materials is two-fold: first, they introduce localized magnetic moments, second, when substituting group III element they acts as acceptors introducing free carriers, holes. The combination of localized magnetic moments of Mn atoms and high density of holes intercepting the ferromagnetic order between the localized moments results in strong carrier mediated ferromagnetism observed in this class of material. The robustness of the carrier mediated ferromagnetism is demonstrated in GaMnAs where Curie temperature as high as 150 K has been observed in material with Mn doping around 5% (of Ga sublattice), in contrast to ferromagnetism of MnAs metal where 100% Mn concentration results in Curie temperature of "only" 310 K.

Mn concentrations well above the equilibrium solubility limit are needed for the ferromagnetism in GaMnAs. The non-equilibrium low temperature molecular beam epitaxy growth is used to circumvent this problem. During the low temperature growth, however, large amount of defects is formed in GaMnAs material. The properties of the layers depend critically on the defects which are controlled by the growth conditions. This thesis focuses mainly on the experimental aspects of the preparation of GaMnAs layers and their basic characterization.

1.1 Structural properties of GaMnAs

Structural properties of GaMnAs are derived from the properties of the GaAs host semiconductor. GaMnAs epitaxial layers retain the zinc-blend structure of GaAs. Mn atoms are randomly distributed in the host matrix. At low concentrations the equilibrium Mn position is in the substitutional position at the Ga sub-lattice. In this position Mn acts as an acceptor. The GaAs structure is illustrated in Fig. 1.1.

At high Mn concentrations, compensating defects form in the p-type GaMnAs

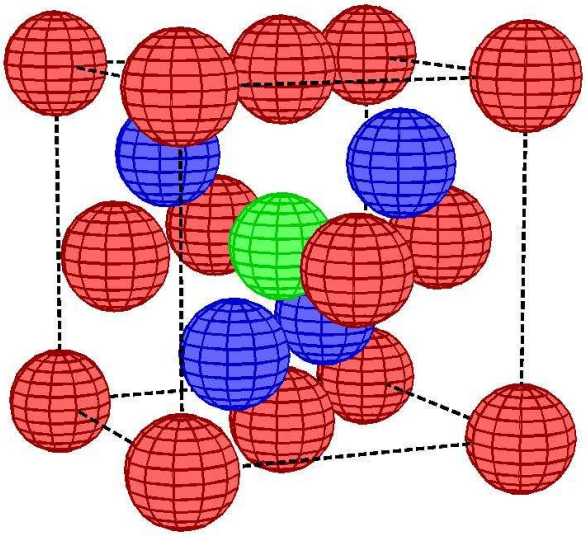

Figure 1.1: The crystal structure of GaMnAs. Red and blue spheres represent As and Ga atoms, respectively. The green sphere in the center represents a Mn atom in the tetrahedral interstitial position with four Ga nearest-neighbor atoms.

material [2]. This is result of the material tendency to self-compensation. The most common defects are Mn interstitials and As antisites, both of them being double donors.

The properties and the role of compensating defects were studied in detail in numerous works both theoretically and experimentally [2-10] . Experimentally the presence of Mn interstitial defects was evidenced by channeling Rutherford backscattering experiments [3].

Theoretically the onset of formation of compensating Mn interstitials was predicted to Mn concentration around 2% [4], which is in good agreement with experimental observations [5].

The role of Mn interstitials is very important. The formation of Mn interstitials limits the substitutional Mn concentration which is decisive for magnetic properties of GaMnAs. Moreover, the Mn interstitial atoms couple antiferromagnetically with neighboring substitutional Mn atoms thus further weakening the ferromagnetism of the material [6]. The role of the compensating defects will be discussed in detail in the following section in connection with the MBE growth of the GaMnAs layers and in connection with the low temperature annealing.

The lattice constant of GaMnAs layers is larger than the lattice constant of GaAs. As confirmed by x-ray diffraction experiments, fully strained (pseudomorphic) layers are prepared by low temperature MBE when GaMnAs layers are deposited on GaAs substrates [1, 7, 8].

x_{Mn} (%)	p (cm^{-3})	M (emu/cm^3)
0.001	2.21×10^{17}	0.00924
0.01	2.21×10^{18}	0.0924
0.1	2.21×10^{19}	0.924
1	2.21×10^{20}	9.24
5	1.1×10^{21}	46.2
10	2.21×10^{21}	92.4
100	2.21×10^{22}	924

Table 1.1: Table of calculated hole concentration p and magnetic moment density M of GaMnAs material with varying Mn doping x_{Mn} calculated assuming one hole and magnetic moment of $4.5\mu_B$ per Mn atom.

Theoretical calculations predict the lattice constant of $Ga_{1-x}Mn_xAs$ material to be only weakly sensitive to the substitutional Mn concentration x_s. On the other hand, it is predicted to be sensitive to the presence of Mn interstitials and As antisites. Ab-initio calculations predict the following dependence of the lattice constant [9]:

$$a(x_s, x_i, y) = a_0 + 0.002x_s + 0.105x_i + 0.069y \ (nm) \tag{1.1}$$

where $a_0 = 0.565361$ nm is the lattice constant of GaAs, x_s is the concentration of substitutional Mn atoms, x_i is the concentration of interstitial Mn atoms, and y is the concentration of As antisite defects.

The magnetic moment per Mn atom in GaMnAs is reported to be between 4 and 5 μ_B. The value depends on presence of Mn interstitials and on the hole density [10]. In this thesis, the value of $4.5\mu_B$ will be assumed for the sake of interpretation of experimental data. Tab. 1.1 lists the hole concentration and magnetic moment density calculated for various Mn concentrations assuming one hole per Mn atom and magnetic moment of $4.5\mu_B$ per Mn atom.

The ferromagnetic $Ga_{1-x}Mn_xAs$ material with Mn concentration above $\sim$1% is in the metastable phase above the equilibrium solubility of Mn which is $\sim 0.1\%$. In equilibrium, the excess Mn atoms form MnAs precipitates in GaAs. To circumvent this problem, the technique of low temperature MBE needs to be used for the preparation of GaMnAs material.

1.2 Preparation of GaMnAs

1.2.1 Low temperature epitaxial growth

Non-equilibrium low temperature MBE growth is used for the preparation of heavily Mn doped GaAs material. First attempts to introduce magnetism to III-V host by this technique date back to late 1980s, when the first report on the Mn incorporation to GaAs by the technique of low temperature MBE was published [8].

This pioneering work revealed the possibility to dilute over-equilibrium amount of Mn to the III-V host. Three growth regimes were recognized:

- At standard growth temperatures (∼550°C) Mn segregates to the surface.
- At lower growth temperatures (∼400°C) ferromagnetic MnAs inclusions form in the growing material.
- At very low growth temperatures (∼200°C) homogeneous (non-equilibrium) GaMnAs alloy is formed.

At that time, however, no ferromagnetism was observed in the (III,Mn)V alloy. The first successful preparation of the ferromagnetic (III,Mn)V material was reported in 1992 for InMnAs [11]. The first ferromagnetic GaMnAs was reported in 1996 [12].

By careful optimization of the growth parameters the Curie temperature of GaMnAs has been increased up to 110 K [13]. With the post-growth annealing (which is discussed in detail in the following section) the Curie temperature of high quality GaMnAs layers was increased well above 150 K [7, 14]. Currently the highest Curie temperature achieved in GaMnAs reaches 185 K [15, 16].

The main effect of the low growth temperature is the slowing down of the adatom lateral diffusion, thus inhibiting the Mn clustering and segregation from the growing GaMnAs alloy. The low growth temperature, however, in general induces formation of defects deteriorating the material properties.

Fig. 1.2 shows the growth diagram of GaMnAs reconstructed following [17, 7]. The 2D growth occurs only below the indicated roughening boundary. With increasing Mn doping the growth temperature needs to be lowered to avoid Mn segregation and accumulation on the surface which results in surface roughening. The roughening can be observed by Reflection High Energy Electron Diffraction (RHEED) and is deteriorating for the magnetic properties of the prepared material. The best magnetic properties are achieved on layers grown at temperature close to the roughening temperature. The exact knowledge of the roughening boundary is essential for successful growth of GaMnAs layers. Sec. 3.2 provides detailed description of construction of the growth diagram with extended Mn doping (up to 13%) and using reliable substrate temperature measurement by band gap thermometry.

Another important parameter during the low temperature MBE growth of GaMnAs is the As flux. The best properties of grown GaMnAs layers are achieved in near stoichiometry group V:III ratio [7]. It has been shown that the 2D-3D boundary can be substantially shifted when applying As overpressure [18].

Even under the non-equilibrium growth conditions, the semiconductor material tendency to self-compensation limits the substitutional Mn concentration, which is decisive for magnetic properties of GaMnAs layers [2, 19, 4]. Mn atoms in different crystallographic positions possess different energies depending on the hole concentration [2, 4]. In the case of low Mn doping the substitutional acceptor

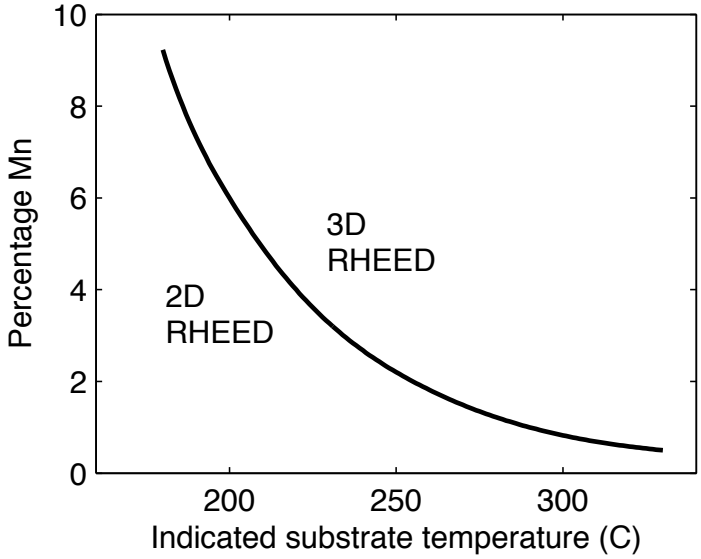

Figure 1.2: Transition from 2D to 3D growth mode as a function of growth temperature and Mn concentration.

position possess the lowest energy. With increasing doping the energy of substitutional Mn increases and the energy of compensating defects decreases. This results in increasing fraction of Mn incorporated into the interstitial positions. In simplified growth simulation the incorporation probabilities can be calculated as Boltzmann weighting factors reflecting the energy differences of Mn incorporated into different sites at given growth temperature [4]. This approach predicts onset of Mn interstitials at around 2% of the total Mn concentration and subsequent linear increase of their fraction. Though this approach completely neglects the kinetics of the growth process and the energies are calculated for bulk crystal, its predictions compare well with experimental observations [5].

The detailed description of the growth of GaMnAs layers requires the understanding of all involved surface processes (e.g. surface reconstructions, Mn segregation to the surface, surface diffusion of species during the growth, formation of precipitates with different phases, role of As overpressure). The incorporation pathway of Mn through Mn interstitial position was pointed out [2], however systematic theoretical description of the growth processes is still lacking.

It can be expected that the self-compensation tendency and the formation of defects resulting from the low growth temperature will at some point limit the effective Mn doping. Nevertheless, the question on the maximum value achievable by optimization of the low temperature MBE growth remains open, still motivating efforts to increase the Curie temperature of GaMnAs.

It is worth noting, that also an alternative route for preparation of (III,Mn)V with over-equilibrium Mn concentration by ion implantation has been developed.

With optimized post-implantation pulse-laser-melting and recrystallization procedure relatively high Curie temperatures has been achieved in GaMnAs (reaching 130 K [20, 21]). This procedures results in Mn incorporation into desired substitutional position thanks to short time scale of the recrystallization processes which inhibits Mn segregation from the alloy. Nevertheless, at present, the properties of the layers prepared by this technique do not reach the quality of the epitaxial GaMnAs layers. An important advantage of this technique is that materials with different semiconductor hosts can be relatively easily prepared (e.g. GaMnP [22]).

1.2.2 Annealing of GaMnAs layers

Low temperature annealing (at temperatures close to the growth temperatures $\sim$ 200°C) results in a substantial improvement of magnetic and transport properties of GaMnAs epitaxial layers [23, 24]. This effect is understood as a result of the out-diffusion of Mn interstitial defects towards the surface of GaMnAs layers. The high diffusivity of Mn interstitial atoms comes from relatively low barrier between adjacent interstitial sites [2, 24].

With increasing Mn content, both the growth and annealing temperature must be lowered to avoid the segregation of substitutional Mn from the GaMnAs alloy [15, 25, 26], which results in Mn clustering and formation of MnAs. Upon annealing at very high temperatures (500-600°C) MnAs clusters tend to grow and change phase to hexagonal NiAs-type [27].

Arsenic antisite defects are stable up to the temperature of about 450°C [28]. The role of As antisites during the low temperature annealing is believed to be negligible.

The Mn interstitial out-diffusion towards the surface during the annealing has been evidenced by various experiments [24, 29, 30]. It has been established that the Mn interstitial atoms need to be neutralized (e.g. by oxidation) on the surface of GaMnAs during the annealing. The influence of a controlled oxygen supply to the GaMnAs layer surface has been found [31]. Another approach to the Mn interstitial neutralization is based on the annealing under the As capping. In this case the Mn interstitials are neutralized by the reaction with arsenic resulting in the formation of a MnAs layer on the top of the GaMnAs layer [32].

It has been shown that the annealing is inefficient if the GaMnAs layer is covered by the GaAs capping layer [29]. The diffusion of Mn interstitials towards undoped GaAs (either to the substrate or capping layer) is not efficient. This is understood as a consequence of electrostatic interaction between positively charged mobile Mn interstitials (and holes) and negatively charged Mn substitutional atoms which are fixed in the GaMnAs layer.

To summarize, three aspects are essential for the effect of low temperature annealing:

- At annealing temperatures comparable to growth temperatures 150-250°C, only Mn interstitials are mobile, Mn substitutional atoms and As antisites

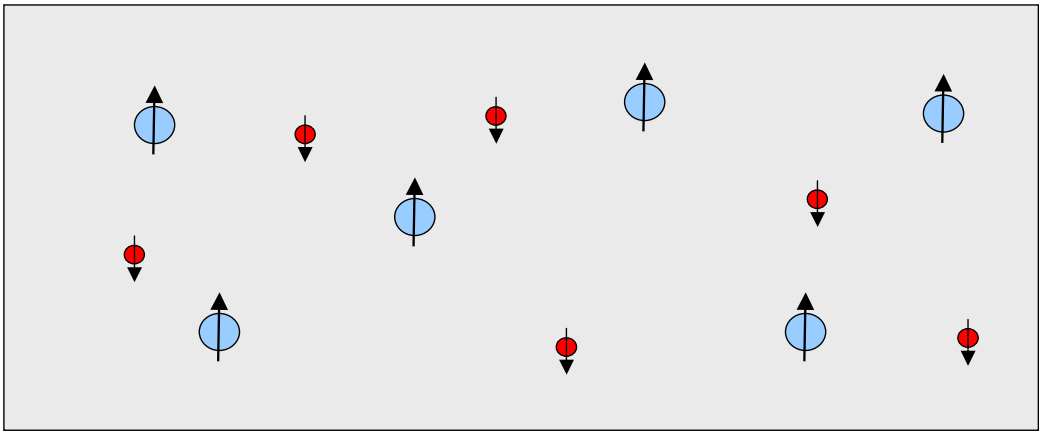

Figure 1.3: Illustration of carrier mediated ferromagnetic order in GaMnAs dilute magnetic semiconductor. Blue circles represent Mn atoms carrying magnetic moment, red circles represent itinerant holes anti-ferromagnetically coupled to the Mn ions and mediating their ferromagnetic order.

remain stable.

- Mn interstitials do not diffuse to substrate GaAs (or other undoped layers) due to the charging effects.
- Mn interstitials can leave the GaMnAs layer only if they are passivated on the surface (e.g. by oxidation).

In Chap. 6 we investigate the role of the surface oxide layer during annealing and the effect of its removal by etching on the efficiency of the annealing process.

1.3 Carrier mediated ferromagnetism

Long range Zener kinetic-exchange interaction is widely accepted as the dominant interaction determining the magnetic properties of Mn doped III-V semiconductors [33, 34]. This model captures the physics of interaction between localized moments of Mn atoms as being mediated by the semiconductor valence band holes (as illustrated in Fig. 1.3). The presence of magnetic ions results in the spin splitting of the semiconductor host bands, and hence in the spin polarization of free carriers which in turn stabilizes the magnetic order of the magnetic ions.

For the strength of carrier mediated ferromagnetism in Mn doped semiconductor, three properties are essential: Mn density, free carrier density, and strength of J_{pd} interaction between holes and d states of magnetic ions. Within mean field approximation the following expression for the Curie temperature T_c was derived

for the (III,Mn)V ferromagnets [33]:

$$k_B \cdot T_c = \frac{N_{Mn} S(S+1)}{3} J_{pd}^2 \chi_f \tag{1.2}$$

where N_{Mn} is the Mn density, S is the magnetic moment of magnetic ions, J_{pd} is the exchange interaction, χ_f is the spin susceptibility of itinerant holes, and k_B is the Boltzmann constant.

The mean field theory predicts that room temperature ferromagnetism could be achieved in GaMnAs with non-compensated substitutional Mn concentration around 10%. It is not clear at present, whether the preparation of GaMnAs with so high effective Mn concentration is technologically possible [5].

Other related materials are investigated in order to reach room temperature ferromagnetism in semiconductors [35]. Within the family of Mn doped III-V semiconductors the most promising material is the wide band gap GaN with very strong J_{pd} interaction. Its preparation is, however, very difficult and it is not clear at present whether high Curie temperatures reported in this material [36] should be attributed to the GaMnN alloy or to the presence of Mn rich precipitates.

Also promising are some special semiconductor heterostructures. In Mn δ doped AlGaAs/GaAs heterostructure the Curie temperature of 250 K was observed [37]. Recently, another route for realization of the room temperature ferromagnetism was reported [38]: the magnetic polarization of GaMnAs has been achieved by a magnetic proximity effect at a Fe/(Ga,Mn)As interface and has been evidenced at room temperature.

1.3.1 Magnetic anisotropy

The GaMnAs epitaxial layers exhibit a rich magnetic anisotropy. Theoretically this behavior is described on the basis of the anisotropy of energy of valence band electrons with respect to the magnetization direction. This is given by anisotropy of the valence band and strong anisotropic spin-orbital interaction [39, 40]. The anisotropic properties are modulated by magnetization density (which controls spin splitting of the valence band) and by hole concentration (which controls the occupation of the valence band). The temperature dependence of the anisotropy is governed by the temperature dependence of the magnetization [41].

Three main contributions to anisotropy are observed in GaMnAs epitaxial layers:

- Cubic anisotropy
- Uniaxial out-of-plane anisotropy
- Uniaxial in-plane anisotropy

The cubic magnetic anisotropy of GaMnAs is result of the cubic symmetry of the valence band of GaAs.

The out-of-plane anisotropy is understood as a consequence of strain/stress induced anisotropy of the valence band of GaMnAs layers grown on substrates with a slightly different lattice constant. Typically, GaMnAs is grown on the GaAs substrate which has a smaller lattice constant (the ratio $a_{GaMnAs}/a_{GaAs} = 1.001 - 1.005$ for Mn concentrations 1-10%). Mismatch of this size produces anisotropy in the valence band which is strong enough to overwhelm the cubic anisotropy and govern the easy axis to the plane or to the out-of-plane direction depending on the Mn doping and hole concentration.

The change of strain can be used for control of GaMnAs anisotropy. This was demonstrated on magnetic properties of GaMnAs layers grown on InGaAs substrate with larger lattice constant [42], and by experiments with piezo-electric stressors [43].

The third main magnetic anisotropy observed in GaMnAs layers is the in-plane uniaxial anisotropy, with its axis along in-plane diagonal direction [44]. The symmetry of zinc-blend structure does not allow the uniaxial in-plane anisotropy in bulk crystal. It has been shown theoretically that very small hypothetical shear strain could be used for simulation of the in-plane uniaxial anisotropy [34]. However, no experiment has evidenced such a shear strain in GaMnAs layers nor it is expected to be probable in epilayers grown on cubic substrates with cubic symmetry.

In principle the presence of uniaxiality in MBE grown GaMnAs is physically possible. During the epitaxial growth the symmetry between [110] and $[1\bar{1}0]$ direction is broken on the surface of the zinc-blend structure. The presence of surface reconstructions demonstrates this effect. It is known that the surface diffusivity of Ga is different in [110] and $[1\bar{1}0]$ directions [45]. So, it is probable that the distribution of distances between substitutional Mn atoms (and all defects) is different along [110] and $[1\bar{1}0]$ directions. However, so far no direct experimental evidence of such an ordering has been found. It is worth mentioning in this context, that the influence of MnAs precipitates on the anisotropic behavior has been observed [46].

The following expression is used for the description of the anisotropy energy using the lowest-order cubic and uniaxial terms [34]:

$$e_{ani}(\boldsymbol{n}) = K_c(n_x^2 n_y^2 + n_x^2 n_z^2 + n_y^2 n_z^2) + K_u^{out} n_z^2 + K_u \frac{(n_x + n_y)^2}{2}. \qquad (1.3)$$

where K_c is the cubic anisotropy constant, K_u^{out} is the out-of-plane anisotropy constant, K_u is the in-plane uniaxial anisotropy constant, and $\boldsymbol{n}$ is the unit vector of the magnetization direction ($\boldsymbol{n} = \boldsymbol{M}/|\boldsymbol{M}|$).

The out-of-plane uniaxial component results in energy maxima in the out-of-plane axis if K_{un}^{out} is positive, hence in the in-plane easy axis orientation. For standard layers grown on GaAs substrates the K_{un}^{out} is positive and large. Negative K_{un}^{out} occurs in the case of GaMnAs layers grown on substrates with larger lattice constant (e.g. InGaAs) or in the case of very low hole density [41].

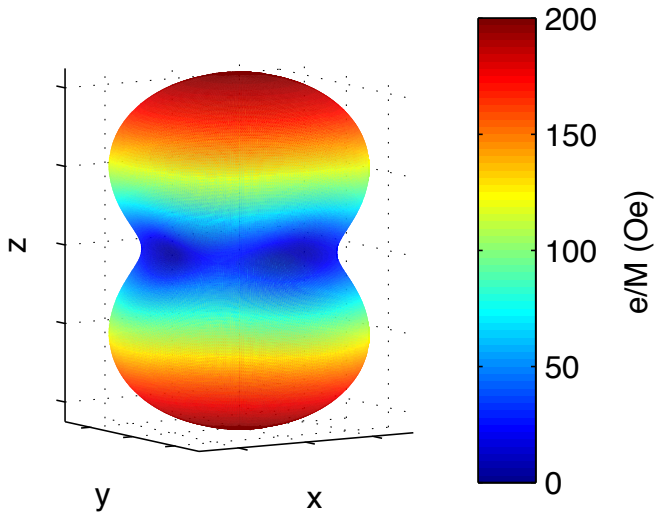

Figure 1.4: Example of the anisotropy energy functional calculated using Eq.1.3 with $K_c/M = 100\,\mathrm{Oe}$, $K_u^{out}/M = 200\,\mathrm{Oe}$, and $K_u = 0\,\mathrm{Oe}$.

An example of the anisotropy energy calculated with $K_c/M = 100\,\mathrm{Oe}$, $K_u^{out}/M = 200\,\mathrm{Oe}$, and $K_u = 0\,\mathrm{Oe}$ is shown in Fig. 1.4. The out-of-plane anisotropy dominates. The anisotropy energy minima (dark blue spots in the figure) in the xy-plane reflect the influence of the cubic component.

1.4 Magnetic semiconductors for spintronics

In spintronics, the spin degree of freedom of electrons is used in addition to their charge [47, 48, 49] . Today's spintronics is based on ferromagnetic metals and exploits the possibility to manipulate electrical transport properties of devices by magnetic means. The prototype example is the giant magnetoresistance device where the magnetization orientation of two ferromagnetic layers results in the low resistivity state in the parallel configuration and in the high resistivity state in the antiparallel configuration.

The essential property making the group of carrier mediated ferromagnetic semiconductors exceptional among other magnetic materials is that the magnetic properties are in a direct connection to the transport properties. This is a direct consequence of carrier mediated ferromagnetism, in which the spin polarization of charge carriers is not a side effect of ferromagnetic order, but it is an essential ingredient of it. Hence the ferromagnetic properties can be directly controlled by the electronic means (electric fields, gating, co-doping).

New spintronic phenomena based on ferromagnetic semiconductors have been

already demonstrated: control of magnetism by electrical gating of GaMnAs and InMnAs layers [50, 51, 52] and polarized light emission resulting from recombination of spin polarized carriers in the semiconductor material [53].

1.5 Aims and structure of this thesis

This thesis presents experimental study of preparation of GaMnAs epitaxial layers and their basic characterization. It pursues the following main aims:

- Optimization of the conditions of the epitaxial growth in order to achieve the best crystallographic, transport and magnetic properties of GaMnAs layers.
- Optimization and understanding of the post-growth annealing of the layers.
- Basic characterization of magnetic and electronic transport properties of the layers.

The structure of this thesis is as follows:

The first chapter provides an introduction to current state of understanding of GaMnAs preparation and its properties.

The second chapter surveys the used experimental methods. For the preparation of the layers we used the technique of low temperature Molecular Beam Epitaxy (MBE). The growth was monitored by the in-situ Reflection High Energy Electron Diffraction (RHEED). The method of band-gap thermometry was used for the sample temperature determination during the growth. For the characterization of the magnetic properties of the layers we used Superconducting Quantum Interference Device (SQUID) magnetometry. Finally, the technique of angular resolved X-ray Photoelectron Spectroscopy (XPS) is introduced, which we used for investigation of surface processes occurring during annealing of the GaMnAs layers.

Chapter 3 presents our experience concerning the growth of GaMnAs layers by the technique of low temperature Molecular Beam Epitaxy (MBE). The characterization of GaMnAs layers by RHEED is described and the role of the growth temperature and its monitoring by band-gap thermometry is studied. The chapter is concluded by the construction of the growth diagram which defines the optimal conditions for the growth of GaMnAs layers with a wide range of Mn doping.

Chapter 4 presents magnetic properties of the prepared layers. The Curie temperature trends are investigated on a series of samples with varying Mn doping grown in optimal conditions. The influence of the growth temperate on the magnetic properties is shown on a series of samples grown at different growth temperatures. In addition, the magnetic anisotropy of the layers is investigated in detail.

Chapter 5 presents electrical transport properties of the layers. The trends of conductivity are investigated and the temperature dependence of the resistivity of GaMnAs layers is studied.

Chapter 6 presents results concerning the low temperature annealing of GaMnAs layers. The role of the surface oxide during the annealing is studied. The processes which occur in the surface oxide during annealing are studied in detail by the technique of angular resolved x-ray photoemission spectroscopy (XPS).

The last chapter presents a summary of results and conclusions.

Chapter 2

Experimental methods

2.1 Molecular Beam Epitaxy

Molecular Beam Epitaxy (MBE) has developed from vacuum evaporation techniques in the late 1960s. It is used for growth of epitaxial layers of various materials. The technique is characterized by precise control of thickness and composition of the grown layers. The operation under ultrahigh vacuum conditions allows the preparation of very high purity materials.

Typical growth rates during MBE growth are 0.1-10 monolayers per second. At these growth rates the layer-by-layer growth can be achieved which is characterized by very smooth interfaces between layers of different composition and physical properties. This makes MBE a unique tool for the preparation of layered semiconductor heterostructures. MBE systems are nowadays designed and used not only for research purposes but also in the industry.

2.1.1 MBE chamber equipment

The schematic view of an MBE growth chamber is shown in Fig.2.1. It corresponds to Veeco Gen II MBE system used for all the growths presented in this thesis.

It is equipped with several effusion cells, shutters, rotatable sample holder, electron gun, screen for observation of RHEED patterns, vacuum gauge, band gap thermometer, vacuum pump, and cryo-panels.

The equipment of the MBE system can be divided into four groups according to its purpose: vacuum supporting equipment, sample manipulation, effusion cells and analytic tools.

To achieve ultra-high vacuum conditions (characterized by the pressure below 10^{-9} Torr) the MBE systems are equipped with sophisticated vacuum maintaining systems, consisting of a series of vacuum pumps, moreover cryo-panels cover a great part of the inner surface of the growth chamber, which act as pumps during the growth.

Once evaporated, the growth chamber is not exposed to the atmosphere to

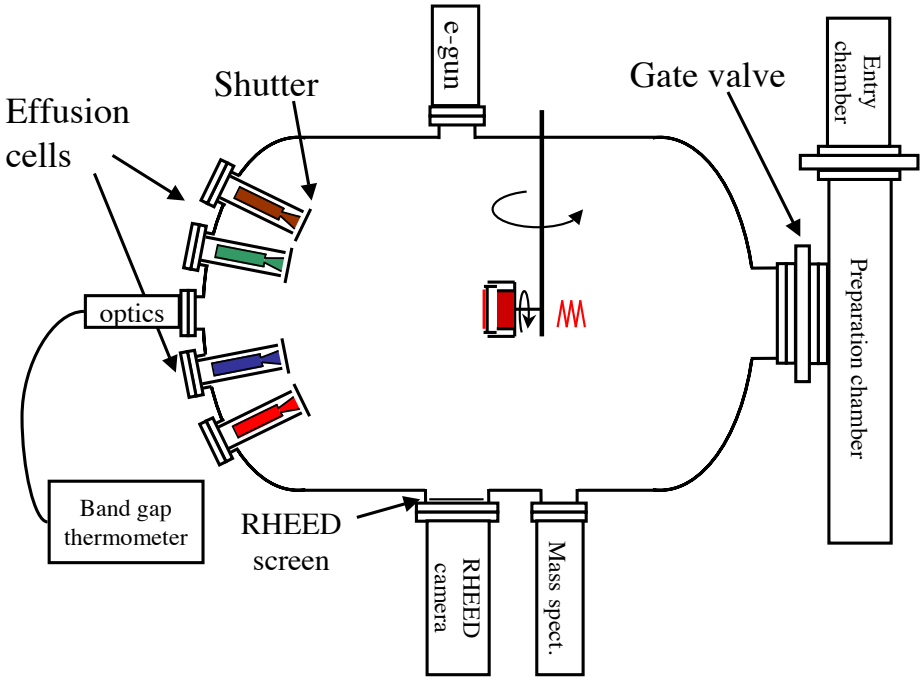

Figure 2.1: MBE chamber equipped with effusion cells, electron gun and fluorescent screen for RHEED, band gap thermometer, mass spectrometer, and rotatable sample manipulator.

prevent the contamination of materials in effusion cells and the inner environment in general.

When introducing new samples into the MBE system, they are first moved to the entry chamber. Here, samples are subjected to the first degassing procedure, then they are moved to the preparation chamber. In the preparation chamber, samples are degassed again and only then they are moved to the growth chamber. The degassing procedure is finished inside the growth chamber where the substrate is shortly heated above 600°C and the native oxide is desorbed from its surface. This last step is performed under As pressure to prevent As loose in the surface which would result in disruption of the monocrystallinity of the surface layers.

The in situ RHEED technique is widely used for the characterization of surfaces during MBE growth. For this purpose the growth chambers are equipped with an electron gun and with a fluorescent screen. The RHEED analysis is discussed in detail in Sec. 2.2.

2.1.2 Molecular beam fluxes

Effusion cells are used for the production of molecular beams, their fluxes are controlled by the temperature of the cells. In the ideal case of the Knudsen effusion, the molecular flux J impinging the sample surface is given by:

$$J = p(T) \cdot S \cdot G \tag{2.1}$$

where p is the vapor pressure of a particular material, S is the orifice area of the cell, and G is the factor taking into account geometry and distances inside the growth chamber. In practice however, the beam fluxes are modified by specific cell parameters such as the shape of the inner space or the amount of material left and periodic calibrations of fluxes are necessary.

The As cells are usually equipped with special valved-cracker cells. The valve of this cell is used for fast change of arsenic pressure. The temperature of the cracker part of the cell controls the fraction of arsenic dimers and tetramers.

Beam equivalent pressures (BEP) of molecular beams produced by effusion cells can be measured by the beam flux monitor (BFM). BFM is an ionization vacuum gauge which is positioned on the rear side the of the sample manipulator. BFM can be rotated to the growth position of the sample. In this position, it is used for the determination of the flux of the molecular beam. The change of the current in the vacuum gauge due to the cell opening and closing is proportional to the molecular beam flux. From the ratio of BEPs P_X/P_Y measured for two cells (with materials X and Y) the ratio of fluxes J_X/J_Y can be obtained using equation 2.2.

$$\frac{J_X}{J_Y} = \frac{P_X}{P_Y}\frac{\eta_X}{\eta_Y}\left(\frac{T_X M_Y}{T_Y M_X}\right)^{1/2} \tag{2.2}$$

where T_X and T_Y are the absolute temperatures of beam sources, and M_X and

M_Y are their molecular weights. The ionization efficiencies η are given by

$$\frac{\eta}{\eta_{N_2}} = \left[\frac{0.4Z}{14} + 0.6\right] \tag{2.3}$$

where Z is the atomic number of evaporated molecules (or atoms) and η_{N_2} is the ionization probability of a N_2 molecule.

BFM is a very useful, fast, and universal tool for the calibration of molecular fluxes of cells. Unfortunately, the vacuum gauge ionization is sensitive to the presence of different atomic species (either originating from rest atmosphere in the chamber or from the re-evaporation from the gage itself) which change the flux ionization probability, resulting in complex memory effects of BFM. To circumvent these problems we repeat the same routine during each calibration (with the same order of cells and the same exposition times). In this manner we obtain calibration which is reproducible though its absolute precision is not very high.

We use BFM to calibrate the ratio between Mn and Ga flux, i.e. for the determination of nominal Mn concentration. The error of the concentration determined in this way is approximately 10%.

For the absolute calibration of Ga and As_4 fluxes we use RHEED oscillations discussed in Sec. 2.2.

2.1.3 MBE Growth modes

The crystal growth mode depends on the bonding of adatoms to the substrate and to each other. Three main modes of crystal growth on surfaces can be distinguished [54]. If the bonding to the substrate is weak, Volmer-Weber mode occurs which is characterized by island formation. If the boding to substrate prevails, the Frank-van der Merwe mode of layer-by-layer growth takes place. Also an intermediate case can occur in which the whole surface is covered by adatoms and only then the island formation starts. The three growth modes are illustrated in Fig. 2.2.

2.1.4 GaAs surface reactions

The behavior of Ga and As atoms on the surface of GaAs is quite complex [55]. At temperatures above $\sim$330°C, the arsenic is desorbed from the GaAs surface forming the Ga terminated surface if the As over-pressure is not present. Further GaAs desorption is controlled by the Ga desorption rate, the dissociative evaporation of GaAs becomes measurable above 580°C [56].

For standard MBE growth of GaAs, the temperature region between 500°C and 600°C is typical. The GaAs surface is stable if kept under As overpressure and the growth rate is determined simply by the Ga flux.

The arsenic flux consists of arsenic tetramers and dimers (As_4 and As_2 molecules), their ratio is determined by the As source temperature. An additional heated zone (the cracker zone) of the As cell can be used for the control of ratio of As dimers and tetramers without the change of the bulk temperature of the cell.

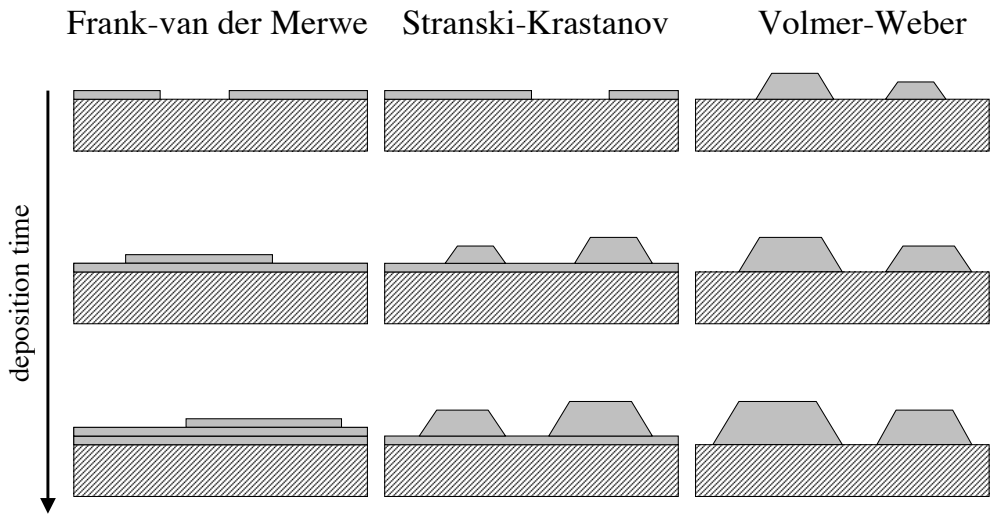

Figure 2.2: Schematic representation of Frank-van der Merwe, Stranski-Krastanov and Volmer-Weber crystal growth modes.

The sticking coefficient of As dimers varies between 0 and 1 depending on the presence of Ga on the crystal surface. If the GaAs surface is fully covered by Ga, the sticking coefficient of As dimers reaches unity - all the arsenic is chemisorbed to the surface.

In the case of the growth from the As tetramers the situation is more complex. Arsenic tetramers are in the first step physisorbed to the GaAs surface, where they migrate (with migration barrier of $\sim 0.25eV$). Then tetramers either re-evaporate (with activation energy 0.4eV) or they react with surface Ga. From each two molecules of As_4 four atoms are incorporated to the GaAs and four As atoms leave the surface in one As_4 molecule. Hence the sticking coefficient of As tetramers never exceeds 0.5 during growth of GaAs.

The role of Ga is rather simple in standard growth conditions. The Ga sticking coefficient is close to unity. If the As flux is sufficient, Ga incorporates to GaAs and determines the growth rate.

2.2 RHEED characterization

The method of Reflection High Energy Electron Diffraction (RHEED) is widely used for the in situ characterization of samples prepared by MBE. The glancing-incidence-angle geometry is compatible with crystal growth and at the same time it determines the high surface sensitivity of the method.

The RHEED pattern contains information on the surface reconstruction, sur-

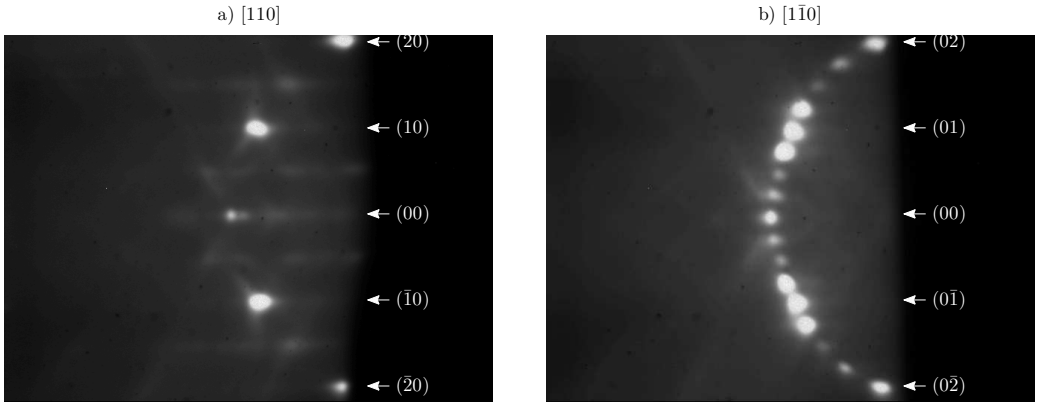

Figure 2.3: RHEED patterns acquired along a) [110] and b) [1$\bar{1}$0] directions on the GaAs surface. The sample was kept under As overpressure at the substrate temperature of 600°C. The patterns reveal a clear 2x4 reconstruction.

face roughness, lattice constant, and crystallinity of the surface layers of the growing material.

The typical energy of electrons in RHEED is 5-40 keV. The wave vector of the electrons is very large compared to the reciprocal lattice unit of GaAs (30-80x), therefore the diffraction pattern reflects almost planar cut through the reciprocal lattice.

The symmetry of diffraction pattern can be analyzed by kinematic theory. For the more detail analysis of intensities of the diffraction spots the use of advanced dynamical diffraction theory is necessary [57, 58].

In the case of very smooth surfaces and thanks to the glancing angle of incidence the penetration depth of reflected electrons reduces to several monolayers and the three-dimensional reciprocal lattice of bulk crystal transforms to the set of diffraction rods of the two-dimensional reciprocal lattice. The symmetry of the two-dimensional reciprocal lattice reflects the ordering of the surface. In the case of unreconstructed surface, the rods copy the symmetry of the crystal bulk. If the surface reconstructions occur additional fractional rods appear between main rods.

Fig. 2.3 shows a typical example of RHEED patterns acquired on GaAs (001) surface under arsenic overpressure with substrate temperature 600°C. The 2x4 reconstruction reflects in 1 additional spot between main diffractions in the [110] direction and in the presence of 3 additional spots in the [1$\bar{1}$0] direction. The circular set of diffraction spots observed in the [1$\bar{1}$0] direction nicely illustrates the cross-section of Ewald sphere with the set of diffraction rods. The corresponding Ewald construction is shown in the Fig. 2.4.

If the three dimensional structures are present on the surface standard three

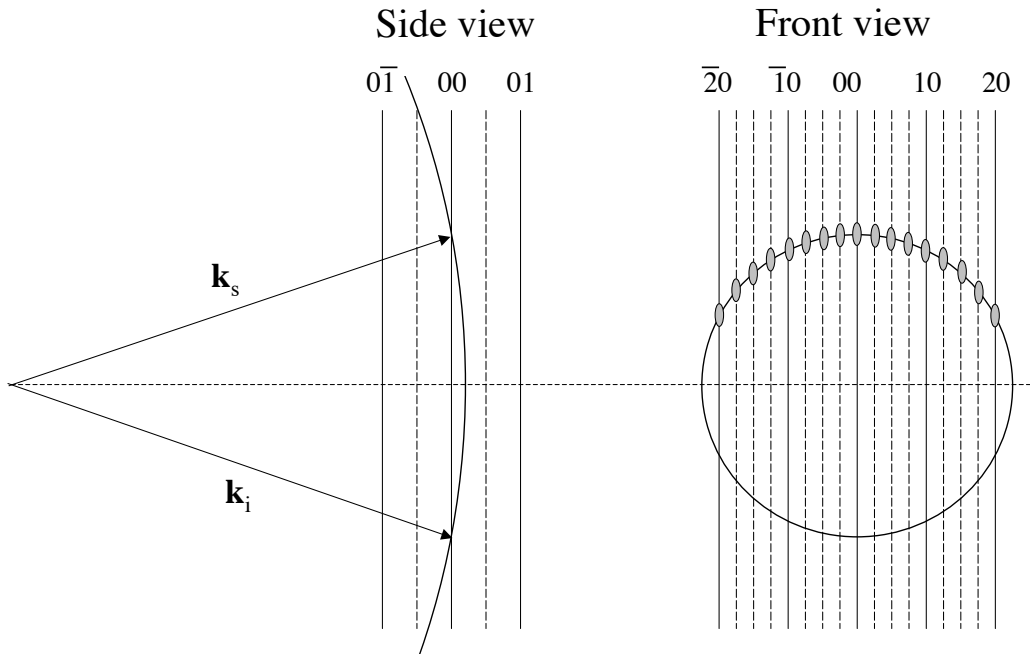

Figure 2.4: Ewald sphere cross-section with reciprocal lattice of GaAs (001) surface with 2x4 reconstruction. k_i indicates the wave vector of the incidence beam along $[1\bar{1}0]$ direction, k_s is the wave vector of specular beam. Full lines indicate the main diffraction rods, dashed lines indicate the fractional diffraction rods.

dimensional diffraction occurs.

Another feature of RHEED which is very important for MBE is the fact that the intensity of diffraction spots exhibit oscillatory behavior during layer-by-layer growth.

2.2.1 RHEED oscillations

The intensity of RHEED diffraction spots exhibit oscillatory behavior during the growth in the layer-by-layer mode. The period of one oscillation corresponds to the growth of one monolayer of material. The oscillations can be used for the calibration of the growth rate. We use the RHEED oscillations to calibrate the Ga flux during growth in standard growth conditions i.e. at high temperatures and with As overpressure. An example of the diffraction spot intensity oscillations measured during the growth of GaAs at growth temperature of 600° C is shown in Fig. 2.5a.

RHEED oscillations can be also used for the calibration of the As flux. As

mentioned above, under standard conditions the growth rate of GaAs is determined by the Ga flux while As flux is kept at a higher value. The excess As impinging the sample surface re-evaporates. In the case of Ga overpressure Ga remains on the surface and forms small droplets of pure Ga, the Ga stored in these droplets can be used for later growth of GaAs when As is available. This effect can be used for the calibration of As flux. A small amount of Ga is deposited on the surface with the As valve closed (approximately the amount needed for the growth of 5-10 monolayers of GaAs), the Ga cell is closed and then the As valve is opened. The growth of GaAs from the accumulated gallium and incoming arsenic starts. In this case, the growth rate is controlled by the arsenic and the frequency of RHEED oscillations is proportional to the As flux.

We calibrated the arsenic flux in this manner to obtain the near stoichiometric ratio between Ga (and Mn) and As which is needed for the low temperature growth of GaMnAs.

2.2.2 GaMnAs growth rate from RHEED oscillations

In principle the RHEED intensity oscillations can be also used for calibration of Mn flux from GaMnAs growth rate. Fig. 2.5b shows an example of RHEED growth oscillations recorded during the low temperature MBE growth. The first 60 s of the record shows growth of GaAs, at the growth time of 60 s the Mn cell was opened, and the growth of GaMnAs started.

The intensity oscillations shown in Fig. 2.5b weaken very quickly during the growth of GaMnAs. Fig. 2.5c shows the time dependence of the horizontal centroid position of the same peak. Oscillations of peak centroids are usually more pronounced during low temperature MBE growth of GaMnAs compared to the peak intensity oscillations.

It is worth mentioning, however, that the oscillation rate R observed during the growth of GaMnAs does not depend simply on the nominal Ga and Mn content. Assuming the most common defects (As antisites and Mn interstitials), one can come to the expression for R derived from the cation site counting:

$$R = R_{Ga} + R_{Mn}^{sub} + R_{As}^{anti} \tag{2.4}$$

where R_{Ga} is the incorporation rate of Ga, R_{Mn}^{sub} is the substitutional Mn incorporation rate, and R_{As}^{anti} is the antisite As incorporation rate. The Mn interstitials do not participate in the growth rate (their role is restricted to the lattice expansion in this context).

The RHEED oscillations can be observed only when the substrate rotation is not employed. In this case however, the geometrical setup of cells in the growth chamber results in a gradient of the fluxes across the sample which is approximately 5-10%. To circumvent this problem, sample rotation is routinely used during MBE growth.

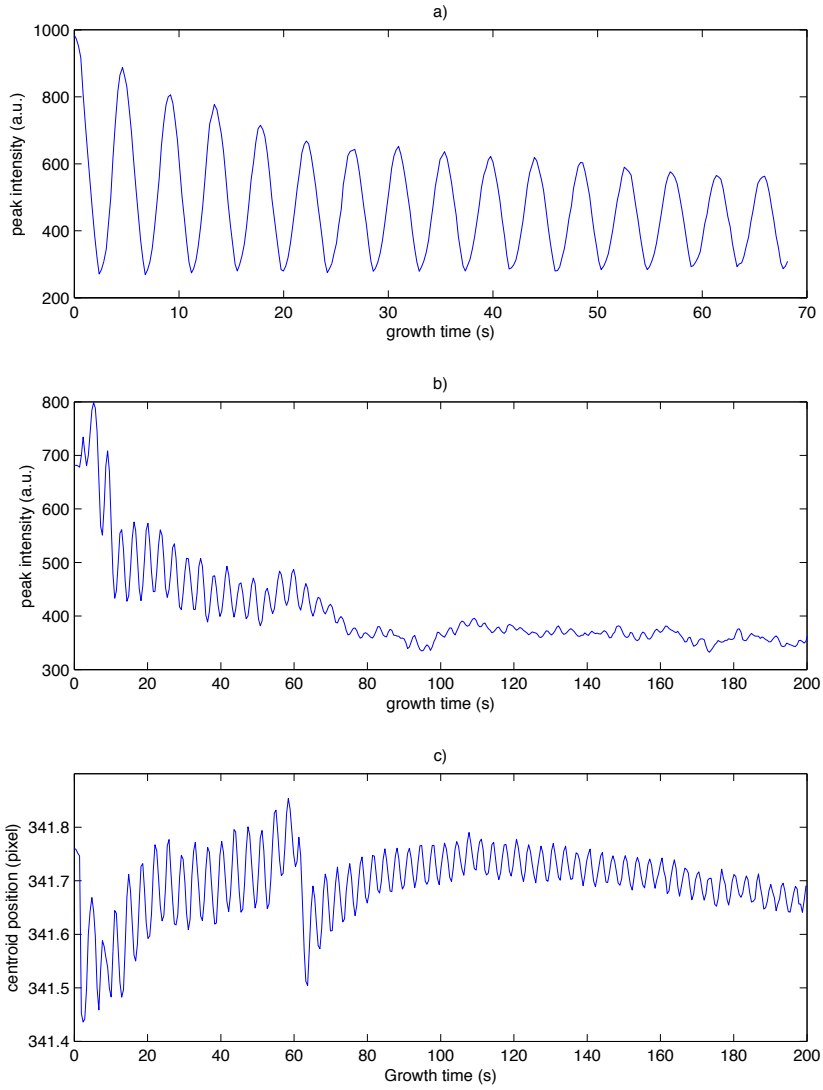

Figure 2.5: Examples of RHEED oscillations. a) oscillations of the peak intensity during the growth of GaAs at high temperature (substrate temperature $\sim 600°$C). b) intensity oscillations observed during low temperature growth, c) oscillations of the centroid position of the same peak. The low temperature growth consisted of a 60 s long growth of GaAs followed by the growth of GaMnAs.

2.3 Band gap thermometry

The temperature dependence of semiconductor band gap was recently utilized as a tool for the direct measurement of the semiconductor sample temperature during MBE [59]. This method provides reliable temperature values needed for the optimization MBE growth.

Fig. 2.6a shows the temperature dependence of the band gap of GaAs [60].

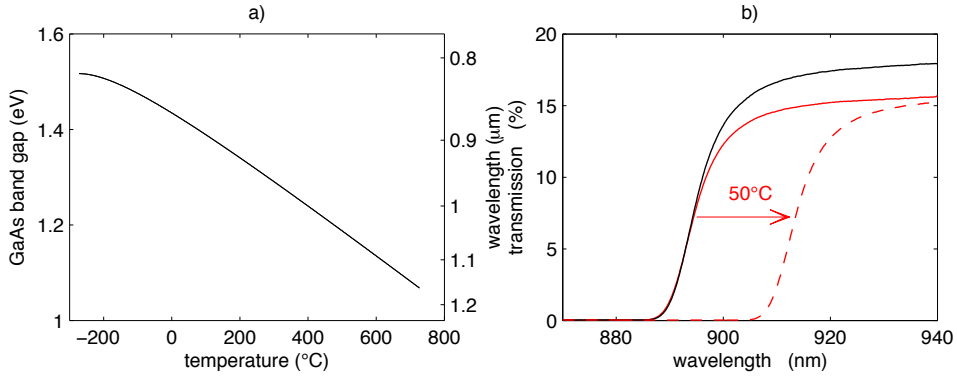

Figure 2.6: a) The temperature dependence of the GaAs gap. b) Examples of absorption edges measured at the room temperature on the GaAs substrate (black), and on the sample with the GaMnAs layer (red), the dashed line illustrates the shift of the edge corresponding to the temperature change of 50°C.

The absorption edge measured at the room temperature on the GaAs substrate and on the sample with the GaMnAs layer (thickness 150 nm, nominal Mn doping 7%) are shown in Fig. 2.6b. The dashed line shows the absorption edge of GaMnAs shifted by the difference corresponding to the temperature change of 50°C.

We can see that the absorption edge position is not sensitive to the presence of GaMnAs layer (of thickness typical for MBE grown layers) and that its position can be used for relatively precise temperature determination.

2.4 SQUID magnetometry

The typical magnetic moment of samples (of area of several mm^2 and thickness 10-100nm) is $\sim 1 \times 10^{-5}$ emu. For measurement of such a small magnetic moment the use of the Superconducting Quantum Interference Device (SQUID) magnetometry is necessary. We used commercial Quantum Design 5S magnetometer, equipped with cryostat which enables measurements between 2 and 300 K and with superconducting magnet with maximum field 5 T.

Fig. 2.7 shows a typical field dependence of magnetic moment of a sample with

a GaMnAs layer grown on GaAs substrate. The red points show the measured field dependence of magnetization, green points show the magnetization with subtracted diamagnetic contribution of the GaAs substrate (of thickness of 0.5 mm). The diamagnetic signal of the GaAs substrate is comparable with the ferromagnetic signal of the GaMnAs layer at field ∼0.25 T.

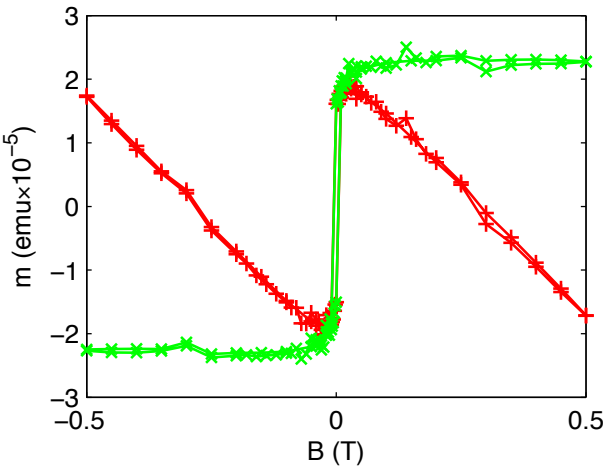

Figure 2.7: Field dependence of magnetization measured for a typical sample with a GaMnAs layer on the GaAs substrate. The red points show the raw data, the green points show the ferromagnetic component obtained by the subtraction of the diamagnetic component of the GaAs substrate.

2.5 Angular resolved XPS

X-ray Photoelectron Spectroscopy (XPS) is a surface sensitive analytical method used for investigation of material composition and electron structure. In XPS the sample is irradiated with monochromatic x-ray light, resulting in the emission of photoelectrons. The kinetic energy of photoelectrons E_k is in direct connection with the binding energy of electrons in the material E_b and follows:

$$E_k = h\nu - E_b - E_w \tag{2.5}$$

where E_w is the work function of the spectrometer and $h\nu$ is energy of x-ray photons.

From the binding energy and intensity of a photoelectron peaks, the elemental identity, chemical state, and quantity of elements can be determined.

XPS is surface sensitive method, this is due to the strong interaction of photoelectrons with matter. Within the inelastic scattering approximation the escape probability for an electron is proportional to $e^{-s/\lambda}$, where s is the length, which

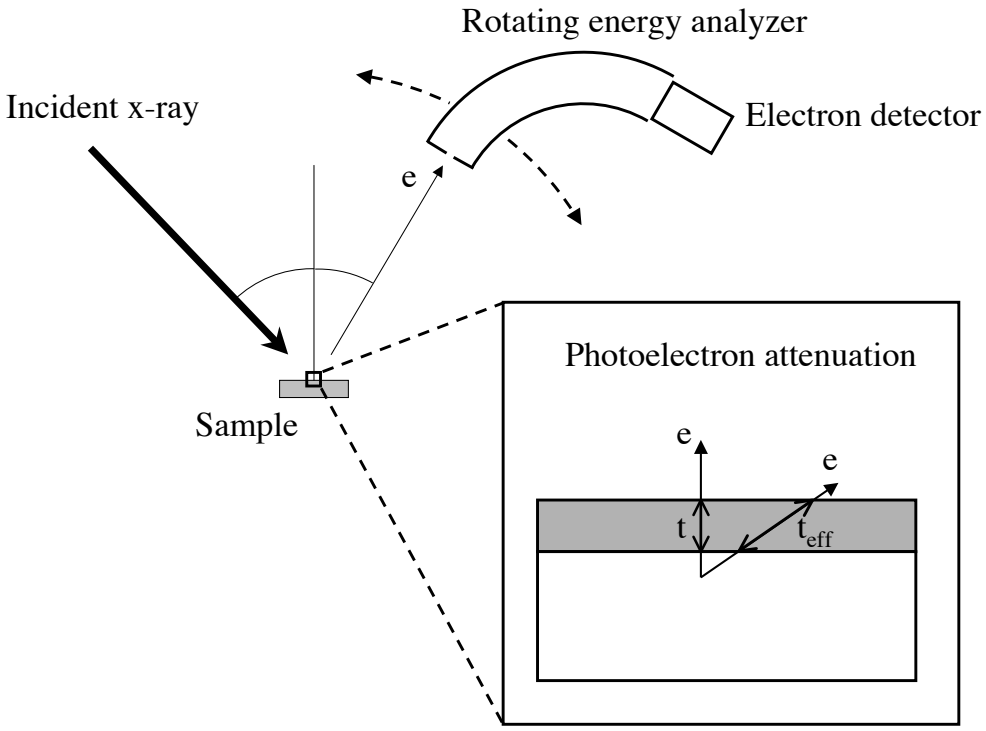

Figure 2.8: Geometry of the ARXPS experiment. Illustration of angular dependent attenuation of photoelectrons in layered structures.

electron travels through material before it reaches vacuum, and λ is the inelastic mean free path. Typical mean free paths of photoelectrons are in the range of several nanometers. The attenuation of photoelectrons defines the information depth.

The information depth can be modified by the emission angle. This can be used for investigation of depth profiles of elemental composition. A schematic view of the angular resolved XPS experimental geometry is shown in Fig. 2.8. The change of effective thickness of layer t_{eff} due to the change of the emission angle is illustrated. The exponential dependence of the escape probability gives rise to very strong angular dependent effects and large surface sensitivity of the method. The information depth can be modified by the emission angle. This can be used for investigation of depth profiles of elemental composition. A schematic view of the angular resolved XPS experimental geometry is shown in Fig. 2.8. The change of effective thickness of layer t_{eff} due to the change of the emission angle is illustrated. The exponential dependence of the escape probability gives rise to very strong angular dependent effects and large surface sensitivity of the method.

Chapter 3

MBE growth of GaMnAs

This chapter presents our results concerning the growth of GaMnAs layers.

Sec. 3.1 describes the dramatic increase of the substrate temperature during low temperature MBE growth of GaMnAs layers observed by band-gap thermometry and presents radiation heat transfer model which explains the observed temperature increase.

As discussed in Sec. 1.2.1, precise knowledge of the roughening boundary is essential for successful growth of GaMnAs. Section 3.2 describes the construction of the growth diagram of GaMnAs based on RHEED analysis of the growing material and reliable temperature measurement provided by the band gap thermometer.

3.1 Temperature increase during growth of GaMnAs

The possibility of the direct measurement of the temperature during the growth by the band gap spectrometry technique proved to be very useful in the case of the low temperature MBE growth of GaMnAs layers. In the low temperature growth regime temperature measurement by optical pyrometry is not possible. The only remaining standard tool for temperature determination is the thermocouple measurement. The thermocouple, however, is mounted on the sample manipulator and its thermal link to the sample is weak.

It turns out from the comparison of the band gap thermometer and the thermocouple measurements, that the thermocouple provides very unreliable temperature values. These values depend on the sample holder type and even on the sample holder surface state; we observed temperature changes due to a deposition of different materials on the sample holder having an influence on the substrate temperature during several following growths. Moreover, it turns out that the thermocouple temperature measurement completely fails to see the temperature increase observed by the band gap thermometry during the low temperature growth of heavily doped GaMnAs layers which is studied in this section.

The band gap thermometry reveals a surprising technological phenomenon occurring during low temperature MBE growth of GaMnAs layers: a dramatic in-

crease of sample temperature during the growth of GaMnAs layers on insulating GaAs substrates.

An example of the typical temperature evolution is shown in Fig. 3.1b. This temperature evolution was measured during 30 minute long growth of GaMnAs with nominal Mn concentration x=7%, which followed after 1 min long low temperature growth of GaAs. The sample was mounted in the free standing setup (see Fig. 3.2). The growth rate was approximately 5 nm / min. During the low temperature growth of the GaAs layer we observe a small increase of temperature caused by heat radiation coming from the open Ga cell (shown in detail in the inset). When the growth of GaMnAs starts, the steep increase of substrate temperature is observed which can not be attributed to the additional heat of the opened Mn cell (Mn cell temperature is around 800°C which is even smaller compared to the Ga cell temperature of 940°C, the cell dimensions are the same).

Only a small temperature increase is observed by the band gap thermometer during standard growth of GaAs at the temperature of 600°C. An example of the temperature evolution is shown in Fig. 3.1a. The temperature of the Ga cell was the same as in the case of low temperature growth. The temperature increase during the growth of GaAs can be simply attributed to the additional heat source of the open Ga cell. The oscillations of the temperature are caused by the substrate rotation and reflects the inhomogeneity of the substrate temperature.

In the case of the increase observed during the growth of GaAs, typically new temperature stabilizes after few minutes. On the contrary, in the case of the growth of GaMnAs layers the temperature is increasing on an order of magnitude longer time scale. At the end of the growth (when both Ga and Mn cells are closed again) the temperature decreases but it remains at a substantially higher value compared to its value before the start of the growth. These observation indicate that the heat transfer to the sample is substantially changed by the presence of the highly doped GaMnAs layer.

In Fig 3.3 the temperature evolutions measured during the growth of GaMnAs layers with varying Mn concentration are compared. The curves were shifted to equalize starting temperatures. We can see that the final value of the temperature increase is very similar for all the concentrations. For the lowest Mn doping the rate of the temperature increase is considerably slower, for higher Mn concentrations the rate is quite similar.

3.1.1 Radiation heat transfer model

To explain the temperature increase observed during the growth of GaMnAs layers let us consider the radiation heat transfer in the MBE chamber.

The MBE system contains numerous parts held at very different temperatures (varying from liquid nitrogen cooled cryo-panels at 77 K to the orifice of Ga cell at 940°C). In following considerations, we will use model containing just three parts: substrate heater, background, and hot orifices of the cells. These objects

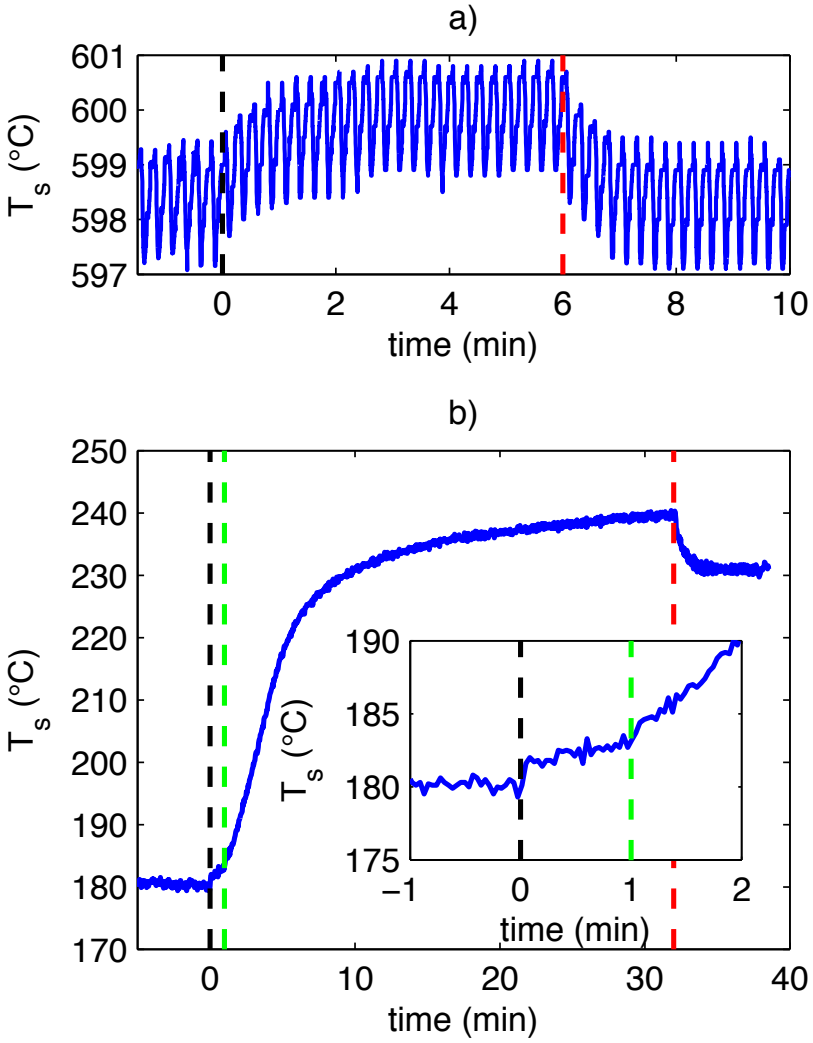

Figure 3.1: a) The temperature increase observed during the growth of GaAs at 600°C. b) The temperature increase observed during the low temperature MBE growth of a GaMnAs layer with nominal Mn concentration x=7%. Start of growth of GaAs (black vertical line), start of growth of GaMnAs (green line), end of growth (red line), inset in b) shows the detail of the temperature evolution during the first minutes of the low temperature growth.

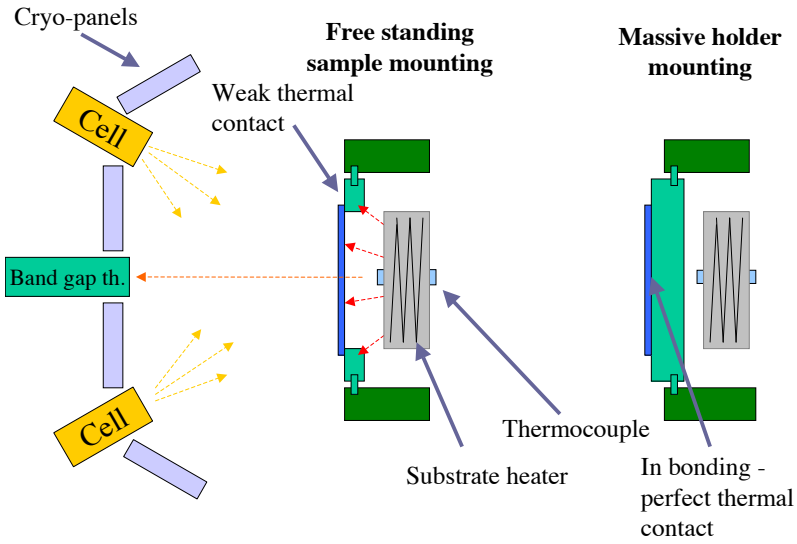

Figure 3.2: Illustration of radiation heat transfer inside the MBE chamber. Sketch of the free-standing sample mounting and sample mounting on the massive sample holder.

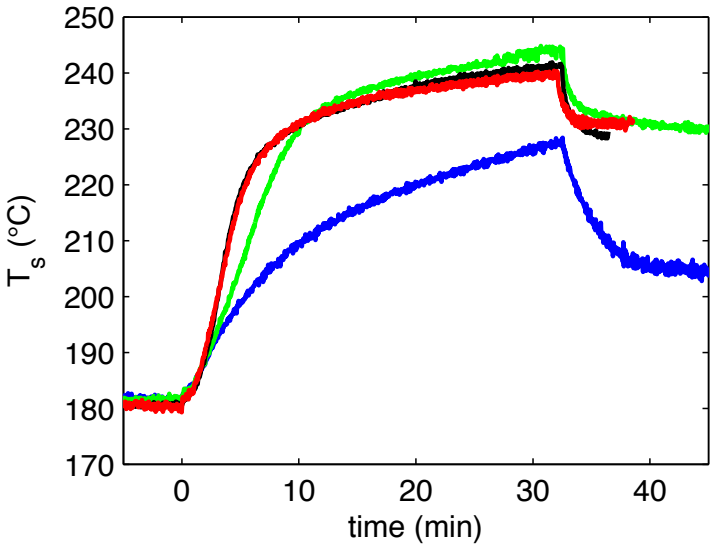

Figure 3.3: Sample temperature evolutions measured by band gap thermometry during growth of samples with various nominal Mn concentrations: 2% (blue), 3.5% (green), 5% (black), 7% (red).

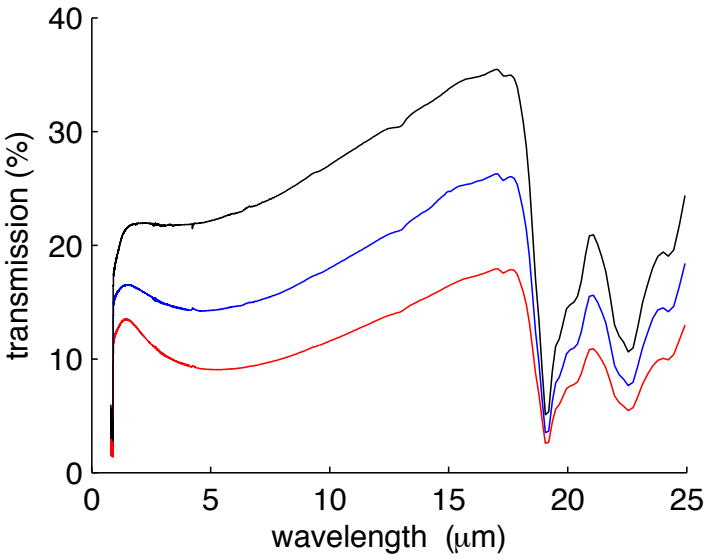

Figure 3.4: Infrared transmission of the GaAs substrate (black), and samples with GaMnAs layers with Mn concentration 7% of thickness 50nm (blue), and 150nm (red).

will be considered as black bodies. The heat propagation by conduction will be completely omitted.

Under these assumptions the net heat exchange of the sample Q_{net} can be expressed by the following equation:

$$Q_{net} = S \sum_i \int_0^\infty a_i [R(\lambda; T_i) - R(\lambda; T_s)] \alpha_s(\lambda) d\lambda \qquad (3.1)$$
$$i = h, b, c$$

where S is sample area, a is the solid angle of particular body, R is the spectral radiance, and α_s is the sample spectral absorptance. Indices h, b, and c denote heater, background, and cells, respectively. The radiation in the chamber is illustrated in Fig. 3.2.

As long as the sample spectral absorptance α_s is a constant over all wavelengths (sample is approximated as an ideal gray body), α_s can be taken out of the integral in Eq. 3.1 and no change of the equilibrium sample temperature due to the presence of the GaMnAs layer can be expected. It follows, that the spectral dependence of the absorptance need to be considered.

Fig. 3.4 shows the infrared transmission spectra of the GaAs substrate and samples with 7% GaMnAs of thickness 50 nm and 150 nm. We can see that the presence of the GaMnAs layer results in the change of transmission in broad energy region below the gap. The transmissivity of the GaAs substrate falls to zero

in the region of phonon absorption. The absorption on phonons starts on the double phonon absorption at $\lambda_{p2} = 17.5\mu$m and then varies with the wavelength as different combinations of acoustic and longitudinal optical phonons occur [61]. The start of the phonon absorption corresponds to the dip of transmissivity observed in Fig. 3.4 around 18μm.

Let us consider a simplified spectral absorptance α_s composed of two components: absorption on phonons (absorbing at all wavelengths above the first double phonon absorption) and free carrier absorption occurring in the growing GaMnAs layer (absorbing at all wavelengths). The absorptance α_s follows:

$$\alpha_s(\lambda) = \begin{cases} 1, & \lambda > \lambda_{p2} \quad \text{(phonon)} \\ \alpha_f = 1 - exp(-k_f d), & \lambda < \lambda_{p2} \quad \text{(free carrier)} \end{cases} \tag{3.2}$$

In this model the phonon absorption is equal to 1, the free carrier absorption is increasing with the increasing thickness of GaMnAs layer d, k_f is the absorption coefficient proportional to the density of free carriers.

The spectral radiance follows Planck's law:

$$R(\lambda, T) = \frac{2hc^2}{\lambda^5} \frac{1}{e^{\frac{hc}{\lambda k_B T}} - 1} \tag{3.3}$$

Spectral radiances of bodies held different temperatures are shown in Fig. 3.5. The red curve corresponds to the radiation coming from the cells (T_c=940°C) and the green curve shows the radiation coming from the substrate heater (T_h=330°C). The intensity of the cell radiation is scaled by a factor of 200, which reflects the ratio of the solid angle of the cells and the solid angle of the substrate heater.

If the absorption only occurs in the phonon region, a significant part of the radiation is not absorbed. With the additional absorption on free carriers the heat incoming to the sample is much larger. However, the sample heat emission also grows (its absorptance is equal to its emittance) so determination of the equilibrium temperature is not straightforward.

The heat power density radiated by a body P (per unit area and solid angle) at temperature T and with spectral absorptance α can be expressed as:

$$P(t) = \int_0^\infty R(\lambda; T)\alpha(\lambda)d\lambda \tag{3.4}$$

Figure 3.6 shows the power P radiated by bodies with different spectral absorptances $\alpha(\lambda)$, the dependences were normalized to the heat density radiated at the temperature of 330°C (the substrate heater temperature).

The red curve corresponds to the case of a black body ($d = \infty$ in Eq. 3.2), the green curve corresponds to the case of absorptance 0 below 17.5 μm and unity above (GaAs substrate with no GaMnAs, $d = 0$). The blue curve is an example of the dependence calculated for an intermediate case (d=50 nm).

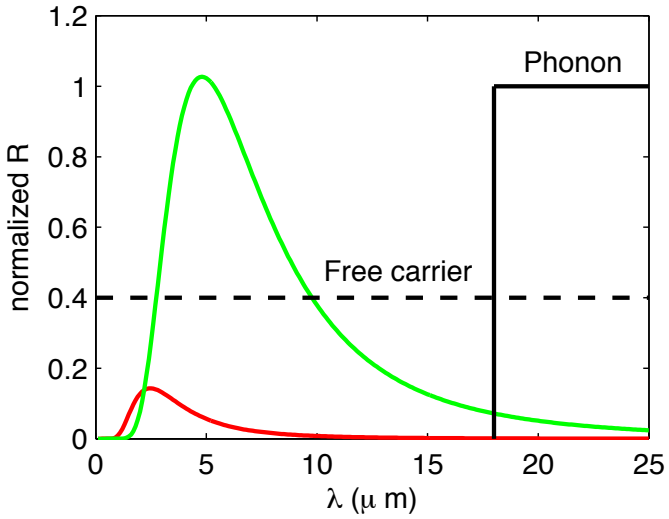

Figure 3.5: Spectral radiances of the heater (T_s=330°C, green curve) and cells (T_c=940°C, red curve, scaled by a factor of 200 reflecting the ratio of solid angle of the cells and the heater). Model regions of spectral absorptances due to the phonon and free carrier absorption.

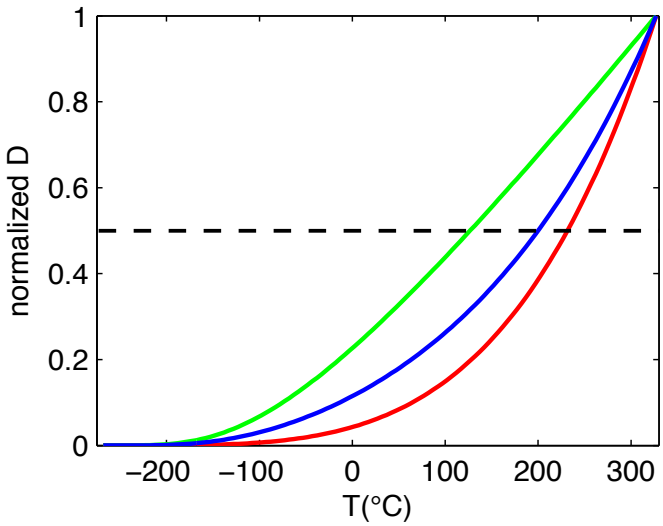

Figure 3.6: Heat power density radiated by samples with different spectral absorptances, normalized to the heater temperature of 330°C. Green curve: only phonon absorption ($t = 0$ in Eq. 3.2), blue curve: some free carrier absorption ($t = 50\,nm$) , red curve: full free carrier absorption, ideal black body ($t = \infty$).

Let us for a moment omit the radiation of cells and background. In this situation, one side of the sample sees the heater at temperature 330°C and no radiation is coming to the other side of the sample (zero temperature background). In equilibrium ($Q_{net} = 0$) eq. 3.1 reduces to the following form:

$$0 = \int_0^\infty [0.5 \cdot R(\lambda; T_h) - R(\lambda; T_s)]\alpha_s(\lambda)d\lambda \tag{3.5}$$

The heat emitted by the sample equals to the heat coming from the substrate heater. The sample has two sides so its heat radiation power needs to be exactly one half of the radiation power of the heater.

The dependences plotted in Fig. 3.6 can be used for graphical solution of the simplified equilibrium equation. The horizontal line in Fig. 3.6 crosses the dependences at the equilibrium temperature of the sample with particular spectral absorptance (and heater at 330°C). This analysis shows that the equilibrium temperature can change by 100°C when we take into account the change of the spectral absorptance.

Coming back to the original model, numerically one can evaluate the equilibrium temperature using Eq. 3.1 and Eq. 3.2 for a particular GaMnAs layer thickness, Mn concentration can be taken into account through the absorption coefficient k_f. Example simulations are shown in Fig. 3.7. The full lines show the dynamical evolution of substrate temperature T_s evaluated with the heat exchange equation in following form:

$$C\frac{dT}{dt} = Q_{net} = \int_0^\infty [a_h R(\lambda; T_h) + a_c R(\lambda; T_c) + a_b R(\lambda; T_b) - R(\lambda; T_s)]\alpha_s(\lambda)d\lambda, \tag{3.6}$$

where C is the heat capacity per unit area of sample. The following parameters were used in the simulations: T_c=940°C, T_b=20°C, T_h=320°C, $a_h = a_c + a_b$, $a_c = a_b/200$, C =907 Jm^{-2} (considering substrate thickness 0.5 mm and specific heat of GaAs at 200°following [60]). The absorption coefficient was estimated from transmission measurements of the sample with 150 nm thick GaMnAs layer and Mn doping 7% (Fig. 3.4), its transmission is approximately 50% of the substrate in the region between gap and phonon absorption, yielding $k_f \sim 4.5 \times 10^{-3}\,\mathrm{nm}^{-1}$. For low doped sample (with x=2%) we used k_f by factor 7/2 smaller reflecting the ratio of the doping. The growth rate was $\sim$0.27MLs^{-1} ($\sim$0.76Ås^{-1}).

The above approximation simplifies the phonon absorption, neglects the λ dependence of the free carrier absorption, reflectivity is not taken into account, and heat transfer by conduction is completely omitted. Nevertheless, the model explains the origin of the observed large increase of the sample temperature.

The change of sample spectral absorptance, which is caused by the presence of the heavily doped GaMnAs layer, results in the change of the equilibrium temperature of the sample during the growth of GaMnAs layers. This mechanism is unique to the growth of heavily doped (conductive) layers on insulating semiconductor substrates with limited spectral absorption. We published the study of the substrate temperature increase in [62].

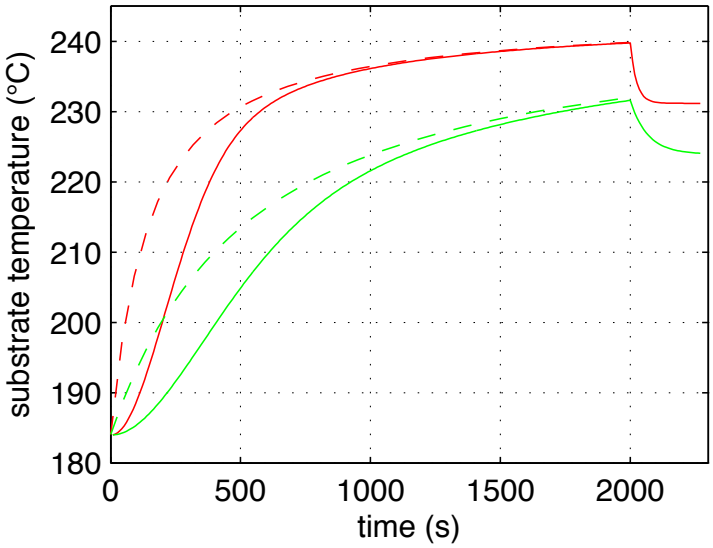

Figure 3.7: Simulated temperature evolutions of the substrate temperature during the growth of GaMnAs layers. The red curve shows the evolution calculated for high Mn doping (x ∼7%), the green curve corresponds to low Mn doping (x ∼2%). Dashed lines show the equilibrium solutions, full lines show the dynamical temperature evolutions.

3.1.2 Control of temperature increase

There are several possible ways to reduce the temperature increase during the growth of GaMnAs layers.

It is possible to reduce the temperature increase by the regulation of heater power. Unfortunately the heat capacity of the heater is large, so the regulation fails to compensate the fast change of the substrate temperature at the beginning of the GaMnAs growth.

Another possibility is to use the massive sample holder setup. In this case the temperature change reduces to the change induced by the additional radiation of open cells.

The next possibility is to pre-grow a thick layer of GaMnAs (with a temperature gradient) and bury it below a buffer layer of GaAs. Then, when the second layer of GaMnAs is grown on the same sample, only the increase due to the cell radiation occurs.

The band-gap temperatures recorded during growths of GaMnAs layers with a standard free standing sample mounting, massive sample holder mounting and pre-grown GaMnAs layer are shown in Fig. 3.8. The large temperature increase can be reduced to 20°C by the use of the massive sample holder or the pre-grown layer.

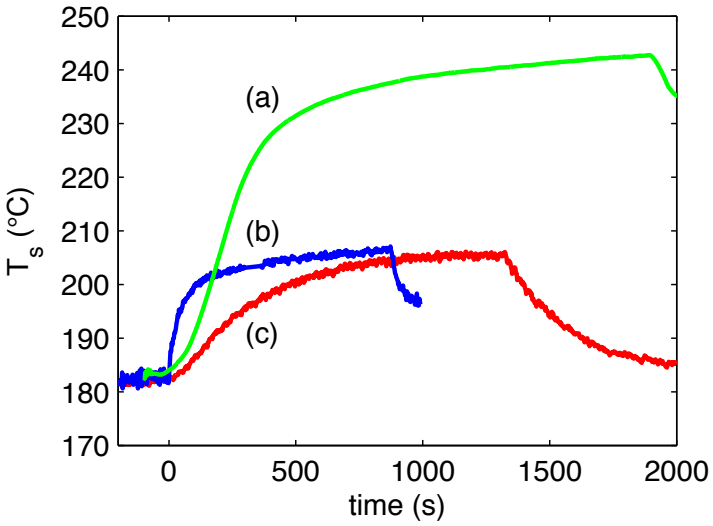

Figure 3.8: Comparison of temperature evolutions during the growth of GaMnAs layers in three setups: a) sample mounted in the free standing setup, b) sample mounted on the massive sample holder, c) sample with the pre-grown GaMnAs layer in the free standing setup.

To reduce further the temperature increase a change of standard MBE setup is necessary. With the use of two Ga cells the temperature change can be reduced down to several °C [15]. In this setup one of the Ga cells is used as the thermal equivalent of the Mn cell. The temperature is stabilized during low temperature growth of GaAs with both Ga cells opened, then one of them is closed and the Mn cell is opened. In this case the heat balance is not changed at the beginning of the GaMnAs growth.

3.2 Construction of growth diagram

3.2.1 RHEED patterns of GaMnAs

As discussed in Sec. 1.2.1 it is essential to maintain 2D growth conditions for the growth of GaMnAs layers. The homogeneous non-equilibrium solution of Mn to GaAs occurs only in this 2D layer-by-layer growth regime. As discussed in Sec. 2.2 the dimensionality of the surface can be determined from RHEED patterns of the grown layers. 2D surfaces are characterized by streaky patterns, usually accompanied with fractional diffractions reflecting surface reconstructions. 3D surfaces reveal spotty patterns with symmetry of the reciprocal lattice of the crystal bulk.

In Fig. 3.9 the RHEED patterns acquired after the growth of three GaMnAs samples are shown. Patterns a) and b) were acquired along [110] and [1$\bar{1}$0]

directions on a perfectly 2D surface of GaMnAs layer. Figures reveal the 1x2 reconstruction typical for GaMnAs layers.

The patterns c) and d) reveal a partially roughened surface of GaMnAs. The 2D-3D transition is not instantaneous, both streaks and spots are usually observed together on RHEED patterns during the roughening process. Typically this process lasts ~ 2 minutes which corresponds to the growth of ~ 30 monolayers of GaMnAs.

The patterns e) and f) were measured on a sample with a surface which has roughened during the growth. The spotty pattern reveals presence of islands on the surface. Nevertheless, the material is still almost a perfect single-crystal. The polycrystalline layer at the surface would be characterized by circular features in the RHEED pattern. The symmetry of the patterns reflects symmetry of the bulk zinc-blend structure (shown in Fig. 3.11a).

3.2.2 Phase-locked RHEED pattern acquisition

To produce homogeneous GaMnAs layers, the rotation of the substrate during the growth is necessary. The static RHEED images can not be acquired during the growth in this case. To monitor the surface during the growth with substrate rotation we developed a phase locked acquisition technique. The exposure time of the RHEED camera is set exactly to the time of one rotation of the sample (5 seconds in our case). Each acquired image is then an integral diffraction pattern showing superposition of all diffraction spots occurring during the sample rotation. Although some information is lost, these integral patterns clearly reveal the 2D or 3D nature of the surface.

Selected images acquired during the growth of GaMnAs layer with nominal Mn concentration of 6.5% are shown in Fig. 3.10. The change of the character of images indicates roughening of the surface during the growth.

Fig. 3.12 shows the differential image obtained by subtraction of two integral images. First image was acquired just before the roughening started and the second image was acquired 2 minutes later when the 3D features were already clearly seen. Red color indicates the increase of the intensity - developing 3D features, blue color indicates the decrease of the intensity - vanishing 2D features.

The symmetry of the 3D features is given by combination of diffractions in the diagonal directions and main directions. Fig. 3.11 shows cross-section of zinc-blend reciprocal lattice with (110) and (010) planes. By combining both contributions (shown in Fig. 3.11c) we obtain the symmetry of the experimentally observed 3D integral pattern.

3.2.3 Determination of roughening temperature

We used a combination of the phase-locked RHEED acquisition technique and band gap thermometry to analyze the 2D / 3D growth transition during the growth of

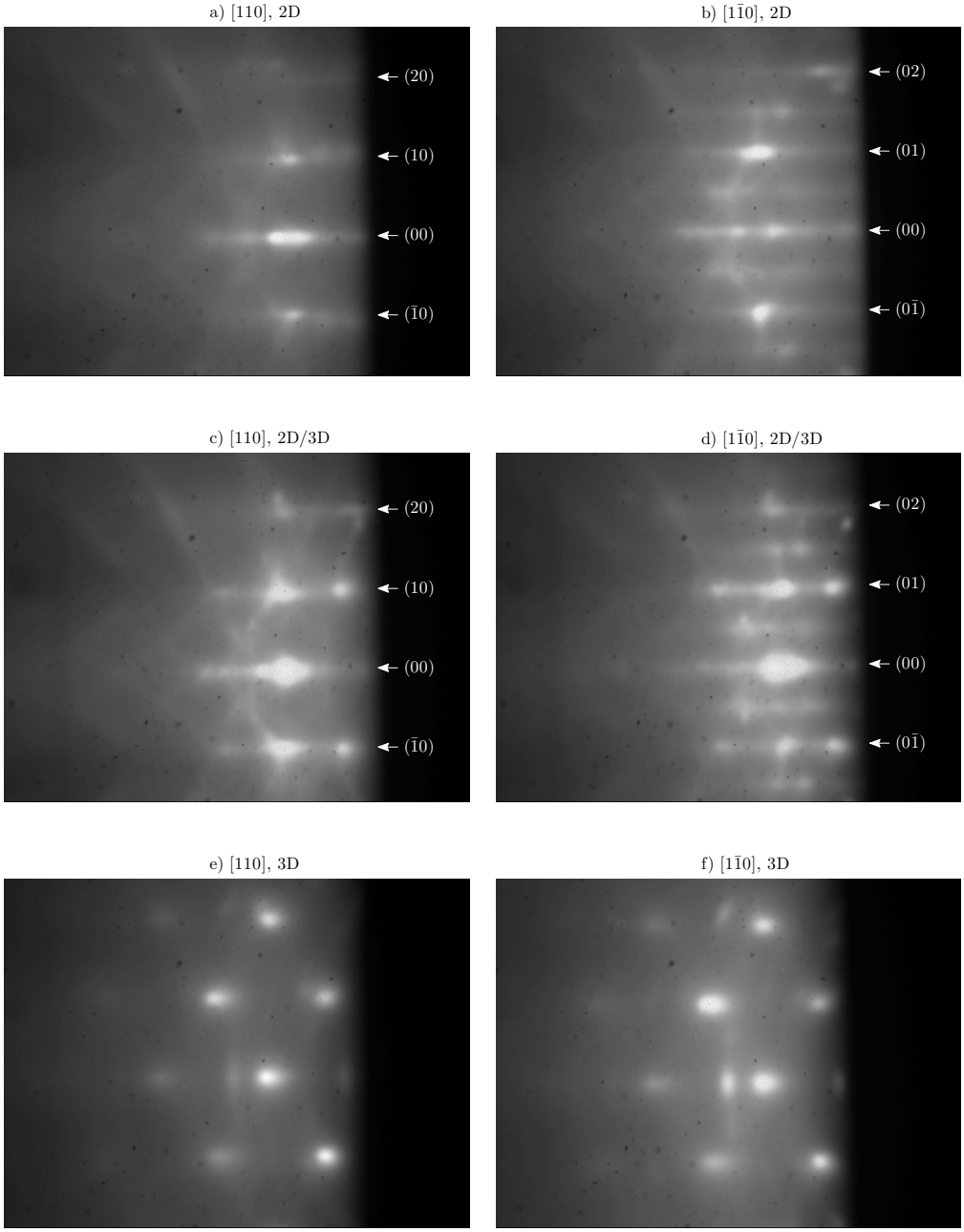

Figure 3.9: RHEED patterns acquired on samples after the growth of GaMnAs. a) and b) 2D surface, c) and d) partially roughened surface, e) and f) 3D surface. Electron beam along [110] direction - left column and along [1$\bar{1}$0] direction - right column.

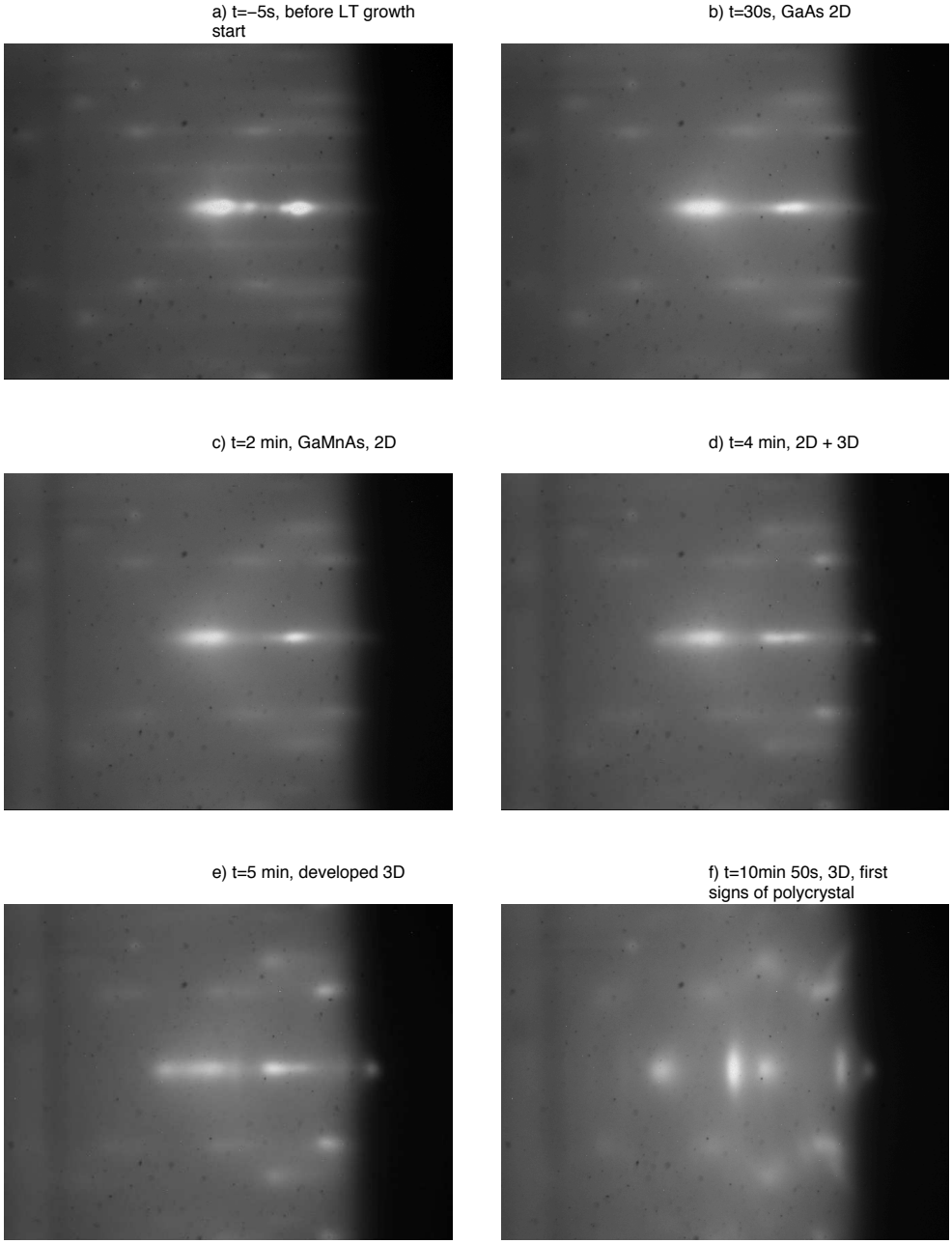

Figure 3.10: The integrated RHEED patterns acquired during the low temperature growth of GaAs buffer layer followed by the growth of GaMnAs with nominal Mn concentration 6.5%, the acquisition time was 5 seconds - equal to the time of one sample rotation.

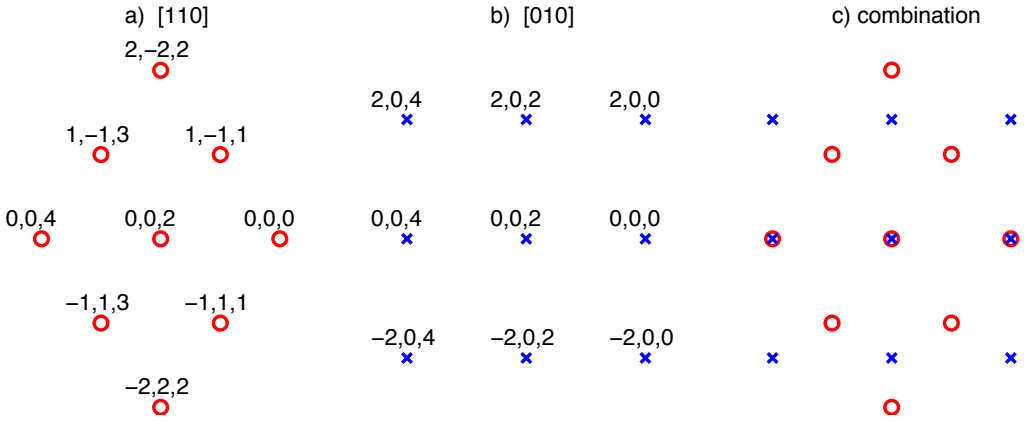

Figure 3.11: Symmetry of 3D diffraction patterns with electron beams along a) [110] and b) [010] direction. c) shows expected symmetry of integral pattern combining both a) and b).

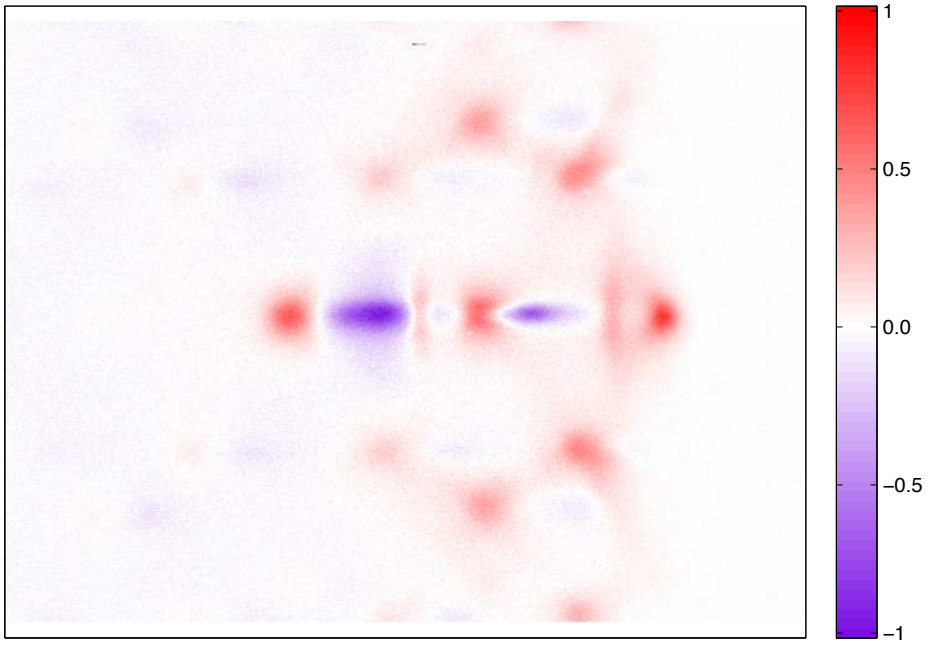

Figure 3.12: Differential image of integral patterns acquired just before the beginning of the roughening process and 2 minutes later. Red color indicate developing 3D features, blue color indicate the vanishing 2D features.

GaMnAs layers. As shown in Sec. 2.2, the integral images contain the information about dimensionality of the surface.

Particular spots can be attributed to the 2D and 3D character of the surface (see Fig. 3.12). However, the change of the the RHEED pattern is not abrupt, usually both the 2D and 3D features are observed for some period of time. Figure 3.13 illustrates a semi quantitative approach to determination of the 2D / 3D transition temperature. The images a) and b) show integrated RHEED patterns of 2D (t=30 s) and 3D (t=500 s) surfaces obtained from the video recorded during the growth of GaMnAs layer with nominal Mn doping 7%. The green rectangle is located in the way that the spot characteristic for the 2D pattern is located in its right part and the spot characteristic for the 3D pattern is located in its left part. Fig. 3.13c shows the time evolution of horizontal position of the intensity centroid of the rectangle. The change of the centroid position correspond to the progress of the surface roughening. We can see that the roughening lasts approximately 3 minutes in this case. The duration of roughening varies with the Mn concentration and with the rate of temperature increase. We define the crossing of the linear extrapolation of the evolution before and during the roughening as a point where the roughening process starts. The estimated error is ±20 second, which corresponds to roughening temperature error ±2C.

As discussed in Sec. 1.2.1, the roughening is triggered by the Mn accumulation on the surface. The above determination of roughening temperature neglects the dynamics of the accumulation process, i.e. the delay due to the accumulation of the critical amount of Mn on the surface is not considered. On the other hand, we haven't observed any pronounced dependence of the roughening temperature on the rate of the temperature increase. This suggests that the accumulation process is relatively fast and that the uncertainty caused by it lies within the experimental error.

3.2.4 Growth diagram

We used the technique described in the previous section to find the roughening temperature during the growth of GaMnAs layers with different Mn doping. The resulting growth diagram of GaMnAs is shown in Fig. 3.14. The 2D / 3D transition determines the highest possible temperature at which the GaMnAs material with a given nominal Mn concentration can be grown in the layer-by-layer mode.

The 2D / 3D boundary shown in Fig. 3.14 corresponds to the near stoichiometric ratio of As and Ga+Mn fluxes (as described is Sec. 2.1.1). The growth can be also performed with As overpressure. The magnetic properties of GaMnAs layers are best in the near stoichiometry regime. The characterization of GaMnAs layers with varying Mn concentration presented in following chapters will be focused on the properties of layers grown with the stoichiometric ratio and with substrate temperature just reaching the 2D / 3D boundary at the end of the growth.

Our growth diagram agree with diagram reported by other group [7] (Fig. 1.2). Our diagram extends the maximum Mn concentration from 9% to 13%. The

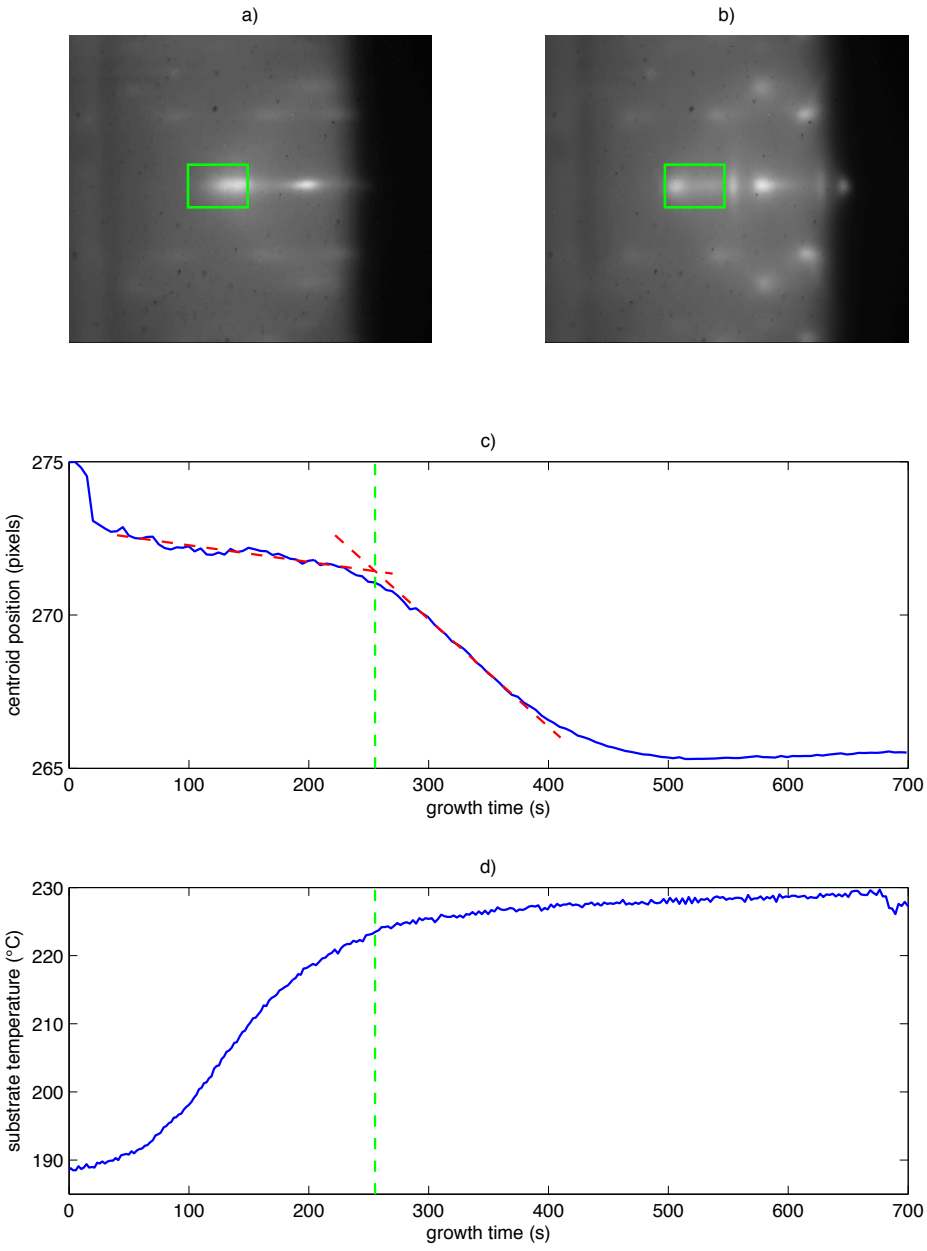

Figure 3.13: Determination of the roughening temperature. a) and b) integrated RHEED patterns of 2D and 3D surfaces, respectively. c) evolution of the intensity centroid of the area inside green rectangles indicated in a) and b). d) evolution of the substrate temperature measured by the band-gap thermometer. Vertical green lines indicate the start of the roughening process.

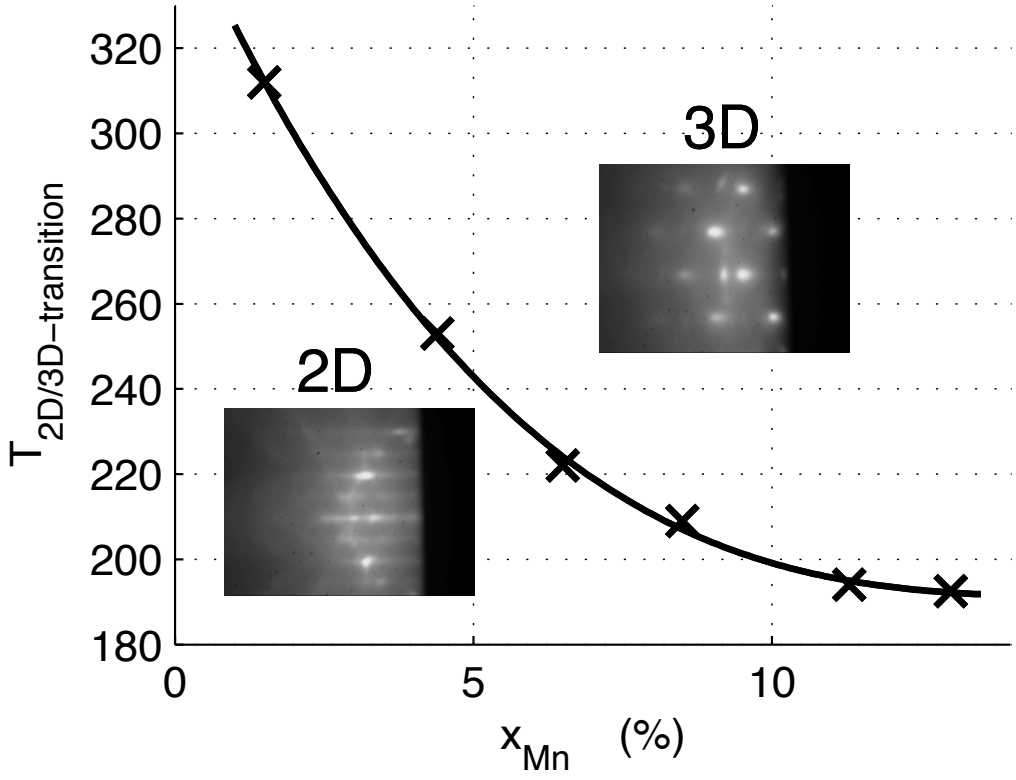

Figure 3.14: Growth diagram of GaMnAs. 2D / 3D transition temperatures were determined using the phase-locked RHEED pattern analysis and band-gap thermometry.

roughening temperature is shifted by 30°C which is probably due to the uncertainty of the thermocouple thermometer temperature values used in that study.

As discussed in detail in Sec. 4.2 the properties of the grown GaMnAs material are sensitive to the growth temperature. Again in agreement with [7] our findings show that the growth in the vicinity of the 2D / 3D boundary and with the near stoichiometric ratio results in the best magnetic properties of the prepared GaMnAs layers.

The magnetic and electrical transport properties of the layers grown under the optimal conditions are presented in the following chapters.

Chapter 4

Magnetic properties

This chapter presents the magnetic properties of GaMnAs layers.

Sec. 4.1 presents a study of magnetic properties of a series of optimally grown layers with varying Mn concentration.

In Sec. 4.2 the influence of growth temperature is investigated on a series of samples grown at various growth temperatures.

Last, a study of magnetic anisotropy of GaMnAs layers is presented in Sec. 4.3.

4.1 Curie temperature vs. nominal Mn doping

The Mn doping is the key parameter determining magnetic properties of GaMnAs. Fig. 4.1a shows the dependence of the Currie temperature T_c on the nominal Mn doping for as-grown and annealed samples. This characterization concerns standard samples, i.e. thin films of GaMnAs which were grown under optimal growth conditions defined in Sec. 3.2.4.

As expected the Curie temperature of as-grown samples is strongly reduced by the presence of Mn interstitial atoms. These defects act against the ferromagnetism of GaMnAs in two ways: they reduce the hole density and couple antiferromagnetically to neighboring substitutional Mn atoms.

We can see that the increase of Curie temperature considerably slows down with growing Mn doping both for as-grown and annealed samples when plotted against nominal Mn doping (in Fig 4.1a).

Fig. 4.1b shows the dependence of Curie temperature plotted against effective Mn concentration x_{eff} which was calculated from the low temperature magnetization of the annealed layers assuming the magnetic moment of $4.5\mu_B$ per Mn atom. In this dependence the Curie temperature still grows even for high Mn concentrations which suggests that the Curie temperature of GaMnAs layers could be increased further if we increase the amount of Mn atoms incorporated to the substitutional positions.

Table 4.1 summarizes the Curie temperatures of as-grown and annealed samples. The Curie temperatures of our layers reaches the record values reported [15]

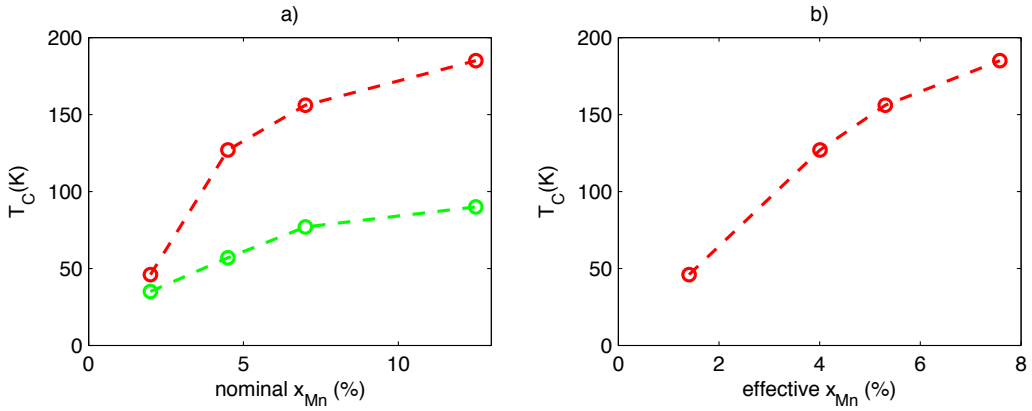

Figure 4.1: a) The Curie temperature of GaMnAs layers plotted against the nominal Mn concentration for as-grown (green) and annealed (red) samples. b) the Curie temperature of annealed GaMnAs layers plotted against the effective Mn concentration (obtained from the magnetization density).

and proves high quality of these layers.

4.2 Sample quality

4.2.1 Growth temperature

The magnetic and transport properties of GaMnAs layers depend critically on the growth temperature. To analyze the influence of the growth temperature we studied a series of four samples with the same nominal Mn doping (x_{Mn}=13%) grown at various temperatures in the vicinity of the optimal growth temperature. The growth parameters are summarized in Tab. 4.2. As discussed in Sec. 2.3 the sub-

x_{Mn} (%)	$T_C^{AG}(K)$	$T_C^{AN}(K)$	$m^{AN}(emu/cm^3)$	$x_{Mn}^{eff}(\%)$	$d(nm)$
2	35	46	13	1.4	100
4.5	57	127	37	4	50
7	77	156	49	5.3	50
12.5	90	185	70	7.6	25

Table 4.1: Table of sample parameters: the nominal Mn concentration x_{Mn}, the effective Mn concentration x_{Mn}^{eff} determined from the magnetization density of annealed layers m^{AN} assuming magnetic moment of $4.5\mu_B$ per Mn atom, the Curie temperature of as-grown T_c^{AG} samples, the Curie temperature of annealed samples T_c^{AN}, and the thickness of the layers d.

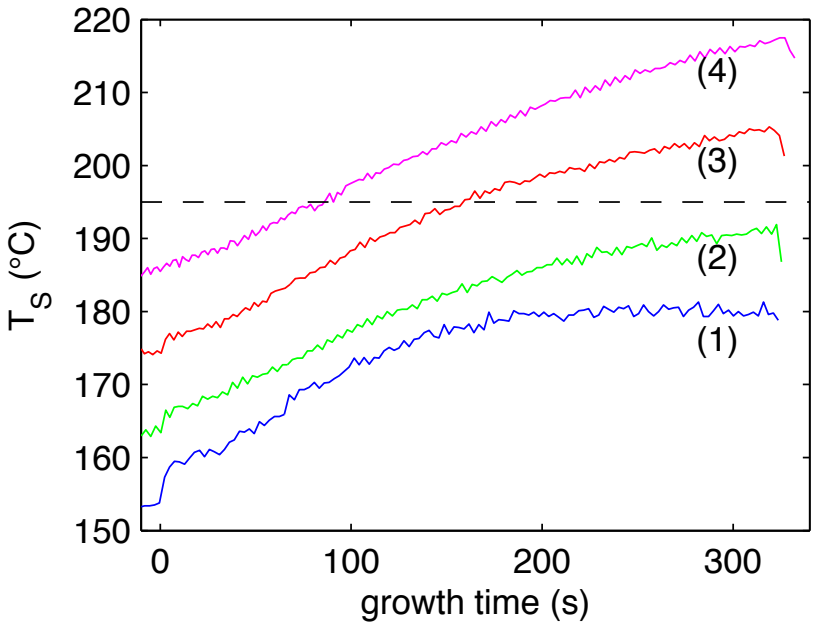

Figure 4.2: Evolutions of the sample temperature measured by the band-gap thermometer during the growth of a series of GaMnAs layers grown at various temperatures. The nominal Mn doping of layers was 13% and thickness was 20 nm. Horizontal dashed line indicates the roughening temperature.

strate temperature increases during the growth of GaMnAs layers. The substrate temperatures recorded during the growths are shown in Fig. 4.2. The horizontal line in the plot indicates the 2D / 3D transition temperature corresponding to the Mn doping of the layers. Samples 3 and 4 exceeded the roughening temperature, which was accompanied by surface roughening observed by RHEED.

To characterize the influence of the growth temperature we measured the temperature dependences of magnetization of as-grown and annealed samples. The temperature dependences of as-grown samples are shown in Fig. 4.3. Samples (2) and (3) (green and red curves) were grown very close to the optimum temperature and their behavior is similar. Sample (4) which was overheated during the growth has very similar value of T_c but considerably lower total magnetic moment (violet curve).This observation indicate that the part of the layer which was grown above the roughening temperature has poor magnetic properties. Maybe more interesting is the behavior of sample (1) which was grown at the lowest temperature (blue curve): its ferromagnetism is almost completely suppressed.

The temperature dependences of annealed samples are shown in Fig. 4.4. Samples (2) and (3) are again very similar. The optimal substrate temperature lies probably between these two growths. This agrees with a general experience that

Sample	$T_{start}(°C)$	$T_{end}(°C)$	$T_c^{AG}(K)$	$T_c^{AN}(K)$
(1)	154	180	46	157
(2)	164	191	90	181
(3)	174	205	87	179
(4)	186	217	90	157

Table 4.2: Table of sample parameters: the substrate temperature measured by the band-gap thermometer at the beginning T_{start} and at the end T_{end} of the growth of GaMnAs, the Curie temperatures of as-grown layers T_c^{AG} and annealed layers T_c^{AN}.

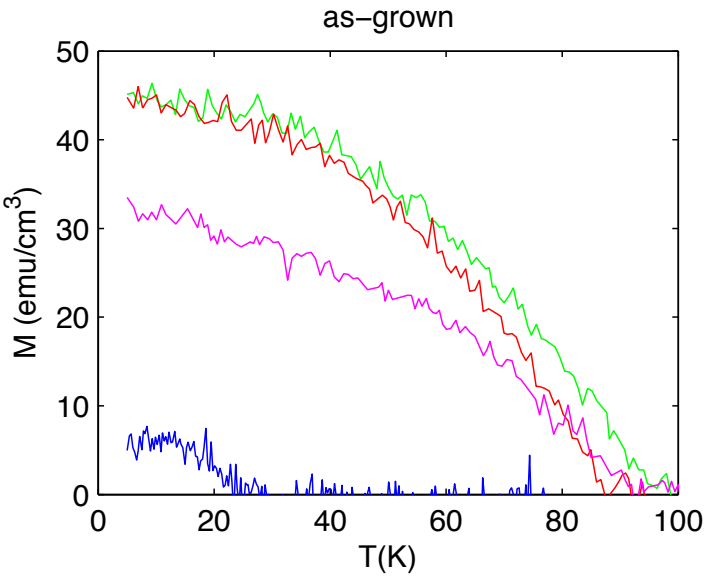

Figure 4.3: Magnetization curves of the as-grown samples grown at different temperatures (blue curve - sample (1), green curve - sample (2), red curve - sample (3), violet curve - sample (4) in Tab. 4.2 and Fig. 4.2).

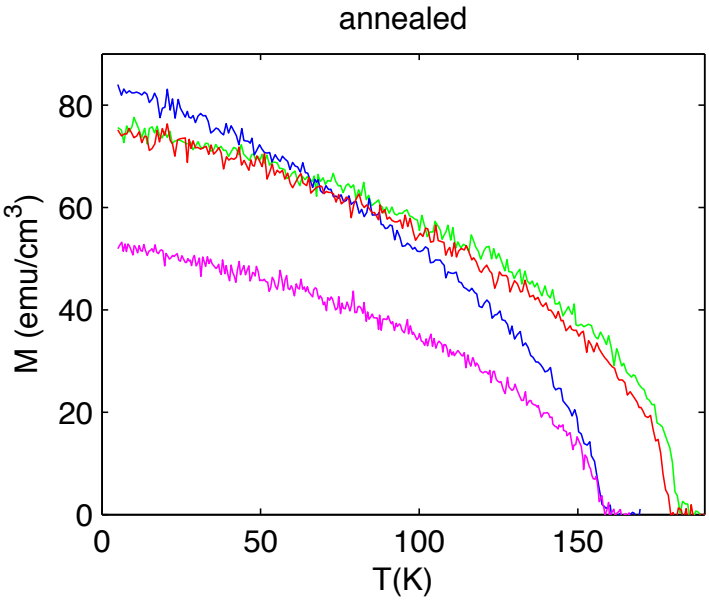

Figure 4.4: Magnetization curves of the annealed samples grown at different temperatures (blue curve - sample (1), green curve - sample (2), red curve - sample (3), violet curve - sample (4) in Tab. 4.2 and Fig. 4.2).

best samples (samples with the highest Curie temperature) are those which in the end of the growth just reach the 2D / 3D temperature for given Mn concentration.

The magnetic moment of sample (4) is again considerably smaller, its Curie temperature is also smaller compared to the samples grown close to the optimal temperature.

The most interesting behavior exhibits sample (1). The T_c of the annealed sample jumps from 26 K up to 157 K. Even more spectacular observation concerns its magnetic moment which exceeds even the samples grown close to the optimal temperature. This behavior can be explained when the As antisites are considered. The concentration of As antisites is known to grow with decreasing growth temperature [28, 63]. This explains poor magnetic properties of the as-grown sample and reduced T_c of the annealed sample. On the other hand, reduced hole density resulting from the high concentration of As antisites, allowed a higher concentration of the Mn atoms to be incorporated into the substitutional positions during the growth. This explains the observed high magnetic moment of the annealed sample.

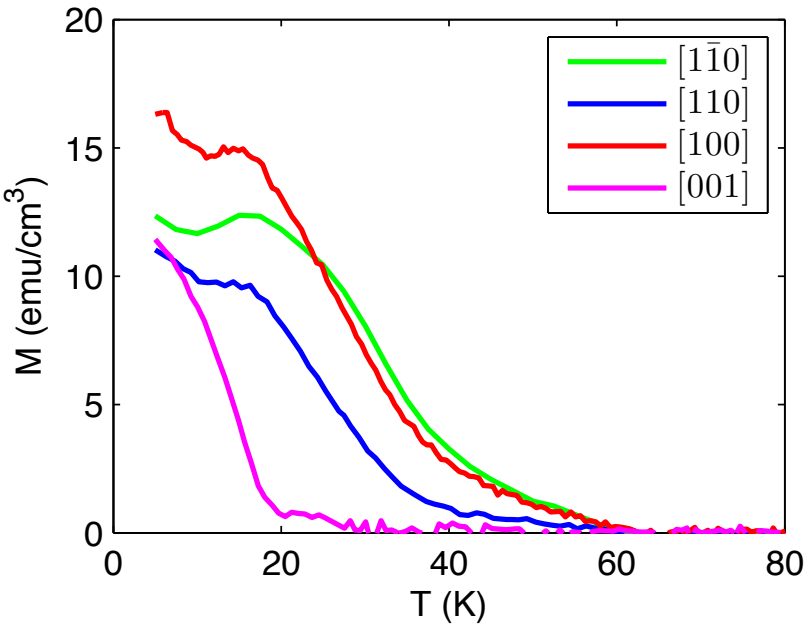

Figure 4.5: Temperature dependences measured along different crystallographic direction on 500 nm 6.5% GaMnAs layer.

4.2.2 Thick GaMnAs layers

The sensitivity of GaMnAs material to growth parameters is also reflected in the properties of thick layers. The preparation of thick layers is more difficult because the temperature change during the growth is larger and an unintentional annealing occurs during the growth.

Fig. 4.5 shows the magnetization curves of a GaMnAs layer with nominal Mn concentration 6.5% and thickness 500 nm. It can be seen that the behavior is not Brillouin like in any crystallographic direction. The magnetization gradually decreases to zero reflecting inhomogeneity of magnetic properties. Moreover, at low temperatures magnetization of part of the layer is oriented to the out-of-plane direction which is sign of very low hole density of that part of the layer [41]. The preparation of thick layers becomes more complicated with increasing Mn content.

4.3 Magnetic anisotropy

4.3.1 In-plane anisotropy

In the case of GaMnAs layers with standard doping and grown on GaAs substrates the strong and positive uniaxial out-of-plane anisotropy component prevails and

the easy axis is bound to the plane of the GaMnAs layer. The remaining in-plane magnetic anisotropy is studied in this section.

To describe only the in-plane anisotropy Eq. 1.3 can be reduced to a more convenient form describing only the in-plane cross-section of the anisotropy energy functional [64]:

$$e(\varphi) = -K_c sin^2(2\varphi)/4 + K_u sin^2\varphi - MHcos(\varphi - \varphi_H), \tag{4.1}$$

where K_c and K_u are the lowest order biaxial and uniaxial anisotropy constants, H is the external field, M is the magnetization, and φ and φ_H are the angles of magnetization and external magnetic field with respect to the $[1\bar{1}0]$ direction.

Examples of $e(\varphi)$ calculated for different combinations of cubic and uniaxial components are shown in Fig. 4.6. Fig. 4.6a shows the case of the prevailing cubic component (K_u/K_c=0.1), the easy axis is oriented close to the main crystallographic direction [100]. Fig. 4.6b shows the intermediate case (K_u/K_c=0.5), where the competition of the two components occur, the easy axis is shifted towards $[1\bar{1}0]$ direction. Fig. 4.6c shows the the case of the prevailing uniaxial contribution (K_u/K_c=1.1), the easy axis is oriented along the $[1\bar{1}0]$ direction.

Fig. 4.6d shows the shift of the easy axis orientation from the [100] direction to the $[1\bar{1}0]$ direction with increasing ratio K_u/K_c.

Figure 4.7 illustrates the influence of external magnetic field. Fig. 4.7a shows the case of a sample with a strong in-plane uniaxial component, easy axis is along $[1\bar{1}0]$ direction (φ=0°). The external magnetic field is applied along the hard axis ([110] direction, φ=90°). The shift of the energy minimum (indicated by the crosses) results in the magnetization rotation from the easy axis direction towards the hard axis direction with increasing external field. Fig. 4.7b shows the case of sample with prevailing cubic anisotropy.

We developed a code which simulates hysteresis loops based on numerical finding of energy minimum in the anisotropy potential (Eq. 4.1). The code can be used for simulation of hysteresis loops measured in arbitrary orientation and for arbitrary combination of anisotropy constants. To analyze the anisotropy of layers, we have done simultaneous simulations of hysteresis loops measured along different directions. We fitted the anisotropy constants until we got the best agreement between the measured and simulated magnetization curves.

It is necessary to stress that our simulation does not describe the switching part of the magnetization curves. When the switching occurs magnetization direction jumps from one local minimum to the other one. The switching field is determined by the domain wall dynamics, which is not considered in our simulations.

Fig. 4.8 shows the example of magnetization hysteresis loops in [110], $[1\bar{1}0]$ and [100] directions for the annealed sample with nominal Mn doping x=4.5%. The anisotropy energy calculated with constants obtained by the fit of all three hysteresis loops is shown in Fig. 4.8a. This example shows the competition between cubic and in-plane uniaxial components.

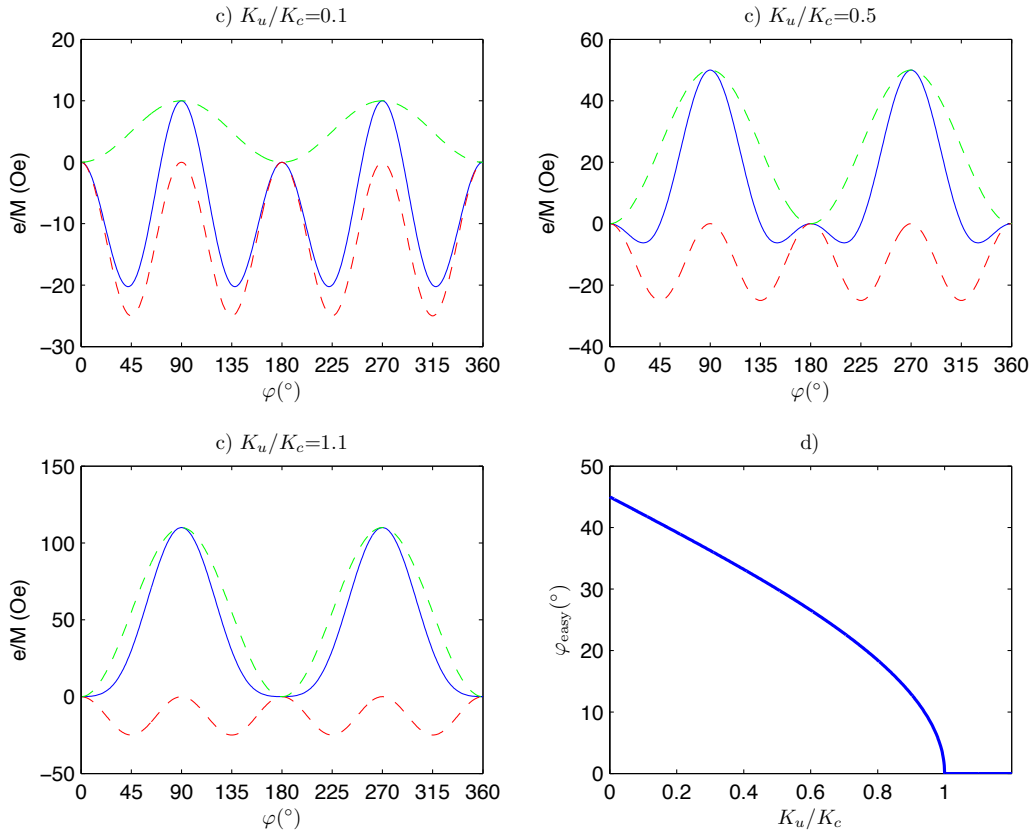

Figure 4.6: Examples of the in-plane anisotropy energy. a) dominant cubic component, 4 energy minima, b) competition between cubic and uniaxial components, 4 energy minima, shifted towards the diagonal direction, c) prevailing uniaxial component, 2 minima, d) easy axis orientation as a function of K_u/K_c. $\varphi = 0°$ corresponds to the $[1\bar{1}0]$ direction, red and green dashed curves show the contribution of cubic and uniaxial components.

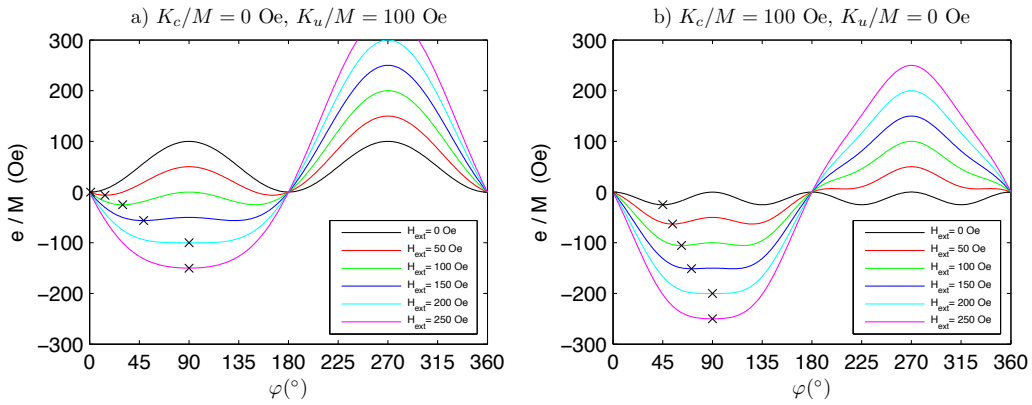

Figure 4.7: Anisotropy energy calculated with the external magnetic for a sample with uniaxial anisotropy (a) and cubic anisotropy (b). The crosses indicate the orientation of the magnetization for particular external field.

Fig. 4.9 shows the data measured for the as-grown sample with nominal Mn doping x=4.5%. The cubic component dominates the in-plane anisotropy in this case. The magnetization curves measured in the [110] and [1$\bar{1}$0] directions are almost identical.

Fig. 4.10 shows the example of the annealed sample with nominal Mn doping x=12.5%. The uniaxial component is dominating the in-plane anisotropy in this case. Zero magnetization projection in zero field is observed in the hard direction [110], while in the [1$\bar{1}$0] direction the magnetization curve shows a square hysteresis loop.

The present approach extends an analytical solution which was derived for the anisotropy constant determination from the data measured in hard axis direction (direction in which zero magnetic moment projection is measured in zero external magnetic field) [64]. The present numerical approach can be used for the anisotropy constant determination for all possible combinations of anisotropy components, in particular it can be used in the case of a strong cubic anisotropy, when no "really" hard axis can be found.

4.3.2 Low temperature results

The results of the analysis of the set of standard as-grown and annealed samples are listed in Tab. 4.3. The cubic and uniaxial constants obtained for the as-grown samples are plotted in Fig. 4.11a. It can be seen, that anisotropy of the as-grown samples is dominated by the cubic component. Its strength is decreasing with increasing Mn concentration.

Anisotropy constants obtained for the annealed samples are plotted in Fig. 4.11b. For low Mn concentrations the cubic component prevails. For high Mn concentrations the uniaxial component dominates.

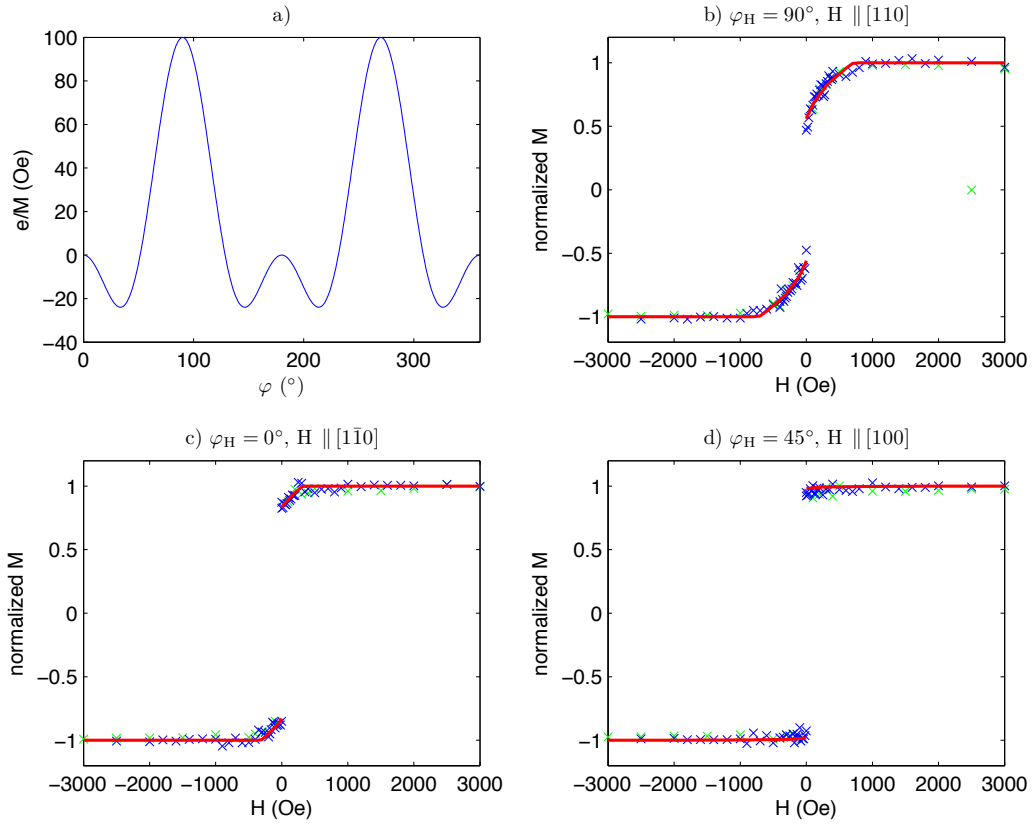

Figure 4.8: Magnetization curves measured on the annealed sample with nominal concentration 4.5% along b) [110], c) [1$\bar{1}$0], and d) [100] directions, red curves show the fit of the magnetization used for the extraction of anisotropy constants, a) shows the in-plane cross section of the anisotropy energy functional. Example of competition between cubic and uniaxial components.

	as-grown		annealed	
x_{Mn} (%)	K_c/M (Oe)	K_u/M (Oe)	K_c/M (Oe)	K_u/M (Oe)
2	948	94	723	75
4.5	606	30	257	100
7	521	42	105	194
12.5	538	100	3	241

Table 4.3: Table of anisotropy constants obtained from fits of field dependences of magnetization measurements for as-grown and annealed samples with different Mn concentrations x_{Mn}. Measurements were done at the temperature of 5K.

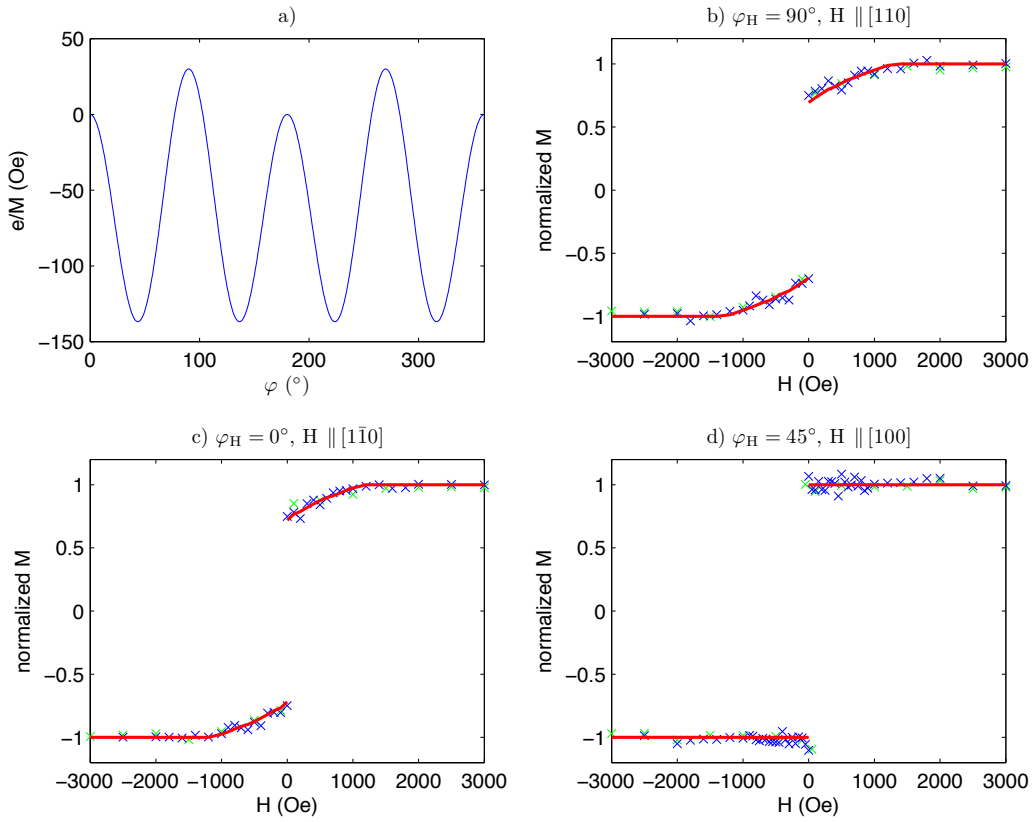

Figure 4.9: Magnetization curves measured on the as-grown sample with nominal concentration 4.5% along b) [110], c) [1$\bar{1}$0], and d) [100] directions, red curves show the fit of the magnetization used for the extraction of anisotropy constants, a) shows the in-plane cross section of the anisotropy energy functional. Example of layer with prevailing cubic anisotropy.

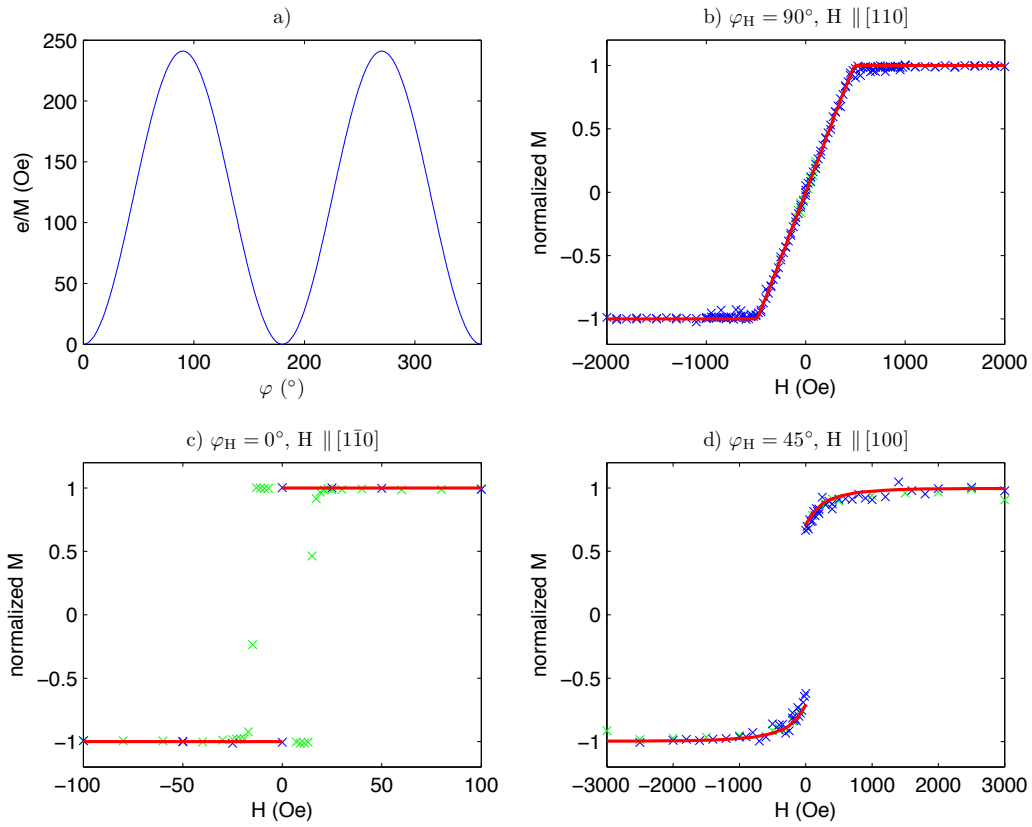

Figure 4.10: Magnetization curves measured on the annealed sample with nominal concentration 12.5% along b) [110], c) [1$\bar{1}$0], and d) [100] directions, red curves show the fit of the magnetization used for the extraction of anisotropy constants, a) shows the in-plane cross section of the anisotropy energy functional. Example of layer with prevailing uniaxial anisotropy.

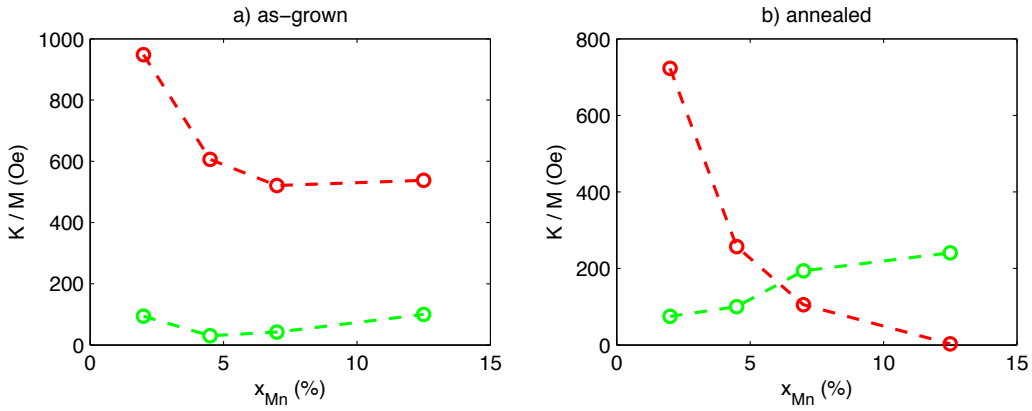

Figure 4.11: Cubic (K_c, red) and uniaxial (K_u, green) anisotropy constants determined for a series of a) as-grown and b) annealed samples with different nominal Mn concentration x_{Mn}.

To summarize, the cubic anisotropy component weakens with increasing Mn content and annealing, while the in-plane uniaxial component strengthens with increasing Mn doping and with the annealing.

The results obtained by the presented approach are consistent with anisotropy analyses of GaMnAs layers reported by other groups [41], [64], including the analyses done by ferromagnetic resonance [65].

4.3.3 Errors

The errors in the determination of the anisotropy constants have several different sources:

- Quality of the sample, the anisotropy constants can be determined only as long as the layer is homogeneous.
- Orientation of samples in the SQUID magnetometer, this error is typically less than 5°.
- Quality of the data measured by the magnetometer. This error can be suppressed by measurement of numerous points in the hysteresis loop or by repeated measurement, if it is necessary.
- Contamination of the sample or sample holder by magnetic materials.
- Condensation of gases occurring in the cryostat of the magnetometer. Especially condensation of oxygen can become important during SQUID measurements, because solid oxygen exhibit complex magnetic behavior. Its influence needs to be taken into account when the diamagnetic background is subtracted from the measured data.

When the anisotropy constants are extracted from the data measured along different directions, the influence of the systematic errors can be reduced or eliminated as they mostly result in obvious inconsistency during the fitting procedure. It is necessary to mention, that if one of the components dominates, the determination of the weaker component becomes very inaccurate. The absolute error of both anisotropy constants is approximately 10% of the value of the stronger component.

4.3.4 Temperature dependence of anisotropy

The temperature dependence of magnetic anisotropy components can be roughly characterized from the temperature dependences of magnetization measured in different directions. The magnetization curves measured for standard as-grown samples are shown in Fig. 4.12, the curves measured for the annealed samples are shown in Fig. 4.13. The temperature dependent magnetization curves were measured in field 20 Oe. The magnetization measured in this field is still very close to the spontaneous magnetization and at the same time the influence of parasitic fields is suppressed.

In the case of as-grown samples, the easy axis lies between [100] and $[1\bar{1}0]$ direction at low temperatures, which is a result of strong cubic anisotropy component. From the difference between the [110] and $[1\bar{1}0]$ directions we can see that with increasing temperature the ratio between cubic and uniaxial components decreases and the uniaxiality of the magnetic anisotropy is more pronounced. In region near the Curie temperature both the anisotropy components weaken. When the anisotropy fields become smaller compared to the field applied during the measurement (20 Oe), the moments measured in all directions become the same.

In the case of low doped annealed layers (2% and 4.5%) the behavior is similar to the behavior of as-grown samples. For highly doped annealed samples the uniaxial anisotropy prevails for all temperatures.

We studied in detail the temperature dependence of anisotropy of the layer with the nominal Mn doping 12.5%. Fig. 4.14 shows the temperature dependence of the anisotropy constants of as-grown and annealed samples. These constants were obtained from hysteresis loops measured at different temperatures. Very fast decrease of the cubic anisotropy with the increasing temperature can be observed in the case of as-grown sample. The uniaxial contribution weakening is slower, which results in the rotation of the easy axis from the [100] direction to the $[1\bar{1}0]$ direction. This result agree with the evolution of the remnant magnetization shown in Fig. 4.12d.

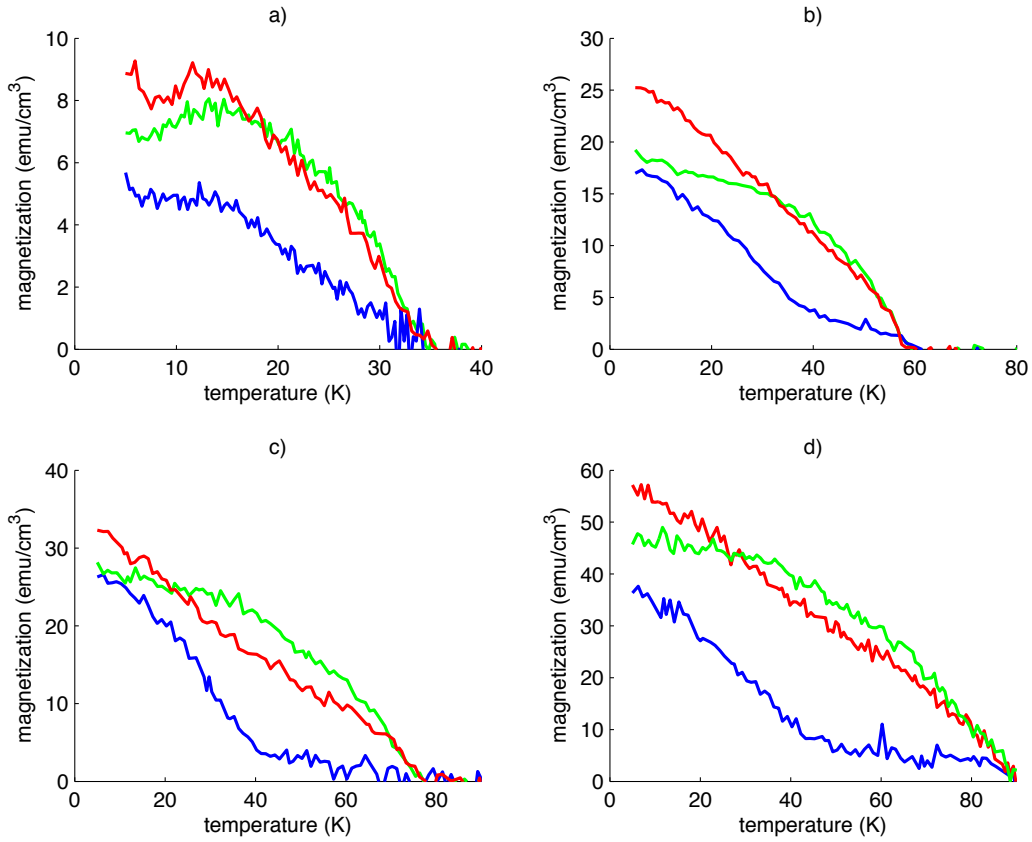

Figure 4.12: Temperature dependences of magnetic moment measured along [110] (blue), [1$\bar{1}$0] (green) and [100] (red) directions for the series of as-grown samples with the nominal Mn doping a) 2%, b) 4.5%, c) 7%, d)12.5%.

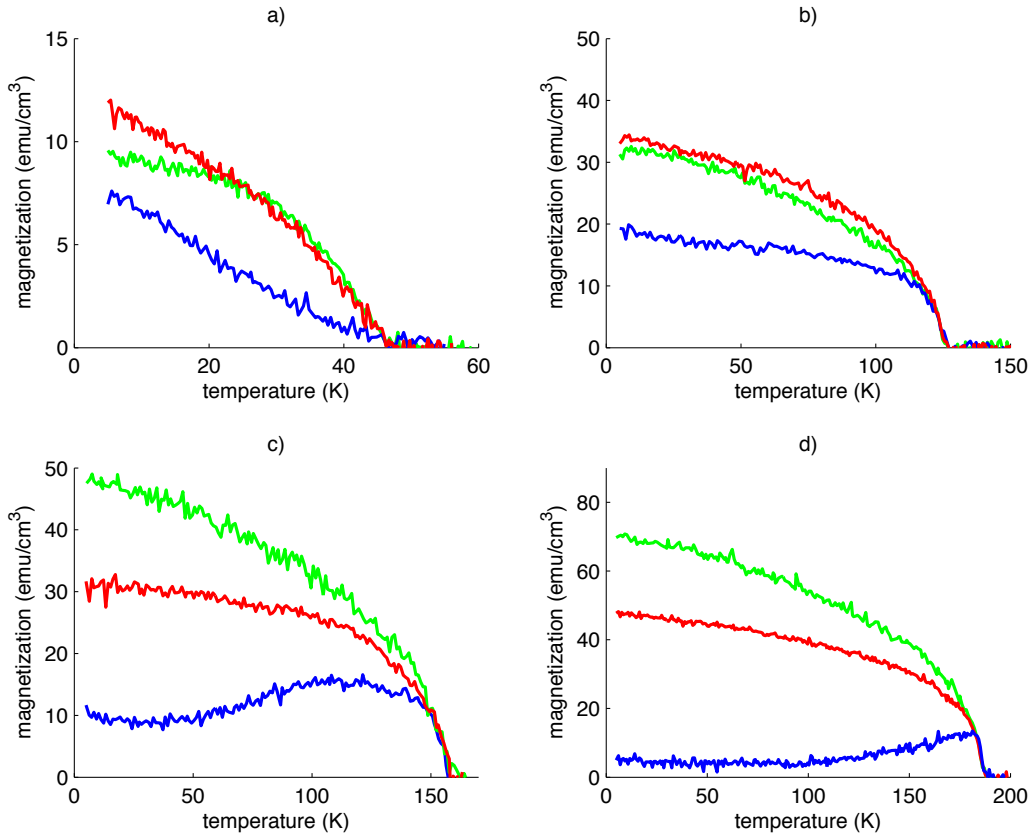

Figure 4.13: Temperature dependences of magnetic moment measured along [110] (blue), [1$\bar{1}$0] (green) and [100] (red) directions for the series of annealed samples with nominal Mn doping a) 2%, b) 4.5%, c) 7%, d)12.5%.

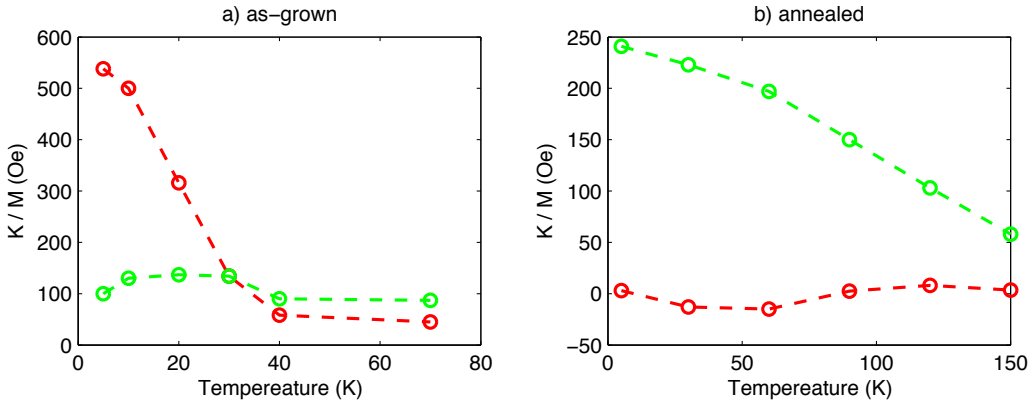

Figure 4.14: Temperature dependences of the cubic (red) and uniaxial (green) anisotropy constants determined for the as-grown a) and annealed b) samples with nominal Mn concentration x_{Mn}=12.5%. The values were determined from fits of field dependences of magnetization measured at different temperatures.

4.3.5 Out-of-plane anisotropy

To complete the picture of magnetic anisotropies of the GaMnAs layers studied in previous sections, lets briefly investigate the out-of-plane anisotropy. The out-of-plane anisotropy component can be determined from the hysteresis loops measured in the out-of-plane direction. Magnetic field dependences of the magnetic moment measured on the annealed samples with varying Mn content are shown in Fig. 4.15a.

The out-of-plane direction is the hard direction for all the samples. The magnetization drops to zero in zero magnetic field. From the saturation field H_{sat} the out-of-plane anisotropy constant can be obtained as $K_{un}^{out}/M = H_{sat}/2 - 2\pi M$, where the term $2\pi M$ is the shape anisotropy correction [39] . Resulting anisotropy constants are shown in Fig. 4.16a.

Fig. 4.16b shows the temperature dependence of the out-of-plane anisotropy component of the annealed sample with nominal Mn concentration 12.5%. These values were determined from magnetic field dependences of magnetic moment oriented to the out-of-plane direction measured at different temperatures (shown in Fig. 4.15b).

The in-plane easy axis orientation is in agreement with expected behavior of the strain induced out-of-plane magnetic anisotropy of GaMnAs layers grown on GaAs substrates [39]. The obtained anisotropy constants are comparable with other reported values [65, 66].

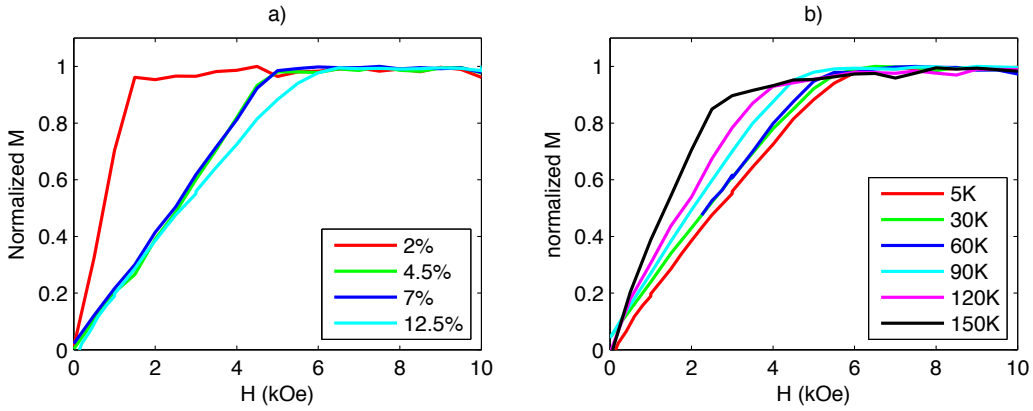

Figure 4.15: a) Field dependences of magnetization measured at 5 K in the out-of-plane direction for the series of annealed samples with different Mn concentrations. b) Field dependences measured in the out-of-plane direction for the annealed sample with nominal Mn doping 12.5% at temperatures between 5 K and 150 K.

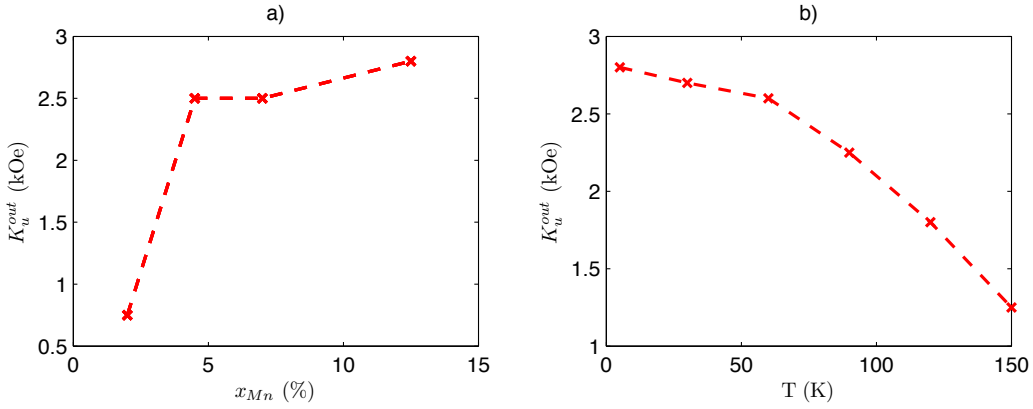

Figure 4.16: a) Out-of-plane anisotropy constants K_u^{out} of annealed samples with different nominal Mn doping measured at 5 K, b) temperature dependence of K_u^{out} of the annealed sample with nominal Mn doping 12.5%.

Chapter 5

Transport properties

This chapter presents the electrical transport properties of GaMnAs layers.

Section 5.1 describes the metal-insulator transition of GaMnAs.

In Sec. 5.2 the conductivity measurements of metallic GaMnAs layers with varying Mn content are presented and trends are discussed.

In Sec. 5.3 the temperature dependence of the resistivity of GaMnAs layers is studied. The singularity of the temperature derivative of resistivity occurring at Curie temperature is pointed out and its origin is discussed.

5.1 Metal-insulator transition of GaMnAs

The acceptor level of the substitutional Mn is 110 meV above the top of the valence band, Mn is referred as a relatively deep acceptor. With increasing Mn concentration the Mn impurity band broadens and shifts down towards the valence band. Until the Mn band reaches the top of the valence band the GaMnAs material exhibits semiconductor properties. When the Mn band merges the valence band of host GaAs, the GaMnAs material becomes metallic [67].

Resistivity of samples with nominal Mn concentrations 0.07%, 1.0%, 2% and 7% are shown in Fig. 5.1. The samples with Mn doping 0.07% and 1.0% show clear semiconductor behavior with diverging low temperature resistivity. Samples with Mn doping 2% and 7% show metallic behavior with finite low temperature resistivity.

5.2 Conductivity of metallic GaMnAs layers

The conductivities of as-grown and annealed GaMnAs layers with varying Mn concentration are listed in Tab. 5.1 and shown in Fig. 5.2. When plotted against nominal Mn doping the conductivity of annealed samples saturates, for the as-grown samples the conductivity even decreases for high Mn doping. This observation is in agreement with the expected self-compensation of the material by Mn interstitials and As antisites [4].

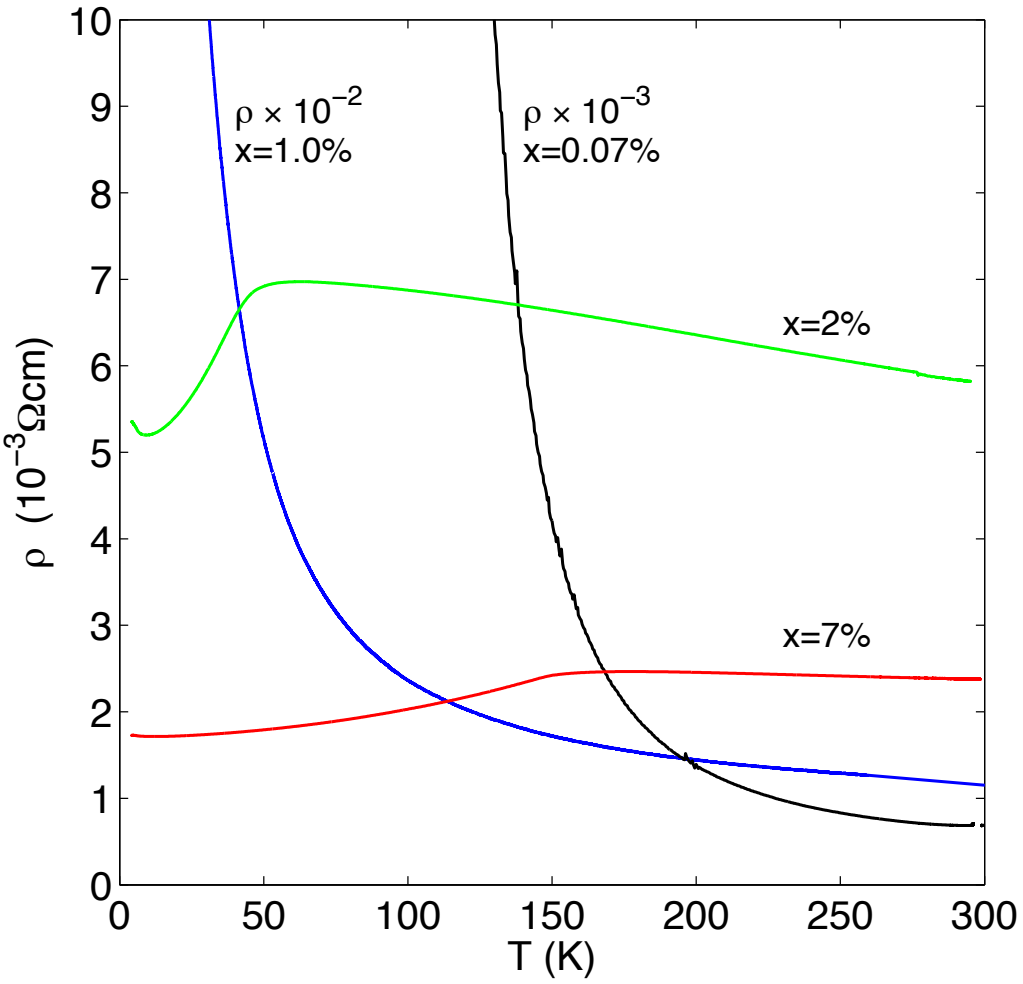

Figure 5.1: Metal-insulator transition in GaMnAs: semiconductor behavior of GaMnAs layers with low Mn doping (x=0.07%,x=1%), metallic behavior of GaMnAs layers with high Mn doping (x=2%, x=7%).

x_{Mn} (%)	$\sigma(\Omega^{-1}cm^{-1})$ as-grown	$\sigma(\Omega^{-1}cm^{-1})$ annealed
2	122	172
4.5	151	358
7	176	421
12.5	150	435

Table 5.1: Room temperature conductivities of as grown and annealed layers, with varying nominal Mn doping x_{Mn}. For magnetic properties of layers see Tab. 4.1

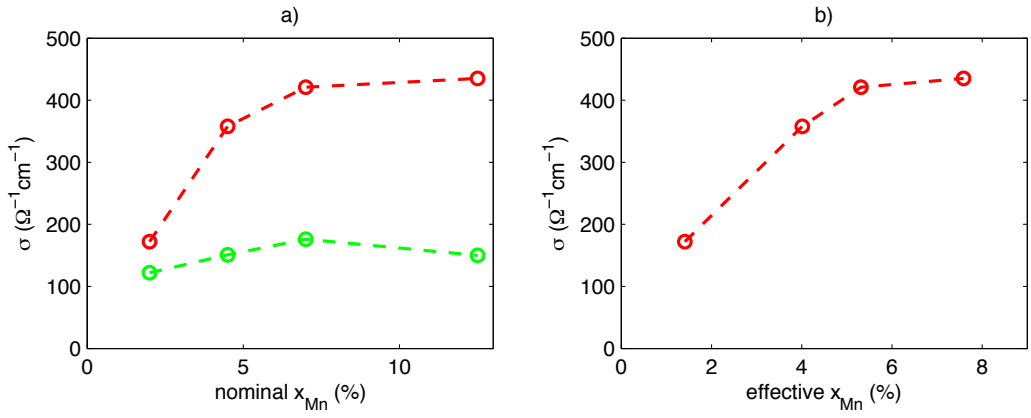

Figure 5.2: a) Room temperature conductivities of as-grown (green dependence) and annealed (red dependence) GaMnAs layers plotted against the nominal Mn concentration, b) conductivities of annealed samples plotted against the effective Mn concentration obtained from magnetometry data.

In the case of annealed samples, the compensation due to the Mn interstitials is removed. Fig. 5.2b shows the conductivities of annealed samples plotted against the effective (substitutional) Mn concentration obtained from the magnetometry measurements of the annealed samples. The conductivity is monotonically increasing function of effective Mn concentration, but its increase again slows down for high Mn concentrations. This behavior can be attributed to the increasing As antisite concentration and to the decreasing hole mobility in highly doped GaMnAs.

5.3 Temperature dependence of resistivity

The temperature dependence of resistivity reveals information about the magnetism of GaMnAs layers [16].

Fig. 5.3b shows temperature dependences of resistivity of series of GaMnAs layers with different Mn concentration. All the samples exhibit metallic behavior:

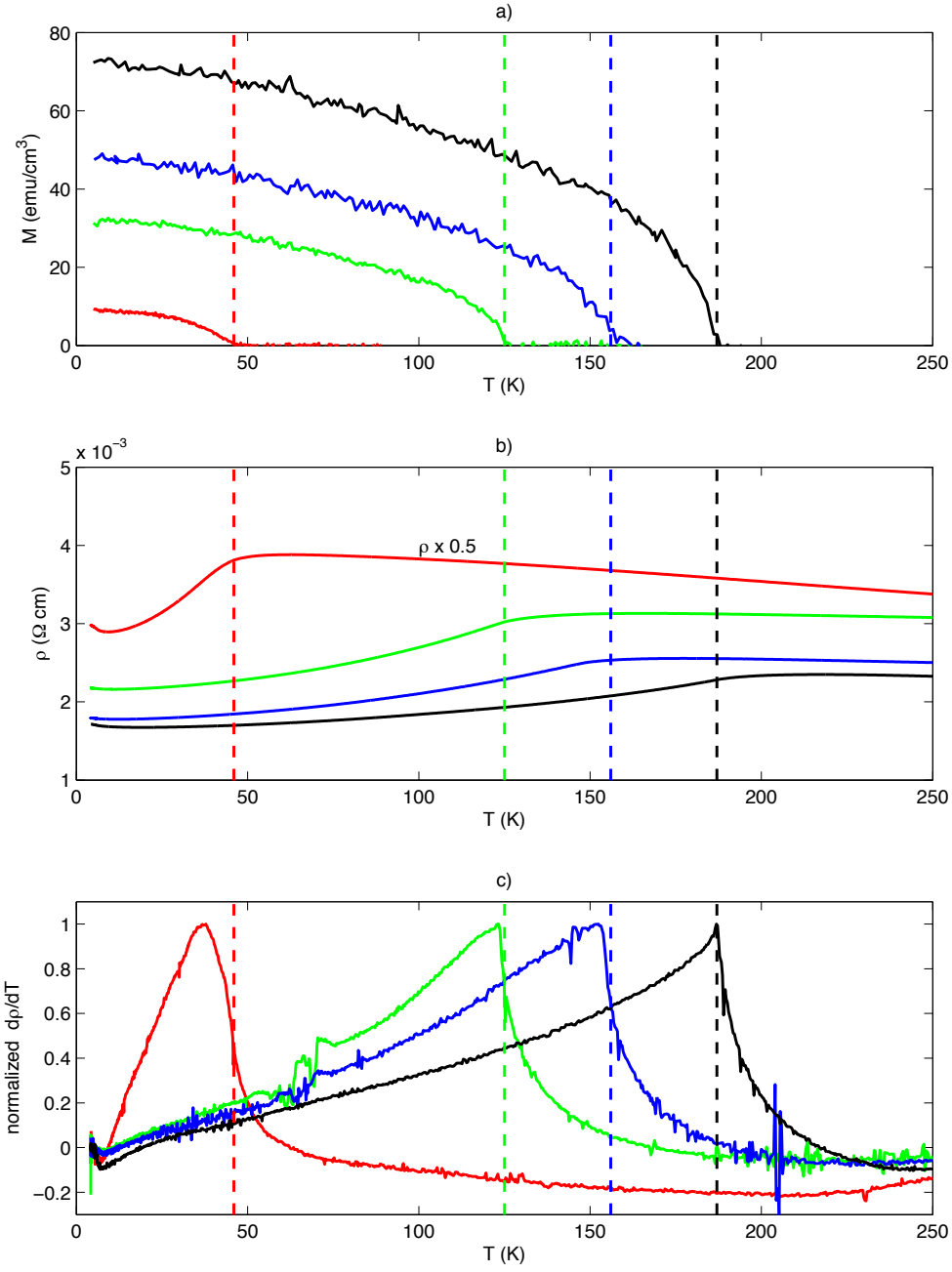

Figure 5.3: a) Magnetization of samples measured along [1$\bar{1}$0] direction, b) temperature dependence of resistivity, c) temperature derivatives of resistivity. Vertical lines indicate Curie temperatures obtained from magnetometry measurements. The data were measured on annealed samples with nominal Mn concentration 2% (red), 4.5% (green), 7% (blue), and 12.5% (black).

their resistivity changes by less than 30% between the room temperature and the liquid helium temperature, exhibiting a very broad maximum of resistivity at temperatures above the Curie temperature. The Curie temperatures of the layers were determined from the temperature dependences of magnetization shown in Fig. 5.3a.

Fig. 5.3c shows the temperature derivative of resistivity. These curves show a sharp cusp singularity at the Curie temperature for samples with Mn doping 4.5%, 7% and 12.5%. In the case of very low Mn doping the singularity is suppressed, usually only a remnant of the singularity is seen as an abrupt change of the slope at the Curie temperature (as in the case of the layer with Mn concentration 2%).

The differences between Curie temperatures determined by the magnetometry measurements and the position of the singularity in the temperature derivative of resistivity are typically several K and can attributed to the differences of particular samples (different pieces of the same wafer were used for the measurements) and to the cross-calibration uncertainty of temperatures in magnetometer and in the cryostat for transport measurement.

The temperature dependence of the resistivity is determined by the carrier scattering rate on magnetic fluctuations in the vicinity of the Curie temperature. In the ferromagnetic regime, the scattering is proportional to the uncorrelated spin fluctuations and the temperature dependence scales with M^2. On the paramagnetic side, a broad shoulder on the temperature dependence of the resistivity can be observed. This behavior is consistent with theory developed for electronic transport properties of ferromagnetic metals with high carrier density i.e. large Fermi vector, where the scattering on spin waves with short wavelengths is dominant and grows even above the Curie temperature. The singularity of the $d\rho/dT$ is expected at the Curie temperature [68].

This behavior is in contrast to the behavior of magnetic semiconductors with low concentration of free carriers (e.g. Eu-chalcogenides), where the maximum in the resistivity is observed at T_c [69].

The temperature derivative of resistivity can be used for relatively precise determination of T_c of GaMnAs. This possibility is very interesting for the T_c determination in the case of very thin layers and of micro or nano-devices, where even the SQUID sensitivity is not sufficient. We published the result concerning temperature of GaMnAs layers in [16].

Chapter 6

Annealing

This chapter concerns the aspects of the annealing of GaMnAs layers.

A typical example of the effect of annealing on the magnetic and transport properties of a GaMnAs layer is shown in Sec. 6.1.

In Sec. 6.2 the Mn interstitial density of GaMnAs layers with varying Mn concentration is estimated from the change of conductivity due to the annealing.

In Sec. 6.3 the effect of surface oxide removal on the efficiency of annealing is studied. The magnetometry and transport measurements indicating important role of the surface oxide layer are presented.

In Sec. 6.4 an XPS study of the GaMnAs layers subjected to surface oxide etching and annealing is presented. The Mn accumulation in the surface occurring during the annealing is studied in detail.

Sec. 6.5 summarizes the results of Sec. 6.3 and 6.4 and discusses the processes occurring during the annealing.

6.1 Effect of annealing

The example of the annealing effect for a GaMnAs layer with nominal Mn doping $x = 12\%$ and thickness 25 nm is shown in Fig. 6.1. Fig. 6.1a shows the temperature dependences of magnetization measured in different stages of the annealing at temperature 160°C. Fig. 6.1b shows the corresponding temperature dependences of the electrical resistivity. It can be seen that the annealing substantially improves both the magnetic properties (the Curie temperature and the magnetization density) and the conductivity of the layer.

6.1.1 Thick layers

The above examples show the standard behavior of thin layers subjected to the low temperature annealing. It is worth mentioning that the situation is much less clear in the case of the annealing of thicker layers of GaMnAs ($t \geq 100\,\mathrm{nm}$). As discussed in section 4.2, the magnetic properties of the as-grown samples are rather

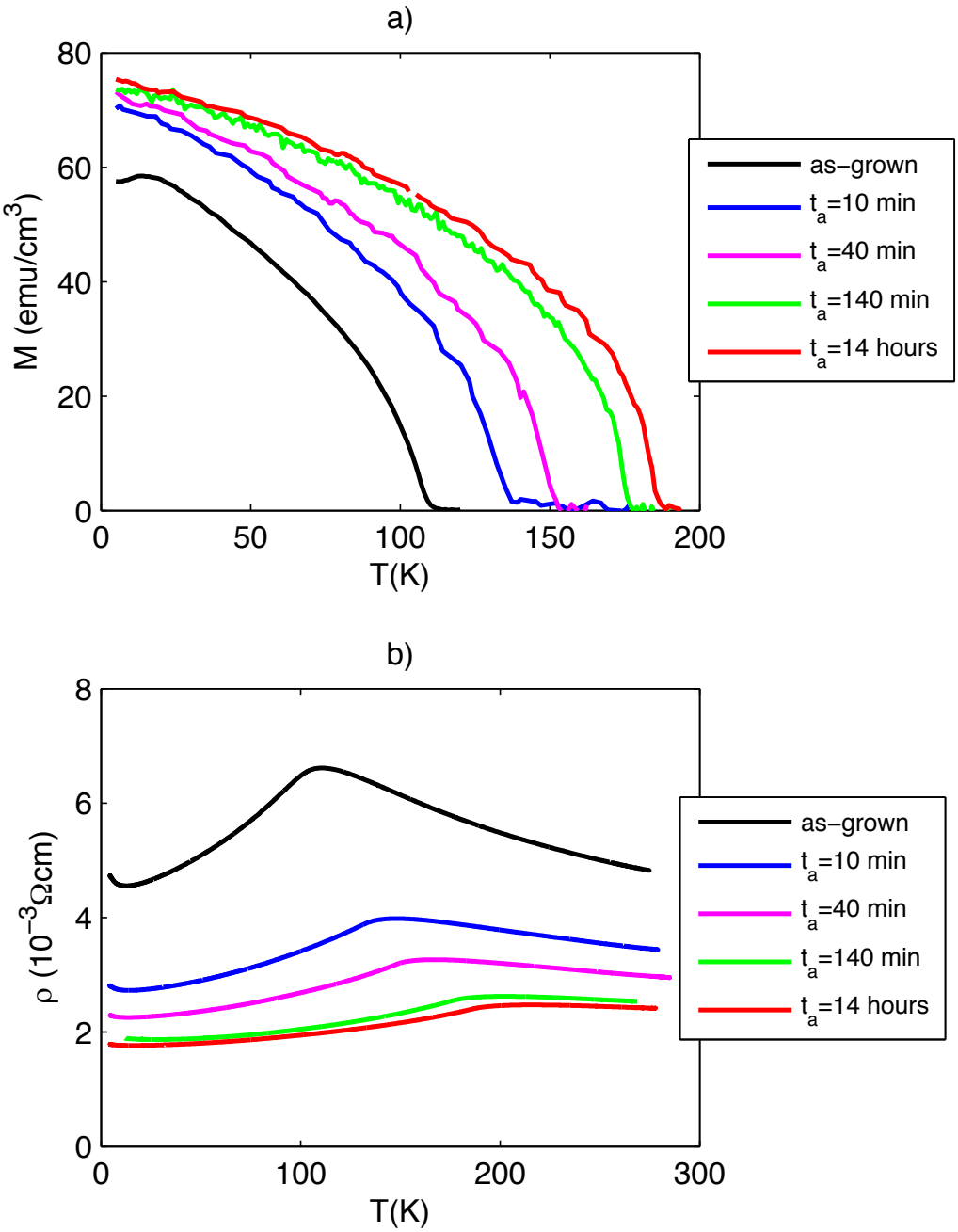

Figure 6.1: a) Temperature dependences of magnetization of GaMnAs layer with nominal Mn doping 12% subjected to annealing at 160°C measured at different stages of annealing, b) corresponding temperature dependences of resistivity.

x_{nom} (%)	$\Delta\sigma(\Omega^{-1}cm^{-1})$	μ $(cm^2V^{-1}s^{-1})$	x_{int}(%)
2	50	5.0	0.14
4.5	207	3.4	0.86
7	245	2.75	1.3
12.5	285	2.7	1.5

Table 6.1: Table of Mn intersitial densities x_{int}, determined for the series of samples with varying nominal Mn concentration x_{nom}, from the difference of the conductivity $\Delta\sigma$ of as-grown and annealed samples (listed in Tab. 5.1) and using mobilities μ obtained from literature [67].

complex due to very long time of growth during which the unintentional annealing occurs and due to the change of the growth temperature.

The annealing of thick layers also results in substantial improvement of their magnetic and transport properties. Nevertheless, the quality of annealed thick layers does not reach the quality of their thin, well-behaved counterparts. For example, we observed difference of Curie temperature as large as 50 K between two annealed layers with thickness 25 nm and 100 nm in the case of nominal Mn doping $x = 13\%$.

6.2 Mn interstitial density

The change of conductivity of the GaMnAs layer subjected to the low temperature annealing can be used for the estimate of the Mn interstitial density of the as-grown sample. The room temperature conductivities of series of as-grown and annealed samples are listed in Tab. 6.1.

The hole density of GaMnAs material can be written as:

$$p = (x_{sub} - 2x_{int} - 2y) \cdot N \tag{6.1}$$

where x_{sub} is the concentration of substitutional Mn, x_{int} is the concentration of interstitial Mn, y is the concentration of arsenic antisites, and N is the cation atom density ($N = 2.21 \times 10^{22}\,\mathrm{cm}^{-3}$).

The conductivity σ is given by:

$$\sigma = p\mu e \tag{6.2}$$

where μ is the hole mobility and e is the electron charge.

Assuming that all the Mn interstitial atoms are removed by the annealing we obtain the following expression for the Mn interstitial concentration of the as-grown layer x_{int}:

$$x_{int} = \frac{\Delta\sigma}{2\mu e N} \tag{6.3}$$

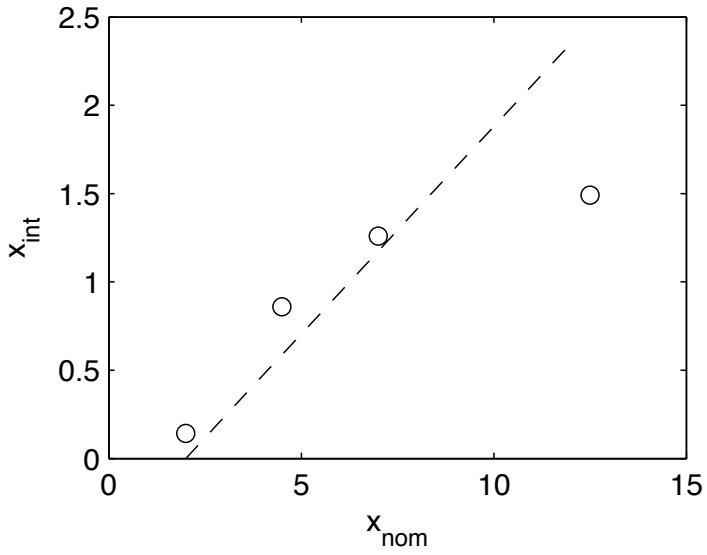

Figure 6.2: Density of interstitial Mn vs. nominal Mn doping estimated from the difference of the conductivity of GaMnAs layers before and after annealing (circles), compared to theoretical prediction [4] (dashed line).

where $\Delta\sigma$ is the change of conductivity due to the annealing, x_{sub} is the concentration of substitutional Mn, x_{int} is the concentration of interstitial Mn, y is the concentration of arsenic antisites, and N is the cation atom density.

The mobilities used in the following calculation were taken from literature [67] and are listed in Tab. 6.1.

The Mn interstitial densities calculated using Eq. 6.3 are shown in Fig. 6.2. The dashed line is the theoretical expectation [4].

Apart from the sample with the highest Mn concentration the experimental results compare well with the theoretical prediction. In the case of sample with $x = 12.5\%$, the experimental Mn concentration is considerably lower compared to the theoretically expected value. This suggests that for highly doped samples (grown at very low temperatures) the As antisite compensation starts to be more pronounced. It should be mentioned, however, that some part of the difference could be attributed to the uncertainty of the nominal Mn concentration coming from the Mn flux calibration and to the possible error of the mobility which was used in the calculation.

6.3 Surface oxide etching

Figure 6.3 shows the influence of repeated surface oxide etching on the efficiency of low temperature annealing of a GaMnAs layer with nominal Mn doping $x = 7\%$

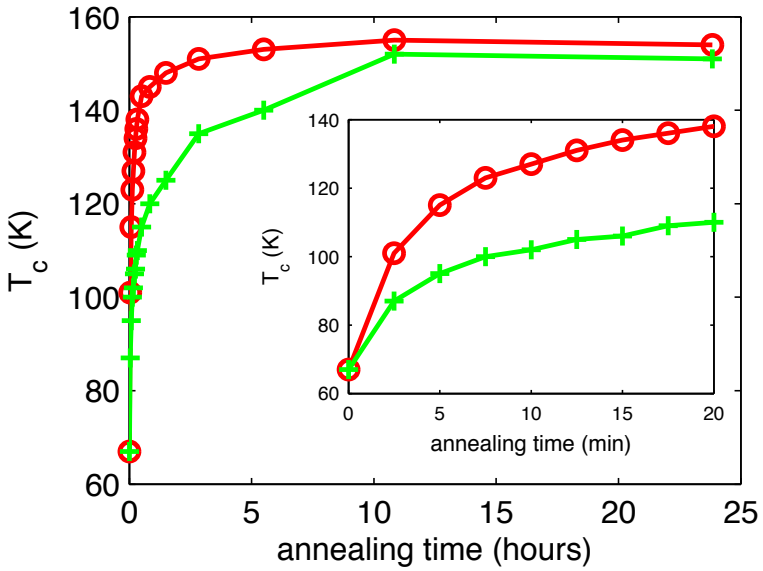

Figure 6.3: The evolution of T_c of a GaMnAs layer with nominal Mn doping $x = 7\%$ and thickness 50 nm which was subjected to standard annealing (green dependence), compared to the evolution of sample subjected to etch-anneal procedure (red dependence). The etching was performed before each annealing step.

and thickness 50 nm. The evolutions of Curie temperatures in the case of standard annealing and in the case of etch-annealing procedure are compared. It can be clearly seen that the annealing process is dramatically faster in the case of the etch-annealing procedure. For example $T_c = 140$ K is reached in 20 minutes in the case of etch-annealed sample, while the annealed sample needs 5 hours to reach this value of T_c.

The oxide removal procedure consisted of 30 s etching in 35% HCl acid and subsequent water rinsing. The HCl acid is known to etch GaAs oxide, while leaving GaAs intact. Samples were annealed on a hot plate at the temperature of 200°C. The Curie temperatures were measured by SQUID magnetometry. During the first 20 minutes of the annealing (shown in inset of the figure) the etching was repeated in intervals of 150 seconds. In the following annealing the intervals of annealing were prolonged, sample was etched after each SQUID magnetometry measurement shown in Fig. 6.3.

The etching procedure was done several minutes before next annealing. The enhancement of annealing efficiency was not sensitive to the time between etching and annealing. Similar annealing efficiency was observed for the delay between etching and annealing in the range of 1 minute and 10 hours.

The maximum values of Curie temperature achieved by both of the procedures are comparable, nevertheless the T_c of the etch-annealed sample is measurably

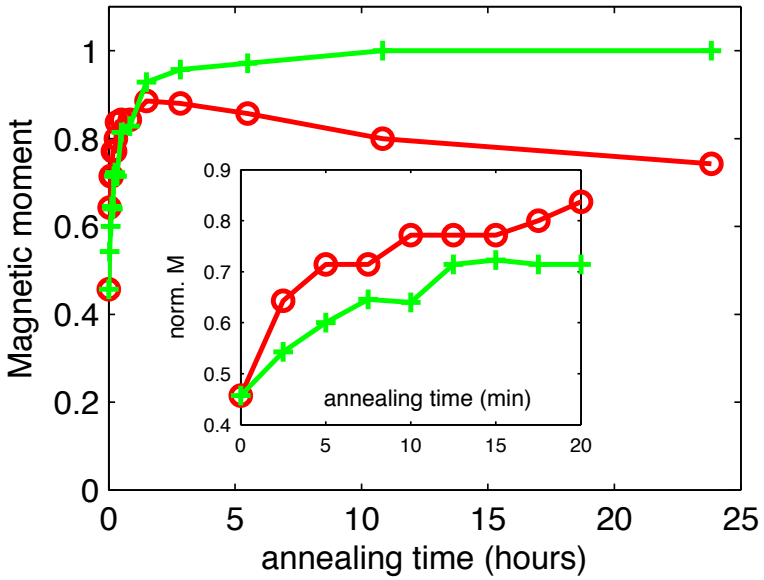

Figure 6.4: The evolution of magnetic moment of a GaMnAs layer with nominal Mn doping $x = 7\%$ and thickness 50 nm subjected to standard annealing (green dependence) compared to the evolution of sample subjected to etch-anneal procedure (red dependence). The etching was performed before each annealing step.

higher (by ~ 3 K). There are two possible explanations for the observed enhancement of the maximum T_c when using the etch-anneal procedure compared to the standard annealing: 1) faster annealing progress enables us to avoid slow detrimental processes (e.g. Mn clustering), 2) repeated oxide etching results in removal of possibly inferior part of the GaMnAs layer (if a vertical gradient of magnetic properties is present).

Figure 6.4 shows the evolution of magnetic moments. The inset of the figure shows a faster increase of the magnetic moment for the etch-annealed sample compared to the sample annealed in the standard way. For longer times, the magnetic moment is increasing with annealing time for the standard annealing. In the case of the etch-annealing procedure the fast increase is followed by the decrease of magnetization observed in further stages of etch-annealing procedure.

The decrease is consequence of the oxide layer removal. Assuming homogeneous magnetic properties of the GaMnAs layer in vertical direction we can estimate the thickness of the removed layer in each etch-annealing step to 0.8 nm (25% of 50 nm layer was removed in 15 steps).

The annealing process can also be monitored by the conductivity measurement. Fig. 6.5 shows the dependences of layer conductivity measured by four point method during the annealing of two pieces of a GaMnAs layer with nominal Mn concentration 8% and thickness 50 nm. One sample was annealed in standard

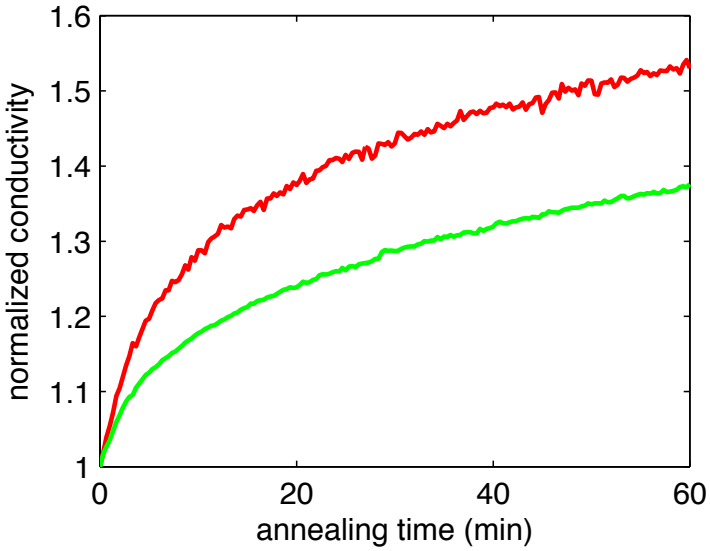

Figure 6.5: Evolution of conductivity of GaMnAs layer during annealing measured on the sample annealed without etching (green curve) and on the sample etched before the annealing started (red curve). The conductivity was measured by four-point method during the annealing on the hot plate at temperature 200°C.

conditions, the second sample was etched before the annealing started. Again the enhancement of annealing efficiency due to the etching can be clearly seen.

6.4 XPS study of etch-annealed samples

To further analyze the processes occurring during the annealing we performed angular resolved XPS measurements on samples in different stages of the etch-annealing procedure. We used 4 samples cut from a wafer of nominal thickness 50 nm and Mn concentration $x = 8\%$. The 4 samples were processed as follows:

- 1) left as-grown
- 2) etched
- 3) etched + annealed for 5 minutes at 200°C,
- 4) etched + annealed for 20 minutes at 200°C.

The etching of samples consisted of 30 s etching in HCl and water rinsing (the same procedure as in the case of the magnetic and transport study described above).

We recorded Mn $2p_{3/2}$, Ga 3d, As 3d and O 1s photoelectron spectra at emission angles of 0, 15, 30, 45, and 60°measured from the sample plane normal. We

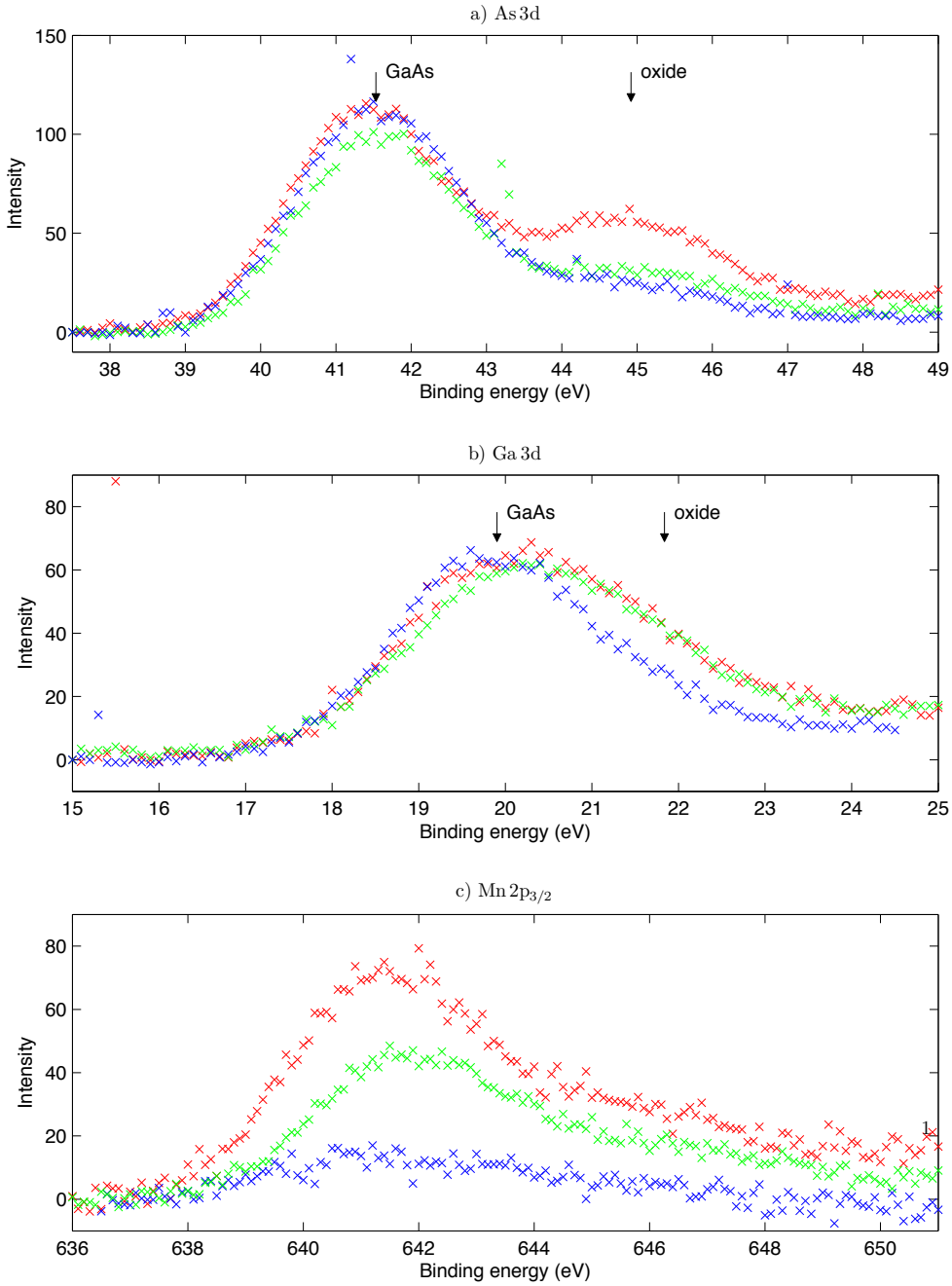

Figure 6.6: As 3d a), Ga 3d b), and Mn $2p_{3/2}$ c) spectra of the as-grown (red), etched (blue), and etched + 20 min annealed (green) samples measured in the normal emission direction.

used the AlKα excitation source producing x-ray radiation of the energy 1487 eV. Mn $2p_{3/2}$, Ga 3d and As 3d XPS spectra of samples 1,2, and 4 measured in the normal emission direction (with subtracted constant background) are shown in Fig. 6.6.

In the case of As 3d spectra the oxide peak is nicely separated from the peak of GaMnAs thanks to different oxidation number of the As atoms in GaMnAs and in the oxide. We can see that the oxide peak intensity is reduced by the etching, and then again increases with the annealing.

In the case of the Ga 3d spectra the separation between oxide and GaMnAs peak is smaller - approximately 2 eV. Nevertheless, we can see again that the oxide component is reduced by the etching and recovers by the annealing.

Looking at the Mn $2p_{3/2}$ spectra we can see that the as-grown sample has very strong Mn $2p_{3/2}$ signal. This signal corresponds to the Mn atoms which accumulated on the top of the layer during the growth performed in the vicinity of the roughening temperature. The Mn $2p_{3/2}$ intensity is reduced by the etching. With following annealing its intensity increases again which is clear sign of Mn out-diffusion from the layer.

The Mn atoms can be incorporated in many different positions (in the substitutional and in the interstitial positions in GaMnAs and in surface oxides and sub-oxides). The spectral decomposition of the Mn $2p_{3/2}$ peak is not straightforward [70, 71].

With the given quality of the data the decomposition of Mn $2p_{3/2}$ spectra would be rather uncertain, in the following analysis we focus on the overall photoelectron intensities recorded at varying emission angles. The angular resolved ratios will be used for the determination of the depth profiles of atomic species in the near surface region. The photoelectron mean free paths in GaAs are in the range of 1-3 nm (for Ga 3d, Mn $2p_{3/2}$ and O 1s photoelectrons) which is optimal for the analysis of depth profiles in the nanometer scale.

Fig. 6.7 shows ratios of Mn $2p_{3/2}$ / Ga 3d photoelectron intensities. The symbols are the experimental data, the lines in the figure represent simulated ratios which will be described later.

The highest Mn 2p / Ga 3d ratio was obtained for the as-grown sample. As discussed earlier this is a result of the accumulation of Mn in the surface during the growth at the temperature close to the roughening boundary.

In the case of the etched sample, the angular dependence is a constant function, not indicating Mn surface accumulation. This observation indicates that the Mn rich surface layer produced during the growth of the sample was fully removed by HCl etching procedure. We determined Mn concentration of 8.8% from this ratio, which is consistent with the nominal doping of the layer.

The increase of ratios measured on the etched + annealed samples agree with the expected surface Mn accumulation due to the annealing. Surprisingly, however, the angular dependences of the ratio do not exhibit the increase with the increasing emission angle, which is the behavior expected for the Mn surface accumulation.

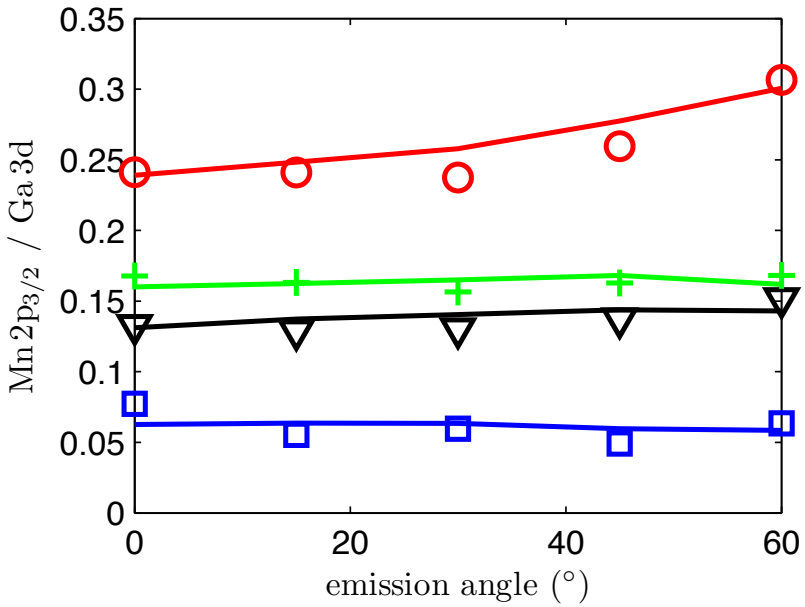

Figure 6.7: Symbols show the experimental Mn $2p_{3/2}$ / Ga 3d ratios of the as-grown (red), etched (blue), etched + annealed for 5 min (black), and etched + annealed for 20 min (green) samples. Lines show the simulated angular dependences.

Before we proceed to the detailed analysis of the above results, let us complete the experimental picture by a short look at the O 1s / Ga 3d angular resolved ratios shown in Fig. 6.8. In general the detail analysis of the O 1s data is hindered by presence of contamination coming from air (the samples were handled and annealed in air). Nevertheless, some information can be seen in those ratios.

The highest oxygen content was measured in the case of the as-grown sample. After etching the oxygen content drops down to a value consistent with the expected thickness of GaAs native oxide ($\sim$ 1 monolayer). With low temperature annealing some increase of oxygen is observed. The angular dependences in all cases show the increase with increasing emission angle which is consistent with the expected oxide location in the surface layer.

6.4.1 Model simulations

To quantitatively analyze the experimental ratios we employed SESSA software [72]. This software simulates XPS intensities of layered structures. It takes into account both the inelastic and elastic scattering of photoelectrons, which extends the applicability of the quantitative analysis to large emission angles.

As mentioned above, the increase of the Mn $2p_{3/2}$ / Ga 3d ratio due to the annealing indicates Mn surface accumulation but at the same time the angular dependence of the ratio exhibits unexpected constant behavior.

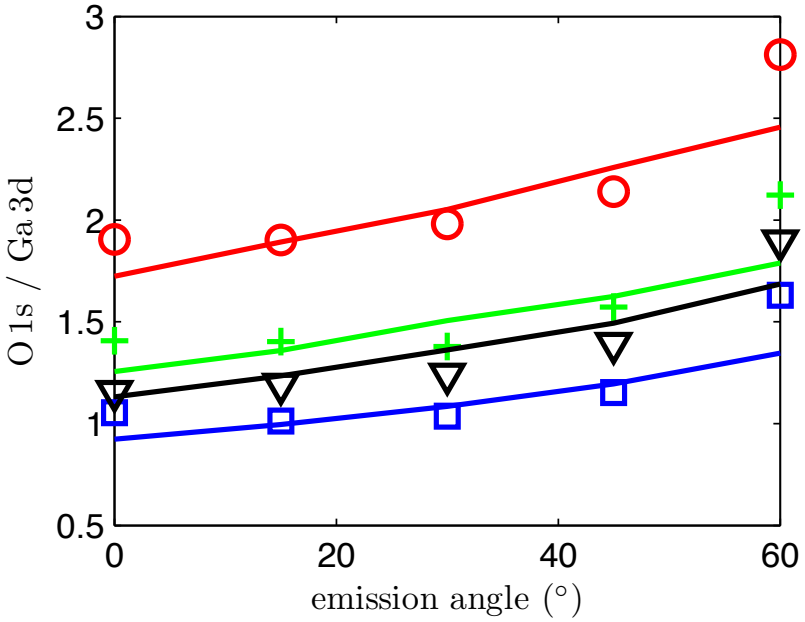

Figure 6.8: Symbols show the experimental O 1s / Ga 3d ratios of the as-grown (red), etched (blue), etched + annealed for 5 min (black), and etched + annealed for 20 min (green) samples. Lines show the simulated angular dependences.

Fig. 6.9 compares the angular dependences simulated for the following three model structures:

- A) Mn oxide over GaMnAs oxide - on the top of the layer
- B) Mn enriched GaMnAs oxide
- C) Mn oxide below GaMnAs oxide - in the interface between GaMnAs oxide and GaMnAs

The simulations are compared to the experimental angular dependence measured on the sample 4 (etched + 20 minutes annealed). The amount of Mn in all the three models was chosen to fit the Mn $2p_{3/2}$ / Ga 3d ratio at small emission angles.

It is clear that models A and B contradict the experimental results. On the other hand model C reproduces the constant behavior of the angular dependence of Mn $2p_{3/2}$ / Ga 3d ratio. The thickness of the oxidized GaMnAs layer used for this simulation is the value obtained from the O 1s / Ga 3d ratios of the etched sample.

The Mn oxide location below the native GaMnAs oxide solves the puzzle of the increase of Mn intensity without the expected behavior of the angular dependence. In this configuration, the increase of the Mn $2p_{3/2}$ photoelectron intensity due to

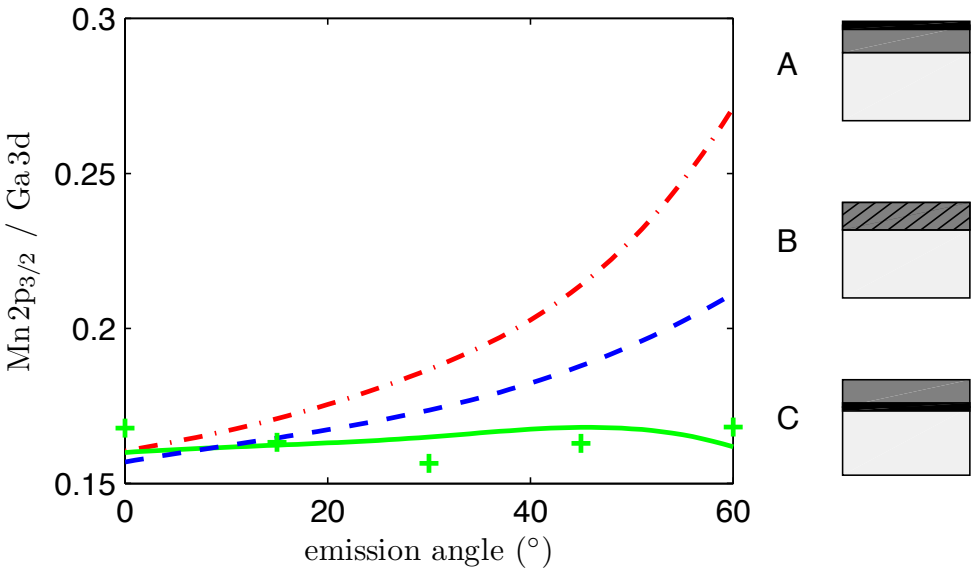

Figure 6.9: Comparison of model simulations used for the interpretation of angular resolved XPS intensity ratios. A - model with Mn oxide on the surface (red curve), B - model of Mn accumulation throughout the whole oxide layer (blue curve), C - model with Mn oxide formation below the native GaMnAs oxide layer (green curve). Crosses show the experimental Mn $2p_{3/2}$ / Ga 3d ratios of sample 4 (etched + annealed for 20 min).

the accumulation of Mn in the near surface region is balanced out by the contribution of Ga 3d photoelectrons coming from the surface GaMnAs native oxide. They are not attenuated with increasing emission angle which results in the observed broad angular dependence of the ratio.

The lines in Fig. 6.7 and Fig. 6.8 show simulated intensity ratios fitted for the particular sample. The as-grown etched sample was simulated as composed of bulk GaMnAs and surface oxide layer with the same Mn concentration. For the as-grown sample the model of a thick, Mn rich oxide layer was used, and for the two annealed samples the model of Mn oxide layer formed at the interface between the bulk GaMnAs and the oxidized GaMnAs layer was used.

The model parameters used in the simulation are listed in Tab. 6.2. It is worth stressing that both Mn $2p_{3/2}$ / Ga 3d and O 1s/ Ga 3d ratios were simulated with the same model parameters which is a strong argument in favor of the chosen models.

Two assumptions were made in the simulations: 1) the stoichiometry of oxides was fixed to 4 oxygen atoms per Ga and As pair and two oxygen atoms per Mn, 2) the inelastic mean free path were fixed to the values valid for GaAs. These assumptions may have resulted in some quantitative error in the layer thicknesses

Sample	Model	Model parameters
1) as-grown	B	9 Å oxidized $Ga_{0.6}Mn_{0.4}As$ / bulk
2) etched	homog.	5.3 Å oxidized bulk / bulk
3) etched + 5 min ann.	C	5.3 Å oxidized bulk / 2 Å MnO_2 / bulk
4) etched + 20 min ann.	C	5.3 Å oxidized bulk / 3 Å MnO_2 / bulk

Table 6.2: Table of model parameters used for simulation of angular dependences. Bulk denotes the $Ga_{0.912}Mn_{0.088}As$ material, the Mn concentration x=0.088 was found from the fit of

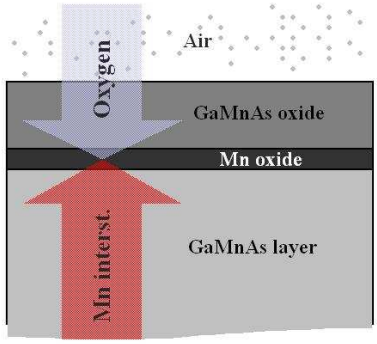

Figure 6.10: Processes occurring during the low temperature annealing of GaMnAs: Mn interstitial diffusion in GaMnAs, oxygen diffusion through the oxide layer, Mn oxide formation in the interface between oxide and bulk GaMnAs.

determination. Nevertheless, the main characteristics of the studied models are not affected by these assumptions.

6.5 Annealing processes

The enhancement of the annealing rate due to the surface oxide etching evidences the critical role of the surface conditions on the efficiency of the annealing. It is clear from the order of magnitude enhancement of the annealing rate that the Mn interstitial diffusivity is not the only parameter limiting the speed of the annealing process. In the case of thin layers ($t \sim$ 50nm or less) the dominant factor is the presence of the surface oxide and its thickness.

The angular resolved XPS experiment shows that the Mn oxide, which forms during the low temperature annealing, is located below the native GaMnAs oxide layer. The process of Mn oxide formation is illustrated in Fig. 6.10. This result suggests that the Mn diffusivity is very low in the oxide layer and that the rate of the annealing process is determined by the oxygen supply through the oxide layer.

Chapter 7

Conclusions

This thesis presented the study of ferromagnetic GaMnAs layers. The main focus was aimed on the optimization of the preparation conditions of the layers, i.e. understanding and control of the low temperature MBE growth and post-growth treatment. The magnetic and transport properties of the layers were studied to characterize the quality of the layers and the material trends.

We succeeded in the growth of high quality GaMnAs layers with nominal Mn doping up to 13%. At the time of publication of [51] we reported the world highest T_c observed in homogeneous GaMnAs alloy[1].

For the quality of the layers the precise control of growth temperature is necessary. We have used band gap thermometry to monitor substrate temperature. We observed temperature increase as large as 50°C during the growth of GaMnAs layers which is not observed by standard temperature measurement (i.e. by thermocouple mounted on sample manipulator). We explained this behavior on the basis of the radiation heat transfer model between the substrate heater and the sample with varying spectral characteristic. These observations are very important for reproducibility of the growth conditions and for transfer of the growth conditions to other MBE systems. We published these results in [62].

The characterization of magnetic properties of the GaMnAs layers produced in our laboratory was presented. The series of samples with nominal Mn doping between 2 and 12.5% was studied. The Curie temperature increases with the doping in the whole region, however, at high nominal doping the increase slows due to the formation of compensating defects occurring during the growth at very low temperature. The results suggest that the Curie temperature is limited by the formation of the defects and could in principle be further increased when increasing the concentration of Mn substitutional atoms. The magnetic anisotropy of the layers was also investigated. The numerical approach for the simulation of hysteresis loops was developed. The simulations were used for the determination

[1]Since other group achieved further increase of Curie temperature by optimization of the annealing temperature [15]. We reproduced their approach with our layers and reached the same Curie temperature [16].

of the anisotropy constants.

We also characterized the electrical transport properties of the GaMnAs layers. The material trends were investigated on the series of samples with varying nominal Mn doping, again showing the material tendency to self-compensation which reduces the doping efficiency in high doping levels. We investigated the behavior of resistivity in the vicinity of Curie temperature in detail. We found that the high quality GaMnAs layers exhibit a cusp-like singularity in the temperature derivative of the resistivity. We pointed out that this behavior can be explained on the basis of theory of resistivity developed originally to explain the transport anomaly in ferromagnetic metals. We published these results in [16].

The annealing process was studied using combination of the magnetometry, transport, and angular resolved XPS measurements. We pointed out the critical role of the oxide layer during the annealing and showed that the rate of Mn interstitial out-diffusion during annealing can be dramatically increased by the repeated surface oxide removal by HCl etching (published in [51]).

The high quality GaMnAs layers produced in our laboratory were also used in studies performed by our collaborators who performed various experiments: x-ray holography [73, 74], x-ray standing wave [75], light-induced magnetization precession experiments [76, 77, 78] , studies of anisotropic magneto-resistance [79, 80], and construction of devices for the electrical control of ferromagnetism in GaMnAs [52].

Bibliography

[1] H. Ohno. Making nonmagnetic semiconductors magnetic. *Science*, 281:951, 1998.

[2] Steven C. Erwin and A. G. Petukhov. Self-compensation in manganese-doped ferromagnetic semiconductors. *Phys. Rev. Lett.*, 89:227201, 2002.

[3] K. M. Yu, W. Walukiewicz, T. Wojtowicz, I. Kuryliszyn, X. Liu, Y. Sasaki, and J. K. Furdyna. Effect of the location of mn sites in ferromagnetic $Ga_{1-x}Mn_xAs$ on its curie temperature. *Phys. Rev.*, B 65:201303, 2002.

[4] J. Mašek, I. Turek, J. Kudrnovský, F. Máca, and V. Drchal. Compositional Dependence of Formation Energies of Substitutional and Interstitial Mn in Partially Compensated (Ga,Mn)As. *Acta Phys. Pol.*, A 105:637, 2004.

[5] T. Jungwirth, K. Y. Wang, J. Mašek, K. W. Edmonds, Jürgen König, Jairo Sinova, M. Polini, N. A. Goncharuk, A. H. MacDonald, M. Sawicki, R. P. Campion, L. X. Zhao, C. T. Foxon, and B. L. Gallagher. Prospects for high temperature ferromagnetism in (Ga,Mn)As semiconductors. *Phys. Rev.*, B 72:165204, 2005.

[6] J. Blinowski and P. Kacman. Spin interactions of interstitial Mn ions in ferromagnetic GaMnAs. *Phys. Rev.*, B 67:121204, 2003.

[7] C. T. Foxon, R. P. Campion, K. W. Edmonds, L. Zhao, K. Wang, N. R. S. Farley, C. R. Staddon, and B. L. Gallagher. The growth of high quality GaMnAs films by MBE. *J. Mater. Sci.*, 15:727, 2004.

[8] H. Munekata, H. Ohno, S. von Molnár, Armin Segmüller, L. L. Chang, and L. Esaki. Diluted magnetic III-V semiconductors. *Phys. Rev. Lett.*, 63:1849, 1989.

[9] J. Mašek and F. Máca. Lattice Expansion of (Ga,Mn)As: The Role of Substitutional Mn and of the Compensating Defect. *Acta Phys. Pol.*, A 108:789, 2005.

[10] T. Jungwirth, J. Mašek, K. Y. Wang, K. W. Edmonds, M. Sawicki, M. Polini, Jairo Sinova, A. H. MacDonald, R. P. Campion, L. X. Zhao, N. R. S. Farley, T. K. Johal, G. van der Laan, C. T. Foxon, and B. L. Gallagher. Low-temperature magnetization of (Ga,Mn)As semiconductors. *Phys. Rev.*, B 73:165205, 2005.

[11] H. Ohno, H. Munekata, T. Penney, S. von Molnár, and L. L. Chang. Magnetotransport properties of p-type (In,Mn)As diluted magnetic III-V semiconductors. *Phys. Rev. Lett.*, 68:2664, 1992.

[12] H. Ohno, A. Shen, F. Matsukura, A. Oiwa, A. Endo, S. Katsumoto, and Y. Iye. (Ga,Mn)As: A new diluted magnetic semiconductor based on GaAs. *Appl. Phys. Lett.*, 69:363, 1996.

Bibliography

[13] R. P. Campion, K. W. Edmonds, L. X. Zhao, K. Y. Wang, C. T. Foxon, B. L. Gallagher, and C. R. Staddon. High quality gamnas films grown with as dimers. *J. Cryst. Growth*, 247:42, 2003.

[14] K. Y. Wang, R. P. Campion, K. W. Edmonds, M. Sawicki, T. Dietl, C. T. Foxon, and B. L. Gallagher. Magnetism in (Ga,Mn)As Thin Films With T_C Up To 173K. *AIP Conference Proceedings*, 772:333, 2005.

[15] M. Wang, R. P. Campion, A. W. Rushforth, K. W. Edmonds, C. T. Foxon, and B. L. Gallagher. Achieving High Curie Temperature in (Ga,Mn)As. *Appl. Phys. Lett.*, 93:132103, 2008.

[16] V. Novák, K. Olejník, J. Wunderlich, M. Cukr, K. Výborný, A. W. Rushforth, K. W. Edmonds, R. P. Campion, B. L. Gallagher, Jairo Sinova, and T. Jungwirth. Curie point singularity in the temperature derivative of resistivity in (Ga,Mn)As. *Phys. Rev. Lett.*, 101:077201, 2008.

[17] R. P. Campion, K. W. Edmonds, L. X. Zhao, K. Y. Wang, C. T. Foxon, B. L. Gallagher, and C. R. Staddon. High-quality GaMnAs films grown with arsenic dimers. *J. Cryst. Growth*, 247:42–48, 2003.

[18] V. Avrutin, D. Humienik, S. Frank, A. Koeder, W. Schoch, W. Limmer, R. Sauer, and A. Waag. Growth of GaMnAs under near-stoichiometric conditions. *J. Appl. Phys.*, 98(2):023909, 2005.

[19] T. Wojtowicz T., J.K. Furdyna, X. Liu, K.M. Yu, and W. Walukiewicz. Electronic effects determining the formation of ferromagnetic $III_{1-x}Mn_xV$. *Physica E*, 25:171–180, 2004.

[20] O.D. Dubon, M.A. Scarpulla, R. Farshchi, and K.M. Yu. Doping and defect control of ferromagnetic semiconductors formed by ion implantation and pulsed-laser melting, 2006. Proceedings of the 23rd International Conference on Defects in Semiconductors.

[21] M. A. Scarpulla, R. Farshchi, P. R. Stone, R. V. Chopdekar, K. M. Yu, Y. Suzuki, and O. D. Dubon. Electrical transport and ferromagnetism in $Ga_{1-x}Mn_xAs$ synthesized by ion implantation and pulsed-laser melting. *J. Appl. Phys.*, 103:073913, 2008.

[22] R. Farshchi, M. A. Scarpulla, P. R. Stone, K. M. Yu, I. D. Sharp, J. W. Beeman, H. H. Silvestri, L. A. Reichertz, E. E. Haller, and O. D. Dubon. Compositional tuning of ferromagnetism in $Ga_{1-x}Mn_xP$. *Solid State Commun.*, 140:443, 2006.

[23] T. Hayashi, Y. Hashimoto, S. Katsumoto, and Y. Iye. Effect of low-temperature annealing on transport and magnetism of diluted magnetic semiconductor (Ga, Mn)As. *Appl. Phys. Lett.*, 78:1691, 2001.

[24] K. W. Edmonds, P. Boguslawski, K. Y. Wang, R. P. Campion, N. R. S. Farley, B. L. Gallagher, C. T. Foxon, M. Sawicki, T. Dietl, M. B. Nardelli, and J. Bernholc. Mn interstitial diffusion in (Ga,Mn)As. *Phys. Rev. Lett.*, 92:037201, 2004.

[25] H. Raebiger, M. Ganchenkova, and J. von Boehm. Diffusion and clustering of substitutional Mn in (Ga,Mn)As. *Appl. Phys. Lett.*, 89:012505, 2006.

[26] T. Hynninen, H. Raebiger, J. von Boehm, and A. Ayuela. High Curie temperatures in (Ga,Mn)N from Mn clustering. *Appl. Phys. Lett.*, 88:122501, 2006.

Bibliography

[27] A. Kwiatkowski, D. Wasik, M. Kamińska, R. Bożek, J. Szczytko, A. Twardowski, J. Borysiuk, J. Sadowski, and J. Gosk. Structure and magnetism of MnAs nanocrystals embedded in GaAs as a function of post-growth annealing temperature. *J. Appl. Phys.*, 101:113912, 2007.

[28] D. E. Bliss, W. Walukiewicz, J. W. Ager III, E. E. Haller, K. T. Chan, and S. Tanigawa. Annealing studies of low-temperature-grown GaAs:Be. *J. Appl. Phys.*, 71:1699, 1992.

[29] M. B. Stone, K. C. Ku, S. J. Potashnik, B. L. Sheu, N. Samarth, and P. Schiffer. Capping-induced suppression of annealing in $Ga_{1-x}Mn_xAs$ epilayers. *Appl. Phys. Lett.*, 83:4568, 2003.

[30] M. Adell, J. Adell, L. Ilver, J. Kanski, J. Sadowski, and J. Z. Domagala. Mn enriched surface of annealed (GaMn)As layers annealed under arsenic capping. *Phys. Rev. B*, 75(5):054415, 2007.

[31] M. Malfait, J. Vanacken, W. Van Roy, G. Borghs, and V. V. Moshchalkov. Enhanced annealing effect in an oxygen atmosphere on $Ga_{1-x}Mn_xAs$. *Appl. Phys. Lett.*, 86:132501, 2005.

[32] J. Sadowski, J. Z. Domagala, V. Osinniy, J. Kanski, M. Adell, L. Ilver, C. Hernandez, F. Terki, S. Charar, and D. Maude. High ferromagnetic phase transition temperatures in GaMnAs layers annealed under arsenic capping. 2006.

[33] T. Dietl, H. Ohno, F. Matsukura, J. Cibert, and D. Ferrand. Zener model description of ferromagnetism in zinc-blende magnetic semiconductors. *Science*, 287:1019, 2000.

[34] T. Jungwirth, Jairo Sinova, J. Mašek, J. Kučera, and A. H. MacDonald. Theory of ferromagnetic (iii,mn)v semiconductors. *Rev. Mod. Phys.*, 78:809, 2006.

[35] T. Dietl. Ferromagnetic semiconductors. *Semicond. Sci. Technol.*, 17:377, 2002.

[36] T. Sasaki, S. Sonoda, Y. Yamamoto, K. Suga, S. Shimizu, K. Kindo, and H. Hori. Magnetic and transport characteristics on high Curie temperature ferromagnet of Mn-doped GaN. *J. Appl. Phys.*, 91:7911, 2002.

[37] A. M. Nazmul, T. Amemiya, Y. Shuto, S. Sugahara, and M. Tanaka. High Temperature Ferromagnetism in GaAs-based Heterostructures with Mn Delta Doping. *Phys. Rev. Lett.*, 95:017201, 2005.

[38] F. Maccherozzi, M. Sperl, G. Panaccione, J. Minár, S. Polesya, H. Ebert, U. Wurstbauer, M. Hochstrasser, G. Rossi, G. Woltersdorf, W. Wegscheider, and C. H. Back. Evidence for a Magnetic Proximity Effect up to Room Temperature at Fe/(Ga,Mn)As Interfaces. *Phys. Rev. Lett.*, 101:267201, 2008.

[39] T. Dietl, H. Ohno, and F. Matsukura. Hole-mediated ferromagnetism in tetrahedrally coordinated semiconductors. *Phys. Rev.*, B 63:195205, 2001.

[40] M. Abolfath, T. Jungwirth, J. Brum, and A. H. MacDonald. Theory of magnetic anisotropy in $III_{1-x}Mn_xV$ ferromagnets. *Phys. Rev.*, B 63:054418, 2001.

[41] M. Sawicki, F. Matsukura, A. Idziaszek, T. Dietl, G. M. Schott, C. Rüster, C. Gould, G. Karczewski, G. Schmidt, and L. W. Molenkamp. Temperature dependent magnetic anisotropy in (Ga,Mn)As layers. *Phys. Rev.*, B 70:245325, 2004.

[42] F. Matsukura, M. Sawicki, T. Dietl, D. Chiba, and H. Ohno. Magnetotransport properties of metallic (Ga,Mn)As films with compressive and tensile strain. *Physica*, E 21:1032, 2004.

[43] A. W. Rushforth, E. De Ranieri, J. Zemen, J. Wunderlich, K. W. Edmonds, C. S. King, E. Ahmad, R. P. Campion, C. T. Foxon, B. L. Gallagher, K. Výborný, J. Kučera, and T. Jungwirth. Voltage control of magnetocrystalline anisotropy in ferromagnetic - semiconductor/piezoelectric hybrid structures. *Phys. Rev.*, B 78:085314, 2008.

[44] M. Sawicki, K-Y. Wang, K. W. Edmonds, R. P. Campion, C. R. Staddon, N. R. S. Farley, C. T. Foxon, E. Papis, E. Kaminska, A. Piotrowska, T. Dietl, and B. L. Gallagher. In-plane uniaxial anisotropy rotations in (Ga,Mn)As thin films. *Phys. Rev.*, B 71:121302, 2005.

[45] K. Ohta, T. Kojima, and T. Nakagawa. Anisotropic surface migration of Ga atoms on GaAs(001). *J. Cryst. Growth*, 95(1-4):71–74, 1989.

[46] K. Y. Wang, M. Sawicki, K. W. Edmonds, R. P. Campion, A. W. Rushforth, A. A. Freeman, C. T. Foxon, B. L. Gallagher, and T. Dietl. Control of Coercivities in (Ga,Mn)As Thin Films by Small Concentrations of MnAs Nanoclusters. *Appl. Phys. Lett.*, 88:022510, 2006.

[47] S. A. Wolf, D. D. Awschalom, R. A. Buhrman, J. M. Daughton, S. von Molnár, M. L. Roukes, A. Y. Chtchelkanova, and D. M. Treger. Spintronics: A spin-based electronics vision for the future. *Science*, 294:1488, 2001.

[48] J. De Boeck, W. Van Roy, J. Das, V. Motsnyi, Z. Liu, L. Lagae, H. Boeve, K. Dessein, and G. Borghs. Technology and materials issues in semiconductor-based magnetoelectronics. *Semicond. Sci. Technol.*, 17:342, 2002.

[49] Igor Zutic, Jaroslav Fabian, and S. Das Sarma. Spintronics: Fundamentals and applications. *Rev. Mod. Phys.*, 76:323, 2004.

[50] H. Ohno, D. Chiba, F. Matsukura, T. Omiya, E. Abe, T. Dietl, Y. Ohno, and K. Ohtani. Electric-field control of ferromagnetism. *Nature*, 408:944, 2000.

[51] K. Olejník, M. H. S. Owen, V. Novák, J. Mašek, A. C. Irvine, J. Wunderlich, and T. Jungwirth. Enhanced annealing, high Curie temperature and low-voltage gating in (Ga,Mn)As: A surface oxide control study. *Phys. Rev.*, B 78:054403, 2008.

[52] M. H. S. Owen, J. Wunderlich, V. Novák, K. Olejník, J. Zemen, K. Výborný, S. Ogawa, A. C. Irvine, A. J. Ferguson, H. Sirringhaus, and T. Jungwirth. Low voltage control of ferromagnetism in a semiconductor p-n junction. *In Press, New J. Phys.*, 2009.

[53] Y. Ohno, D. K. Young, B. Beschoten, F. Matsukura, H. Ohno, and D. D. Awschalom. Electrical spin injection in a ferromagnetic semiconductor heterostructure. *Nature*, 402:790, 1999.

[54] M. A. Herman and H. Sitter. *Molecular beam epitaxy - fundamentals and current status*. Springer-Verlag Berlin-Heidelberg-New York-London-Paris-Tokyo, 1989.

[55] B.A. Joyce and C.T. Foxon. Kinetic studies of the growth of iii-v compounds using modulated molecular beam techniques. *J. Cryst. Growth*, 31:122 – 129, 1975.

[56] C. T. Foxon, J. A. Harvey, and B. A. Joyce. Evaporation of GaAs under equilibrium and nonequilibrium conditions using a modulated beam technique. *J. Phys. Chem. Solids*, 34(10):1693, 1973.

[57] A. Ichimiya and P. I. Cohen. *Reflection High Energy Electron Diffraction*. Cambridge University Press, United Kingdom, 2004.

[58] A. Ohtake. Surface reconstructions on GaAs(001). *Surf. Sci. Rep.*, 63:295–327, 2008.

[59] S. R. Johnson, C. Lavoie, T. Tiedje, and J. A. Mackenzie. Semiconductor substrate temperature measurement by diffuse reflectance spectroscopy in molecular beam epitaxy. *Journal Of Vac. Sci. Technol. B*, 11:1007, 1993.

[60] M. R. Brozel and G. E. Stillman. *Properties of Gallium Arsenide*. INSPEC, The Institution of Electrical Engineers, London, United Kingdom, 1996.

[61] J. S. Blakemore. Semiconducting and other major properties of gallium-arsenide. *J. Appl. Phys.*, 53(10):R123–R181, 1982.

[62] V. Novák, K. Olejník, M. Cukr, L. Smrčka, Z. Remeš, and J. Oswald. Substrate temperature changes during molecular beam epitaxy growth of GaMnAs. *J. Appl. Phys.*, 102:083536, 2007.

[63] D. T. J. Hurle. A comprehensive thermodynamic analysis of native point defect and dopant solubilities in gallium arsenide. *J. Appl. Phys.*, 85:6957, 1999.

[64] K. Y. Wang, M. Sawicki, K. W. Edmonds, R. P. Campion, S. Maat, C. T. Foxon, B. L. Gallagher, and T. Dietl. Reorientation transition in single-domain (Ga,Mn)As. *Phys. Rev. Lett.*, 95:217204, 2005.

[65] L. Thevenard, L. Largeau, O. Mauguin, A. Lemaître, K. Khazen, and H. J. von Bardeleben. Evolution of the magnetic anisotropy with carrier density in hydrogenated $Ga_{1-x}Mn_xAs$. *Phys. Rev.*, B 75:195218, 2007.

[66] X. Liu, Y. Sasaki, and J. K. Furdyna. Ferromagnetic resonance in $Ga_{1-x}Mn_xAs$: effects of magnetic anisotropy. *Phys. Rev.*, B 67:205204, 2003.

[67] T. Jungwirth, Jairo Sinova, A. H. MacDonald, B. L. Gallagher, V. Novák, K. W. Edmonds, A. W. Rushforth, R. P. Campion, C. T. Foxon, L. Eaves, K. Olejník, J. Mašek, S. R. Eric Yang, J. Wunderlich, C. Gould, L. W. Molenkamp, T. Dietl, and H. Ohno. Character of states near the fermi level in (Ga,Mn)As: impurity to valence band crossover. *Phys. Rev.*, B 76:125206, 2007.

[68] M. E. Fisher and J. S. Langer. Resistive anomalies at magnetic critical points. *Phys. Rev. Lett.*, 20:665, 1968.

[69] C. Haas. Magnetic semiconductors. *Crit. Rev. Solid State Sci.*, 1:47, 1970.

[70] S. A. Hatfield, T. D. Veal, C. F. McConville, G. R. Bell, K. W. Edmonds, R. P. Campion, C. T. Foxon, and B. L. Gallagher. Photoelectron spectroscopy study of $Ga_{1-x}Mn_xAs(001)$ surface oxide and low temperature cleaning. *Surf. Sci.*, 585(1-2):66–74, 2005.

[71] R. J. Iwanowski. Comment on "Photoelectron spectroscopy study of $Ga_{1-x}Mn_xAs(001)$ surface oxide and low temperature cleaning" by S.A. Hatfield et al. [Surf. Sci. 585 (2005) 66]. *Surf. Sci.*, 600(19):4670 – 4671, 2006.

Bibliography

[72] W. S. M. Werner, W. Smekal, and C. J. Powel. *NIST Standard Reference Database 100, Database for the Simulation of Electron Spectra for Surface Analysis (SESSA): Version 1.1*, 2005.

[73] M. Kopecký, J. Kub, E. Busetto, A. Lausi, M. Cukr, V. Novák, K. Olejník, J. P. Wright, and J. Fábry. Location of Mn sites in ferromagnetic $Ga_{1-x}Mn_xAs$ studied by means of x-ray diffuse scattering holography. *J. Appl. Cryst.*, 39:735, 2006.

[74] M. Kopecký, E. Busetto, A. Lausi, Z. Šourek, J. Kub, M. Cukr, V. Novák, K. Olejník, and P. Wright. Imaging of interstitial atoms in $Ga_{1-x}Mn_xAs$ layers by means of X-ray diffuse scattering. *J. Appl. Crystallogr.*, 41:544–547, 2008.

[75] V. Holý, Z. Matěj, O. Pacherová, V. Novák, M. Cukr, K. Olejník, and T. Jungwirth. Mn incorporation in as-grown and annealed (Ga,Mn)As layers studied by x-ray diffraction and standing-wave fluorescence. *Phys. Rev.*, B 74:245205, 2006.

[76] E. Rozkotová, P. Němec, P. Horodyská, D. Sprinzl, F. Trojánek, P. Malý, V. Novák, K. Olejník, M. Cukr, and T. Jungwirth. Light-induced magnetization precession in GaMnAs. *Appl. Phys. Lett.*, 92:122507, 2008.

[77] E. Rozkotová, P. Němec, N. Tesařová, P. Malý, V. Novák, K. Olejník, M. Cukr, and T. Jungwirth. Coherent control of magnetization precession in ferromagnetic semiconductor (Ga,Mn)As. *Appl. Phys. Lett.*, 93:232505, 2008.

[78] E. Rozkotová, P. Němec, D. Sprinzl, P. Horodyská, F. Trojánek, P. Malý, V. Novák, K. Olejník, M. Cukr, and T. Jungwirth. Laser-Induced Precession of Magnetization in GaMnAs. *IEEE Trans. Magn.*, 44:2674–2677, 2008.

[79] A. W. Rushforth, K. Výborný, C. S. King, K. W. Edmonds, R. P. Campion, C. T. Foxon, J. Wunderlich, A. C. Irvine, P. Vašek, V. Novák, K. Olejník, Jairo Sinova, T. Jungwirth, and B. L. Gallagher. Anisotropic magnetoresistance components in (Ga,Mn)As. *Phys. Rev. Lett.*, 99:147207, 2007.

[80] A. W. Rushforth, K. Výborný, C. S. King, K. W. Edmonds, R. P. Campion, C. T. Foxon, J. Wunderlich, A. C. Irvine, V. Novák, K. Olejník, A. A. Kovalev, Jairo Sinova, T. Jungwirth, and B. L. Gallagher. The Origin and Control of the Sources of AMR in (Ga,Mn)As Devices. *In Print, J. Mag. Magn. Mater.*

List of publications

[1] K Olejník, J Zemek, and J Stejskal. Surface coverage of polyaniline-coated silica gels. *Acta Phys. Slovaca*, 53(2):121–127, 2003.

[2] J. Zemek, P. Jiříček, and K. Olejník. Photoelectron escape from iron oxide. *Surf. Sci.*, 572(1):93–102, 2004.

[3] K. Olejník, J. Zemek, and W. S. M. Werner. Angular-resolved photoelectron spectroscopy of corrugated surfaces. *Surf. Sci.*, 595(1-3):212–222, 2005.

[4] M. Kopecký, J. Kub, E. Busetto, A. Lausi, M. Cukr, V. Novák, K. Olejník, J. P. Wright, and J. Fábry. Location of Mn sites in ferromagnetic $Ga_{1-x}Mn_xAs$ studied by means of x-ray diffuse scattering holography. *J. Appl. Cryst.*, 39:735, 2006.

[5] V. Holý, Z. Matěj, O. Pacherová, V. Novák, M. Cukr, K. Olejník, and T. Jungwirth. Mn incorporation in as-grown and annealed (Ga,Mn)As layers studied by x-ray diffraction and standing-wave fluorescence. *Phys. Rev.*, B 74:245205, 2006.

[6] A. Jablonski, K. Olejník, and J. Zemek. Elastic electron backscattering from flat and rough Si surfaces. *J. Electron Spectrosc. Relat. Phenom.*, 152(1-2):100–106, 2006.

[7] A. W. Rushforth, K. Výborný, C. S. King, K. W. Edmonds, R. P. Campion, C. T. Foxon, J. Wunderlich, A. C. Irvine, P. Vašek, V. Novák, K. Olejník, Jairo Sinova, T. Jungwirth, and B. L. Gallagher. Anisotropic magnetoresistance components in (Ga,Mn)As. *Phys. Rev. Lett.*, 99:147207, 2007.

[8] V. Novák, K. Olejník, M. Cukr, L. Smrčka, Z. Remeš, and J. Oswald. Substrate temperature changes during molecular beam epitaxy growth of GaMnAs. *J. Appl. Phys.*, 102:083536, 2007.

[9] J. Zemek, P. Jiříček, J. Houdková, K. Olejník, and A. Jablonski. Attenuation of photoelectrons and Auger electrons leaving nickel deposited on a gold surface. *Surf. Interface Anal.*, 39(12-13):916–921, 2007.

[10] T. Jungwirth, Jairo Sinova, A. H. MacDonald, B. L. Gallagher, V. Novák, K. W. Edmonds, A. W. Rushforth, R. P. Campion, C. T. Foxon, L. Eaves, K. Olejník, J. Mašek, S. R. Eric Yang, J. Wunderlich, C. Gould, L. W. Molenkamp, T. Dietl, and H. Ohno. Character of states near the fermi level in (Ga,Mn)As: impurity to valence band crossover. *Phys. Rev.*, B 76:125206, 2007.

[11] K. Olejník, M. H. S. Owen, V. Novák, J. Mašek, A. C. Irvine, J. Wunderlich, and T. Jungwirth. Enhanced annealing, high Curie temperature, and low-voltage gating in (Ga,Mn)As: A surface oxide control study. *Phys. Rev. B*, 78:054403, 2008.

[12] V. Novák, K. Olejník, J. Wunderlich, M. Cukr, K. Výborný, A. W. Rushforth, K. W. Edmonds, R. P. Campion, B. L. Gallagher, Jairo Sinova, and T. Jungwirth.

Curie point singularity in the temperature derivative of resistivity in (Ga,Mn)As. *Phys. Rev. Lett.*, 101:077201, 2008.

[13] B. G. Park, J. Wunderlich, D. A. Williams, S. J. Joo, K. Y. Jung, K. H. Shin, K. Olejník, A. B. Shick, and T. Jungwirth. Tunneling anisotropic magnetoresistance in Multilayer-(Co/Pt)/AlOx/Pt structures. *Phys. Rev. Lett.*, 100:087204, 2008.

[14] E. Rozkotová, P. Němec, P. Horodyská, D. Sprinzl, F. Trojánek, P. Malý, V. Novák, K. Olejník, M. Cukr, and T. Jungwirth. Light-induced magnetization precession in GaMnAs. *Appl. Phys. Lett.*, 92:122507, 2008.

[15] J. Zemek, K. Olejník, and P. Klapetek. Photoelectron spectroscopy from randomly corrugated surfaces. *Surf. Sci.*, 602:1440–1446, 2008.

[16] M. Kopecký, E. Busetto, A. Lausi, Z. Šourek, J. Kub, M. Cukr, V. Novák, K. Olejník, and P. Wright. Imaging of interstitial atoms in $Ga_{1-x}Mn_xAs$ layers by means of X-ray diffuse scattering. *J. Appl. Crystallogr.*, 41:544–547, 2008.

[17] K. Olejník and J. Zemek. Applicability of magic angle for angle-resolved X-ray photoelectron spectroscopy of corrugated SiO_2/Si surfaces: Monte Carlo calculations. *Surf. Sci.*, 602:2581–2586, 2008.

[18] E. Rozkotová, P. Němec, N. Tesařová, P. Malý, V. Novák, K. Olejník, M. Cukr, and T. Jungwirth. Coherent control of magnetization precession in ferromagnetic semiconductor (Ga,Mn)As. *Appl. Phys. Lett.*, 93:232505, 2008.

[19] Kh. Khazen, H. J. von Bardeleben, M. Cubukcu, J. L. Cantin, V. Novák, K. Olejník, M. Cukr, L. Thevenard, and A. Lemaître. Anisotropic magnetization relaxation in ferromagnetic $Ga_{1-x}Mn_xAs$ thin films. *Phys. Rev. B*, 78(19):195210, 2008.

[20] E. Rozkotová, P. Němec, D. Sprinzl, P. Horodyská, F. Trojánek, P. Malý, V. Novák, K. Olejník, M. Cukr, and T. Jungwirth. Laser-Induced Precession of Magnetization in GaMnAs. *IEEE Trans. Magn.*, 44:2674–2677, 2008.

[21] K. Olejník, V. Novák, M. Cukr, J. Mašek, and T. Jungwirth. Etching enhanced annealing of GaMnAs layers. *In Press, J. Crystal Growth.*

[22] V. Novák, K. Olejník, and M. Cukr. Free carrier induced substrate heating of the epitaxially grown GaMnAs. *In Press, J. Crystal Growth.*

[23] A. W. Rushforth, K. Výborný, C. S. King, K. W. Edmonds, R. P. Campion, C. T. Foxon, J. Wunderlich, A. C. Irvine, V. Novák, K. Olejník, A. A. Kovalev, Jairo Sinova, T. Jungwirth, and B. L. Gallagher. The Origin and Control of the Sources of AMR in (Ga,Mn)As Devices. *In Print, J. Mag. Magn. Mater.*

[24] M. H. S. Owen, J. Wunderlich, V. Novák, K. Olejník, J. Zemen, K. Výborný, S. Ogawa, A. C. Irvine, A. J. Ferguson, H. Sirringhaus, and T. Jungwirth. Low voltage control of ferromagnetism in a semiconductor p-n junction. *In Press, New J. Phys.*